APPLICATIONS OF NEUTRON RADIOGRAPHY & TOMOGRAPHY

Martin Nicholas Dawson

Submitted in accordance with the requirements for the degree of
doctor of philosophy

The University of Leeds
School of Physics & Astronomy
May 2008

The candidate confirms that the work submitted is his own and that appropriate credit has been given where reference has been made to the work of others.

This research was funded by the Earth and Biosphere Institute, University of Leeds (one third) and the Institut Laue-Langevin, Grenoble (two thirds).

All images included herein are the direct result of the personal work and research of the author.

Acknowledgements

I would like to express my gratitude towards my supervisor and colleague, **Professor Bob Cywinski**, a source of guidance, support and ideas, whose imagination, ingenuity and boundless enthusiasm have been a great inspiration throughout my studies.

I would also like to thank the numerous people, who took the time and trouble to assist me in their various fields of expertise, providing me with samples, equipment, information, and advice. Their help has been greatly appreciated.

Jane Francis, Phil Guise, Crispin Little, Joseph Holden, Nigel Bubb, Rosemary Stephens, Jim Best, Suleiman Al-Hinai, Carlos Grattoni, Quentin Fisher, John Forth, Adrian Brough, Bob Finch, Stephen Compton, Eric Dickinson and Liane Benning (University of Leeds); **Nico Gray and Anthony Thornton** (University of Manchester); **Andrea Snelling** (University of Leicester); **Dominic Powlesland** (Landscape Research Centre); **Susan Kilcoyne** (University of Salford); **Erica Hendy** (University of Bristol); **Jeff Liston** (Hunterian Museum and Art Gallery); **Ross Springell, Rajmund Mokso and Marco Di Michiel** (European Synchrotron Radiation Facility); **Roland Gähler, Andreas Van Overberghe, Marcus Trapp, Mark Faist, Hendrik Ballhausen, Ken Andersen, David Jullien, Pascal Mouveau and Pierre Thomas** (Institut Laue-Langevin); **and Elbio Calzada, Klaus Lorenz and Michael Schulz** (Forschungs-neutronenquelle Heinz Maier-Leibnitz).

Finally, but by no means least, I would like to thank my parents, **Graham and Marilyn,**

for their continual support and encouragement (read nagging me to get a "proper" job), and **Kymmene** for enduring my huffier moments and for knowing that a good cup of tea can cure all ills. Tak.

Abstract

This thesis represents the investigation and development of neutron imaging techniques as a versatile method that can be used to reveal the presence, position, size, morphology, and chemical composition of structures and materials within a sample. The underlying physics of neutron radiography and tomography mean that it has fundamental similarities to x-ray techniques, although some subtle differences mean that neutrons are often applicable in circumstances where x-rays are not. This complementarity is presented and discussed.

Most of the experimental results contained herein were obtained using *Neutrograph*, the thermal neutron imaging instrument at the Institut Laue-Langevin's high flux research nuclear reactor in Grenoble, France. *Neutrograph* utilises the world's most intense neutron beam currently in use for this purpose, $\sim 3\times10^{9}\ n\cdot cm^{-2}\cdot s^{-1}$ across an area of $220\times220\ mm^{2}$, and is capable of producing high quality images with single-frame exposure times down to the millisecond regime. Meanwhile, the modest beam divergence of $6\ mrad$ (equivalent to a beam length-to-diameter ratio, L/D, of ~ 150) can achieve a spatial resolution in the region of $150\text{-}300\ \mu m$.

It is demonstrated how these properties make *Neutrograph* ideal for obtaining time-resolved measurements of dynamic processes in both two and three dimensions, and for imaging relatively thick samples or highly attenuating materials on a reasonable time-scale. One aspect that is addressed in this research is the potential scope of relevance of neutron imaging methods across a range of scientific disciplines. In this

vein, attempts have been made not only to draw examples from a number of different fields (palaeontology, archaeology, and fluid mechanics, for example), but also to improve the performance of the instrumentation and methodology, and to establish novel techniques that will further the applicability of neutron imaging. An illustration of the latter is the use of a polarised neutron beam to investigate the presence and distribution of magnetic components in non-magnetic matrices.

Table of Contents

List of figures

List of tables

It is always with the best intentions that the worst work is done.

~ Oscar Wilde

1 Introduction

Transmission radiography measures intensity variations of radiation passing through a sample in order to visualise internal structures. It has been exploited extensively as a non-destructive testing tool in a range of practical applications since shortly after Röntgen's discovery of x-rays in 1895, while experimenting with cathode-ray tubes. Following their discovery by Chadwick in 1932, neutrons too began to be implemented in similar research activities pioneered by Kallmann and Kuhn [1], and Peter [2] in the late 1930s and 1940s, initially using sources based on radioisotopes (typically radium-beryllium) and later on accelerators. However, this early work was greatly limited by the low flux beams available ($\sim 3\times 10^9$ $n\cdot cm^{-2}\cdot s^{-1}$), and thus concentrated on understanding the underlying principles and evaluating potential uses [3-5]. It was not until the advent of reactor sources (*British Experimental Pile 0* at the Atomic Energy Authority Research Establishment in Harwell, England, for example) in the late 1940s that experimental techniques were refined and optimised, and applications were explored more usefully, notably by Thewlis and Derbyshire [6, 7]. The impetus for developing neutron radiography was the need for a technique that could be employed in applications that precluded the use of x-rays – highlighting the complementarity of neutrons and x-rays – the most valuable of which (at least at the time) was the investigation of reactor fuel assemblies (x-rays were unsuitable as they were unable to penetrate the heavy metal components and gamma-radioactivity produced fogging on the detector).

Although steady advances in instrumentation and refinements in experimental practices have lead to improved performance and an ever-broadening spectrum of applications, radiography has one major shortcoming: all the data for a three-dimensional sample are compressed into a two-dimensional image, often making it difficult to distinguish between regions with similar properties. This issue was overcome in 1972, when Hounsfield demonstrated "computed axial tomography" [8, 9]. Tomography is based on a mathematical framework formulated by Radon in 1917 [10], and provides a system for reconstructing the three-dimensional properties of a sample from a set of many radiographs taken at a series of angles – clearly a very appealing analytic tool.

Undoubtedly, the major advances in transmission imaging have been based around x-rays, while, although having gained from the general scientific and technological substructure, neutrons have lagged behind. The main reasons for this are, firstly, x-ray imaging developments have been driven by their prominent role in diagnostic medicine (which has also lead to them becoming far better-known and hence more widespread); and, secondly, high quality x-ray results can be obtained with relatively simple and portable instrumentation, whereas equivalent results with neutrons require large experimental facilities, which are much less accessible. Consequently, neutrons are utilised more sparingly, and often only as a last resort after other methods have failed to yield the desired information.

In recent years, several new neutron imaging facilities have become operational (*Neutrograph* at the Institut Laue-Langevin, *CONRAD* at the Hahn-Meitner Institut [11], *ANTARES* at the Forschungsneutronenquelle Heinz Maier-Leibnitz [12], and *NEUTRA* at the Paul Scherrer Institut [13], to name a few) as have several commercial neutron imaging services, offering the opportunity to develop and expand the scope of neutron imaging, and making suitable instruments more available to the greater scientific community. Hopefully, this will help to alleviate the difficulties mentioned above. Indeed, in the past five years alone neutron imaging has been successfully applied in fields as diverse as archaeology [14-16], palaeontology [17], engineering and materials science [18-22], and more [23-28].

The work presented here is based mostly on direct experimental experience on *Neutrograph,* and, as such, much of the discussion of the processes involved are explicitly specific to this instrument. However, many of the principles are generic to neutron imaging, and indeed to transmission imaging as a whole. The aims of this research were to characterise *Neutrograph* in order to understand its experimental capabilities and limitations, and then to develop new techniques and to explore new applications to make effective use of these properties.

2 Principles of Imaging

Transmission imaging is a technique that uses incident penetrating radiative energy to investigate the internal structures and material compositions of optically opaque objects non-destructively. The types of radiation used are multitudinous, ranging from particles (neutrons, electrons) to electromagnetic waves (x-rays, γ-rays), with specific selection depending upon the requirements of the application. However, the underlying principle is universal: as the radiation passes through the object of study, it is attenuated (its intensity is reduced) by an amount that depends both on the thickness of the sample along the path taken by the radiation, and on the materials present along that path.

2.1 Principles of radiography

Radiography involves the bi-dimensional detection of the transmitted beam intensity in a plane perpendicular to beam propagation (Figure 2.1 and 2.2). This produces a two-dimensional grey-scale image, or shadowgraph, which may be considered as a measure of the spatially varying integrated attenuation properties of the object, and holds information about sample thickness (including the presence of cracks and voids) and the chemical composition. If accurate details of either the morphology or chemistry of a sample are known, then in principle quantitative data about the other can be extracted.

The transmission, T, is simply the ratio of the transmitted beam intensity, I, to the incident beam intensity, I_0

$$T = \frac{I}{I_0} \qquad \text{Equation 2.1}$$

For any narrow path, the transmission behaviour of the radiation can be described by the basic law of radiation attenuation in matter

$$I = I_0\, \mathrm{e}^{-\int \alpha\, ds} \qquad \text{Equation 2.2}$$

where α is the local linear attenuation coefficient, and s is the propagation path. The attenuation coefficient is a material property and is given by

$$\alpha = \sigma \frac{\rho\, N_A}{M} \quad \text{or} \quad \alpha = \sum_i \sigma_i \frac{\rho_i N_A}{M_i} \qquad \text{Equation 2.3}$$

for single-element or multi-element materials respectively, where σ is the total interaction cross-section, ρ is the material density, N_A is Avogadro's number, and M is the molar mass of the material.

The interaction cross-section for radiation passing through matter can generally be divided into two macroscopic components, both of which depend on the radiation energy: absorption and scattering (coherent and incoherent). Absorption is the retention of incident radiation without further transmission, reflection or scattering, coupled with the emission of a secondary photon (which can be neglected). In scattering events, localized non-uniformities cause the dispersal of radiation into a range of directions. Absorption is an ideal attenuation process, while, although scattering also attenuates, it introduces uncertainty since it alters the propagation direction of the radiation. Consequently, there is a possibility for scattered radiation to be redirected onto the detector at any arbitrary position resulting in unavoidable background noise and the blurring of features and boundaries, which degrade the image quality and resolution. In many cases, these effects are small and can be assumed to be negligible.

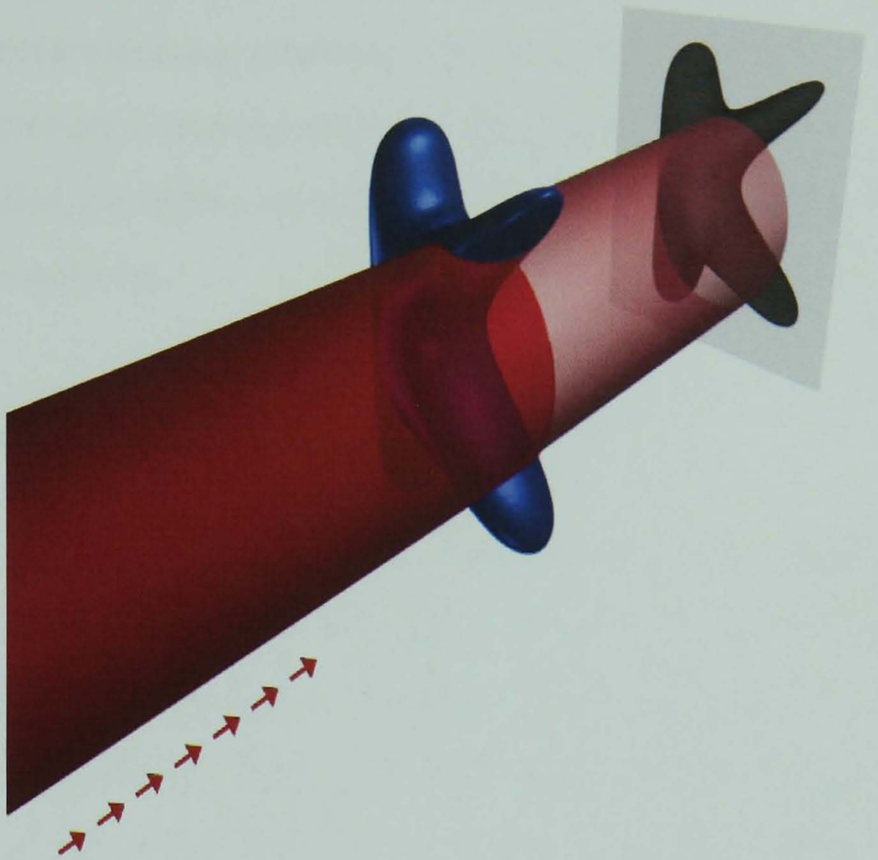

Figure 2.1: *A schematic representation of radiography. The arrows indicate the beam propagation direction.*

Figure 2.2: *A neutron radiograph of a wild flower. The image is a negative; darker areas indicate higher attenuation.*

Although the attenuation law holds in simple cases, it should be noted that it breaks down in situations involving relatively thick samples or samples comprised of strongly absorbing or strongly scattering materials. Here, because the interaction cross-section is energy dependent, multiple scattering effects and changes in the radiation energy need to be taken into account.

2.2 Principles of tomography

Despite providing a useful insight into internal structures, radiography has nonetheless compressed a three-dimensional object into two dimensions, resulting in loss of information. Computerised tomography (CT) is a technique that makes the retrieval of three-dimensionality possible (Figure 2.3). Radiographic images, or projections, are taken from different directions in small, successive steps all the way around (2π) the sample (Figure 2.4). This series of images can then be used to computationally reconstruct a virtual three-dimensional object. Many algorithms exist for tomographic reconstruction, and these are explained in depth elsewhere [29-31] (see Appendix A for a summary). One of the fastest, most efficient, and most widely-used techniques is filtered back-projection, and this is the one used on *Neutrograph.*

All projections are first rearranged into a new set of images such that the *n*th pixel row of each projection is now stored sequentially in an individual image, a so-called sinogram (Figure 2.5). Every sinogram contains all the attenuation information for all angles for a finite section of the sample as defined by a single row of pixels. An implementation of the inverse two-dimensional Radon transform is then used to independently calculate a cross-sectional slice from each sinogram. Each reconstructed slice lies in a plane perpendicular to the axis of rotation around the sample, and is, by definition, exactly one pixel thick (Figure 2.6). Collecting all slices into an image stack represents the three-dimensional attenuation properties of the object; each pixel in every slice is actually a finite volume, a so-called voxel, whose value represents the attenuation properties of the corresponding volume in the sample. This image stack can be rendered and manipulated with software to highlight specific volumes,

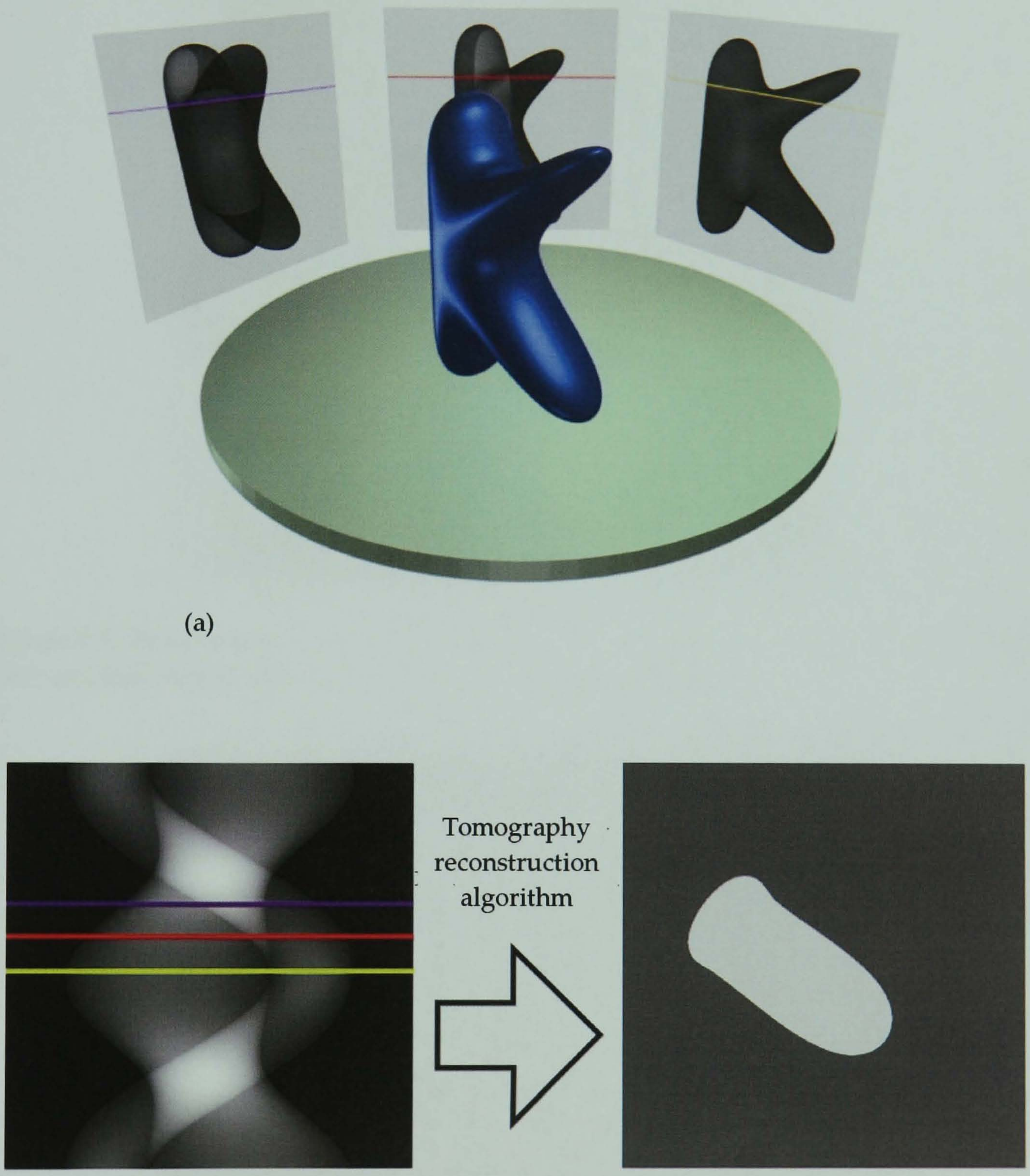

(a)

(b)

(c)

Figure 2.3: *Schematic diagram showing how (a) multiple projections are (b) reformatted into sinograms and then (c) reconstructed into cross-sectional slices. Sinogram produced using CTSim* [32].

surfaces, planes or contours, or to view the selected feature(s) from any perspective (Figure 2.7). The software used on *Neutrograph* is VGStudio Max (Volume Graphics).

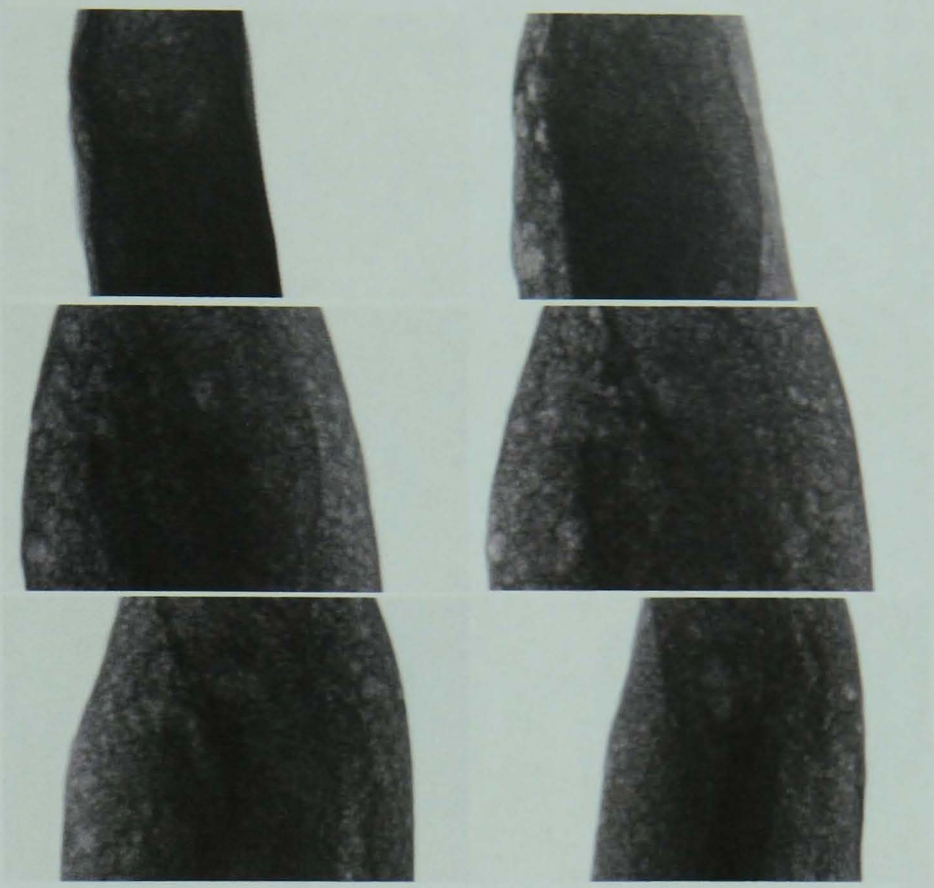

Figure 2.4: *Projections of a piece of bread rotated around a vertical axis by 0°, 30°, 60°, 90°, 120°, and 150° (left to right, top to bottom). The images are negatives.*

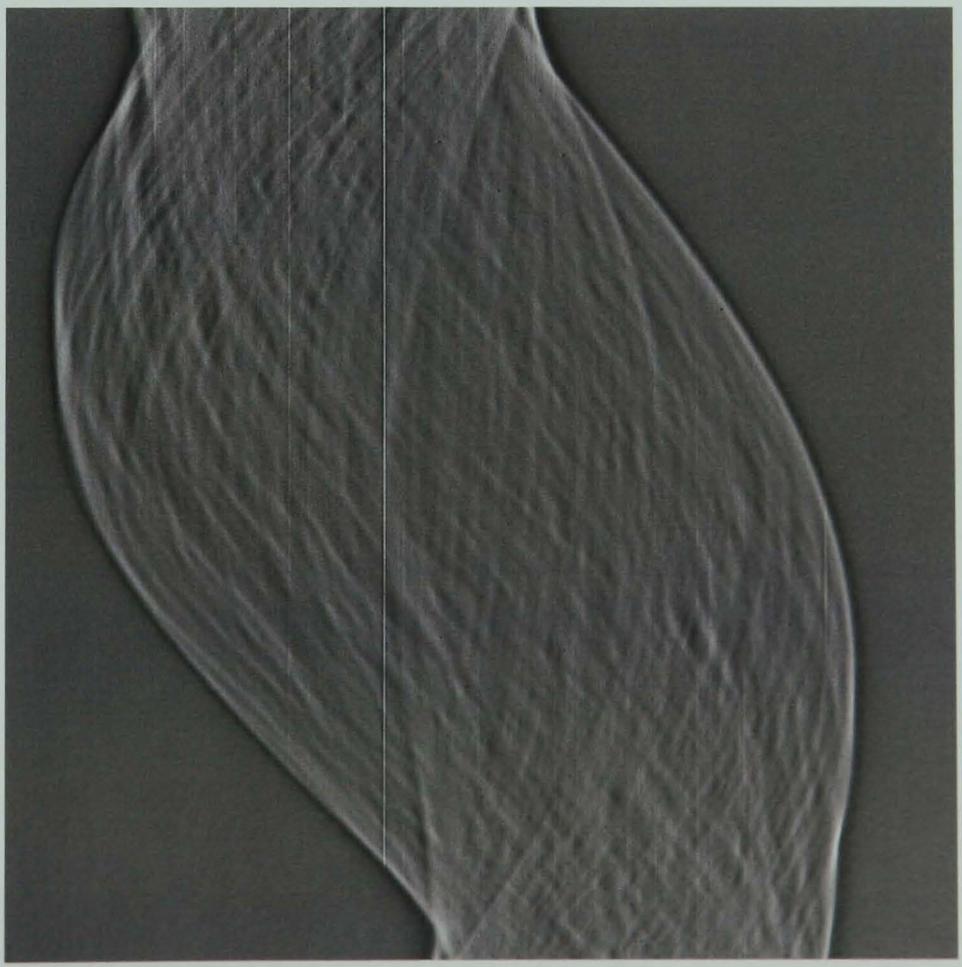

Figure 2.5: *A single sinogram produced from 801 projections of the piece of bread in* Figure 2.4. *The vertical white stripes show the presence of over-active pixels.*

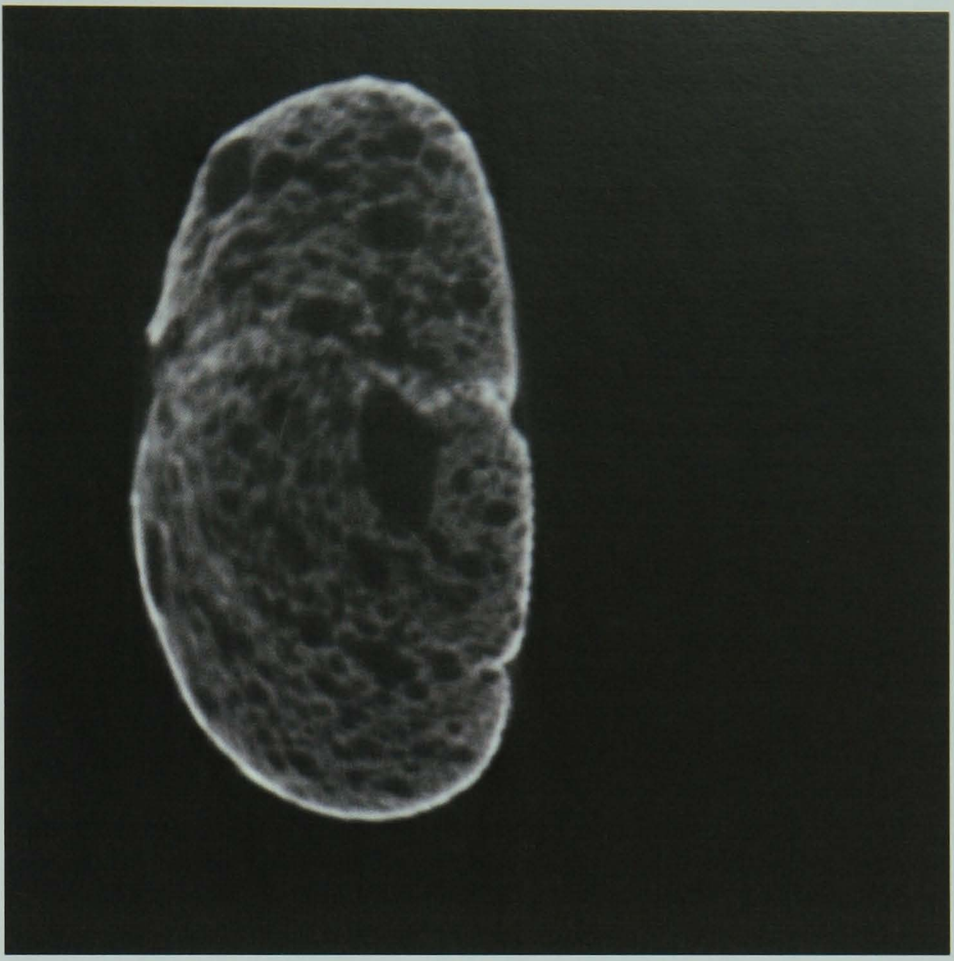

Figure 2.6: *The reconstructed slice from the sinogram in* Figure 2.5 *reveals the internal aerated structure of the bread.*

Figure 2.7: *The image stack of the piece of bread in* Figure 2.4 *rendered in 3-D. A section has been cut away to reveal the internal structure.*

2.3 Comparison of neutrons and x-rays

Neutron and x-ray imaging techniques are analogous, but in terms of the diversity of techniques, the range of applications, the technology currently developed, and global distribution, x-rays are by far the more advanced tool. This is exemplified by the constant evolution of new generations of cutting-edge, all-in-one x-ray CT scanners, which operate increasingly faster, more efficiently, and more accurately, and which range in size from the desktop to the industrial. Moreover, many of the innovative "neutron imaging techniques" have been copied or developed directly from their x-ray counterparts [33, 34, for example]. However, it would be a misconception to treat the analytical information provided by one as being predominantly superior to or more suitable than that yielded by the other. Both x-rays and neutrons have their own strengths and weaknesses, and the two techniques should be viewed as being entirely complementary.

X-rays interact almost exclusively with the electronic distribution of matter via electromagnetic effects: the photoelectric effect, Compton scattering (corresponding roughly to absorption and scattering with neutrons, respectively), and electron-positron pair production. These interactions correlate strongly with Z, the atomic number of the atoms present (Figure 2.8) [35]. This means that x-rays are relatively insensitive to light elements such as hydrogen, while heavier elements such as lead prove difficult to penetrate – even high energy x-rays (*100-300 keV*) can only penetrate several millimetres of lead. It also follows that neighbouring elements in the periodic table prove difficult to differentiate, since they differ only by $Z = \pm 1$. Furthermore, at higher energies Compton scattering is dominant and so, not only are large dense objects difficult to image, but resolving capability is greatly reduced.

Conversely, since the neutron has zero net charge, it interacts with atomic nuclei via the strong force. Atomic nuclei are *~10^5* times smaller than outer electron orbits and, as a result, neutrons pass through matter much more easily than x -rays can. Unlike x-rays, it is not possible to form a general trend for neutron interaction cross-sections, which vary irregularly across the periodic table (Figure 2.8) [36, 37]. Typically, neutron scattering effects may be considered to be constant (although scattering cross-sections tend to drop sharply for energies below the Bragg cut-off), whereas absorption is dependent on neutron velocity, and thus energy. For this reason, cold and thermal neutrons are usually better suited for neutron imaging. The total cross-section can be approximated by

$$\sigma_{total} = \sigma_{scattering} + \frac{v_{thermal}}{v}\sigma_{absorption,thermal} \qquad \text{Equation 2.4}$$

where $\sigma_{scattering}$ is the sum of coherent and incoherent scattering effects, v is the neutron velocity, and $v_{thermal}$ and $\sigma_{absorption,thermal}$ are the velocity (~2200 ms^{-1}) and absorption cross-section for thermal neutrons, respectively. See Table 2.2 for a summary of x-ray and neutron classifications.

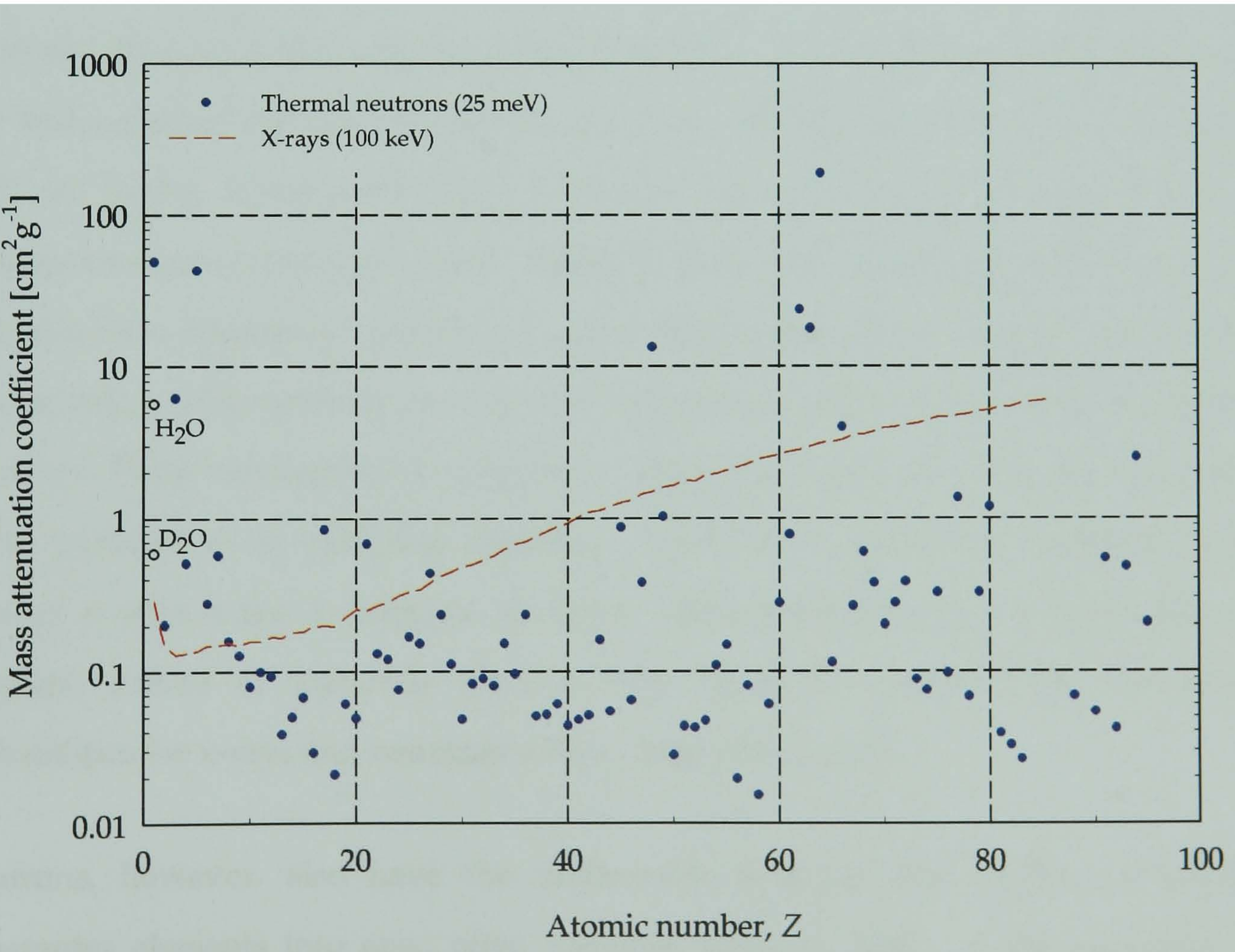

Figure 2.8: *Element mass attenuation coefficients for thermal neutrons (25 meV) and for x-rays (100 keV).*

		Energy *[eV]*	Temperature *[K]*	Wavelength *[Å]*	Speed *[ms^{-1}]*
Neutrons	Ultracold	10^{-7}	0.001	750	5
	Cold	0.005	60	4	1000
	Thermal	0.025	300	1.8	2200
	Epithermal	0.5	6000	0.4	10^4
	Fast	10^6	10^{10}	10^{-4}	10^7
X-rays	Soft	10^3	10^7	10	3×10^8
	Hard	10^4	10^8	1	3×10^8
	High energy	10^5	10^9	0.1	3×10^8

Table 2.1: *Characteristic properties of neutron and x-ray radiation.*

Neutrons, then, hold several striking benefits over x-rays. Hydrogen (and subsequently any hydrogenous material) is opaque, yet many metals (including aluminium and lead) are highly transparent. Many elements with similar atomic numbers can be distinguished, as can many isotopes. Although neutrons are highly penetrative, several elements have absorption resonances, where the absorption cross-section increases by several orders of magnitude for a narrow range of energies, lying within the thermal spectrum. These elements (including boron and gadolinium) are thus ideal for use as tracer particles or in radiation shielding. One further significant property of the neutron is that it has a magnetic moment, offering the prospect of visualising the magnetic nature of materials (Section 5.3). Table 2.2 compares the interaction probabilities for x-rays and neutrons with a range of elements.

Neutrons, however, also have the undesirable property that neutron absorption transmutes elements into new, often unstable, isotopes. Many of these isotopes are either very short-lived or have very low levels of activity, but even traces of others can leave a sample radioactive for many years (e.g. ${}^{59}_{27}\mathrm{Co} + \mathrm{n} \rightarrow {}^{60}_{27}\mathrm{Co}$, ${}^{60}\mathrm{Co}$ decays by negative beta decay with a half-life of 5.27 years, ${}^{60}_{27}\mathrm{Co} \rightarrow {}^{60}_{28}\mathrm{Ni} + e^{-} + \bar{\nu}_{e} + 2.5\ MeV$).

Element	Thermal Neutrons (*25 meV*)		X-rays (*100 keV*)	
	σ_{total} *[barn]*	TVT *[cm]*	σ_{total} *[barn]*	TVT *[cm]*
^{1}H	82.36	0.5 *	0.29	12.5 *
^{2}H	7.64	3.6 *	0.29	12.5 *
B	772.14	0.04	2.49	13
C	5.55	6	3.00	11
Al	1.73	33	7.64	8
Fe	14.18	2	34.48	0.8
Cd	2526	0.02	284.50	0.2
Gd	49880	0.001	812.05	0.1
Pb	11.29	7.5	1910	0.05

Table 2.2: *Total interaction cross-sections for x-rays and neutrons with a range of elements in their natural abundances. The TVT (tenth value thickness) is the approximate distance required to reduce the beam transmission to 10%.*

* *Values calculated for H_2O and D_2O. All other values calculated for elemental solids.*

3 Instrumentation

The configuration and parameters of imaging systems can vary greatly depending upon the type of radiation used and the experimental demands of their primary function (size and composition of objects studied, high spatial resolution, high temporal resolution, short exposure time, etc.). The majority of the experimental work discussed in later chapters was carried out on the neutron radiography and tomography research station, *Neutrograph,* at the Institut Laue-Langevin, and the structure, operation and performance of this instrument are therefore of foremost interest. Nonetheless, it is important to mark distinctions between *Neutrograph* and other facilities and techniques, and comparisons are thus drawn wherever appropriate.

3.1 Neutron source

The source of the neutrons harnessed by *Neutrograph* is the high flux nuclear reactor at the Institut Laue-Langevin [36], currently the world's most intense source of neutrons. Free neutrons are produced by nuclear fission at an average rate of *2.5* neutrons per event inside a *9.5 kg* fuel rod consisting of enriched (*93%*) uranium-235. Uranium-235 fissions spontaneously at a very slow rate, but this is accelerated upon bombardment with neutrons.

$$^{235}\mathrm{U} + \mathrm{n}_{\mathrm{thermal}} \rightarrow \text{fission fragments} + 2.5\ \mathrm{n}_{\mathrm{fast}} + 180\ MeV$$

Due to the interaction cross-section for uranium-235 being much higher for thermal neutrons than for fast neutrons, the emitted neutrons are moderated (slowed down) through multiple collisions with a *2.5 m* diameter tank of heavy water (deuterium oxide, D_2O) at *300 K*, which surrounds the fuel rod. A self-sustaining chain reaction is thence established (the reactor is periodically shut down for maintenance and fuel replenishment), with one fission neutron required to trigger further fission and one available for use after leaving the reactor core (the average *0.5* neutron remaining is absorbed by the material of the reactor).

The maximum practical rate of fission is limited by the rate at which the large amounts of energy released can be removed from the core. The operational thermal power is thus restricted to *58.3 MW* by a central, boron-loaded, neutron-absorbing control rod, while the core is maintained at *50°C* by circulating the heavy water moderator through heat exchangers. Beyond the moderator tank lies a much larger water (H_2O) tank encased in a thick, high density wall of borated concrete and steel, which provides radiation shielding for experimenters and instruments inside the reactor hall.

The reactor is designed such that the peak flux of thermal neutrons, $\sim 10^{15}\ n \cdot cm^{-2} \cdot s^{-1}$, occurs approximately *15 cm* from the outside edge of the core, and beamlines are positioned with their nose in this region in order to extract the maximum possible number of neutrons to the instrument at the opposite end. Most beam tubes are aligned tangentially to the core rather than pointing at the centre. This ensures that neutrons entering the beamline have undergone sufficient moderation to become thermalised – faster neutrons coming directly from the core are directed radially – and also reduces the intensity of the gamma-radiation background. Instruments requiring the highest neutron fluxes ($\sim 10^{9}\ n \cdot cm^{-2} \cdot s^{-1}$), including *Neutrograph*, are concentrated inside the reactor hall, while lower flux instruments ($\sim 10^{6}\ n \cdot cm^{-2} \cdot s^{-1}$) are located further away in two experimental guide halls.

3.2 The *Neutrograph* beamline

Neutrograph is situated on *Level C* of the reactor hall at the end of the *11 m* long H9 beamline (Figure 3.1), a location originally intended as a beam stop for *Lohengrin,* the fission product mass spectrometer that shares H9. This beam stop has now been replaced by a borated-aluminium sheet with a *200×200 mm*^{2} aperture. Behind this lies a *100 cm* long, high-density concrete primary beam shutter, which is mechanically hauled up an incline to allow neutrons to enter *Neutrograph*'s experimental enclosure or casemate (a safety feature: gravity ensures that the shutter closes in case of any system failure). Lohengrin has three key components positioned in and around the beam: an assembly for manoeuvring fissile isotope targets up to the nose of the beamline, a diaphragm shutter for limiting the beam, and a dipole magnet for deflecting and separating fission products. Although the latter is of little consequence, the former two can alter the beam's profile and intensity considerably, and must be kept constant during any measurements on *Neutrograph.*

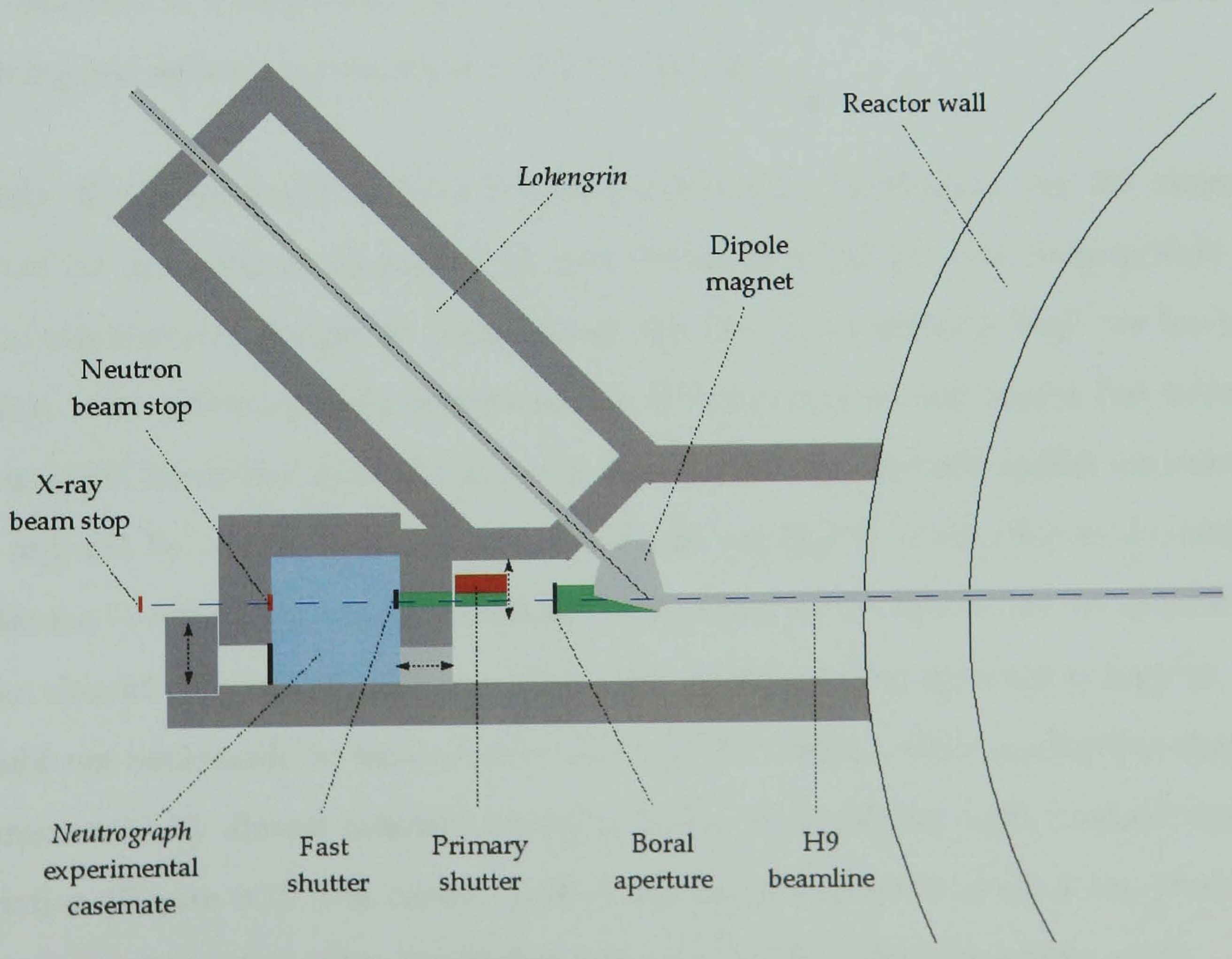

Figure 3.1: *Layout of the H9 beamline, which is shared by Neutrograph and Lohengrin.*

Radiation beams applied for imaging purposes can usually be completely characterised in terms of four properties: the flux distribution, the geometry, the divergence, and the energy spectrum. These properties may be fine-tuned by introducing various pieces of equipment along the flight path. For example, x-rays are commonly filtered through metal discs (often copper or aluminium) to remove lower energy contributions and thereby harden the beam. *Neutrograph*, however, currently utilises a simple helium-4-filled flight tube featuring no such refinement.

3.2.1 Flux

Being positioned so close to the reactor core means that *Neutrograph* benefits from an unparalleled neutron flux of $\sim 3\times 10^9\ n\cdot cm^{-2}\cdot s^{-1}$ at the sample imaging position (subject to random fluctuations caused by small variations (<2%) in the reactor power). The spatial limits of the beam are governed entirely by the dimensions of the flight tube, and the beam has an accordingly broad cross-section of approximately $220\times 220\ mm^2$. Such a wide potential field of view is beneficial for imaging as it allows large objects to be visualised in a single exposure (although even larger objects may be visualised by aligning and splicing exposures at multiple positions).

Ideally, the beam ought to have a homogeneous flux distribution (i.e. the intensity should be the same at all points) as vast fluctuations can lead to overexposure (or underexposure) of images in areas where the flux is particularly high (or low). In reality, some inhomogeneity is unavoidable in large cross-section beams, but, because some applications (for example, imaging objects with considerable spatial variation in the amount by which they attenuate the beam) are highly susceptible to deviations, while many others are not, it is difficult to stipulate acceptable levels. In general the beam should be homogeneous to within *~35%*, although discrepancies as high as *70%* would not necessarily be unworkable. *Neutrograph*'s beam profile is letterbox-shaped, characterised by almost constant intensity across its width but with marked vertical variation (Figure 3.2). The central part of the beam ($\sim 220\times 110\ mm^2$) is the preferred imaging position since it has the highest intensity and is uniform to within *~25%*.

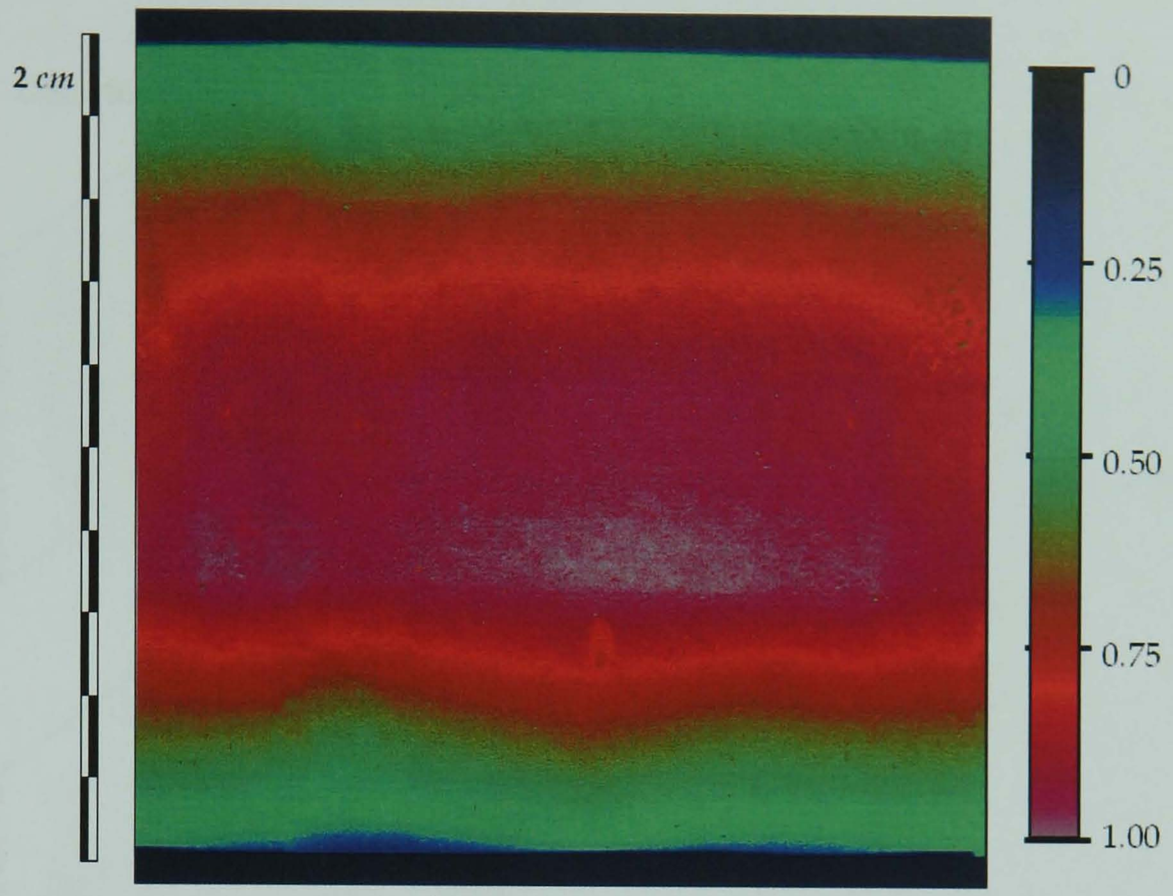

Figure 3.2: *Neutrograph's beam intensity profile. The limits are defined by the camera field of view (horizontal) and by the edge of the scintillator (vertical).*

3.2.2 Geometry

The geometry of the beam describes the spatial distribution of the radiation leaving the source. Various aspects, including the type of radiation, the type of source, and the application, affect the geometry used in any situation, but the three most commonly employed are the cone beam, the fan beam, and the parallel beam (Figure 3.3). Cone beams and fan beams are produced naturally as radiation emanates isotropically (equally in all directions) from a point source. Parallel beams, meanwhile, can only be approximated by taking a relatively small portion of a cone beam far from the source: at large distances, all rays are almost parallel.

Cone beams and fan beams have the benefit that images are magnified, allowing otherwise unresolvable features to be identified, but this can also lead to distortions. Furthermore, fan beams are only one-dimensional and must be scanned perpendicular to the plane of the fan in order to gain the second dimension necessary for radiography. This rules out the two-dimensional dynamic imaging of processes that

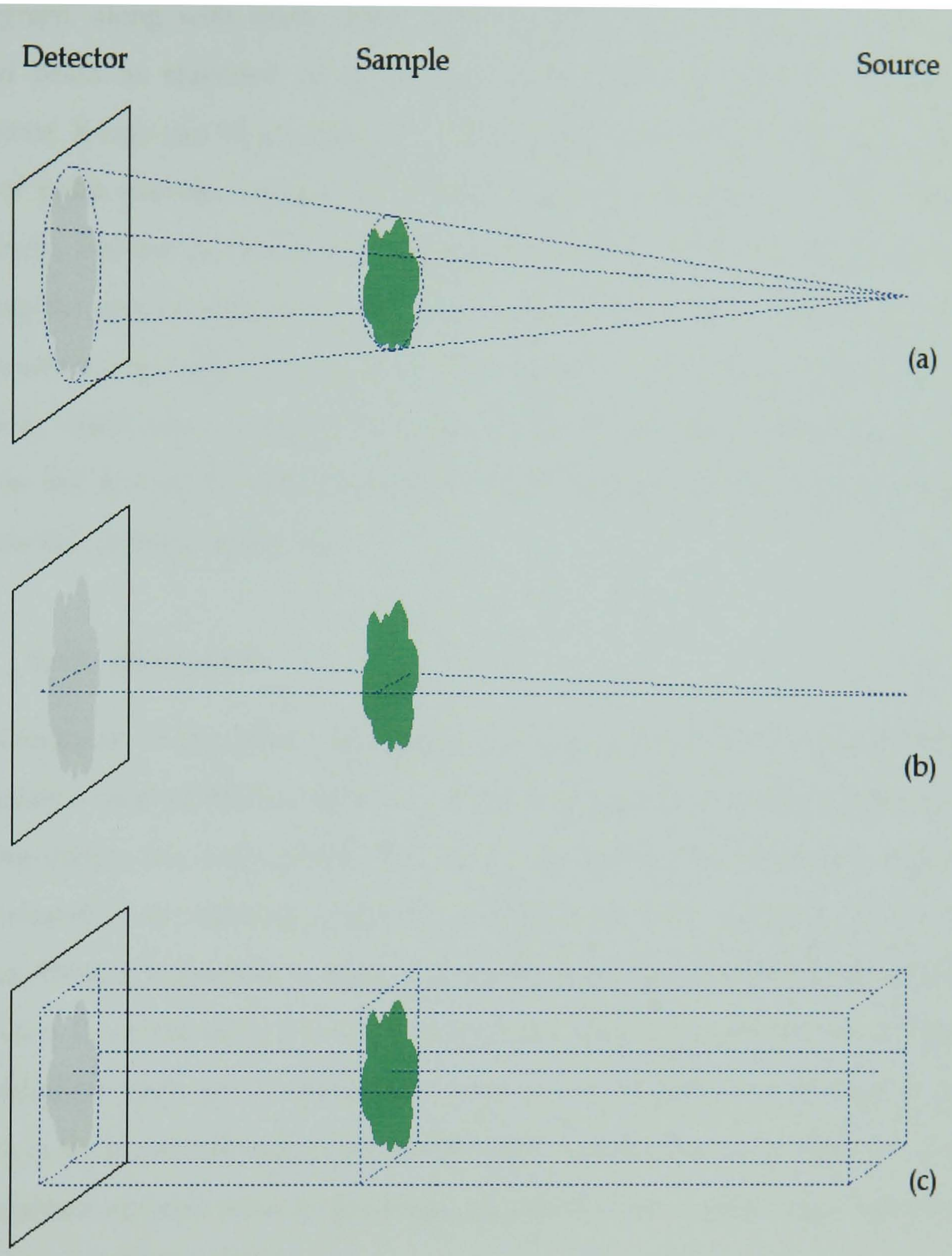

Figure 3.3: *The three most common imaging beam geometries: (a) a cone beam, (b) a fan beam, and (c) a parallel beam.*

occur faster than the time taken for a single scan. The advantage of a parallel beam is that tomographic imaging only requires rotation about the sample of π, since any projection, P_θ, will be an exact mirror image of the projection $P_{\theta+\pi}$ (see also Section 5.1). Fan (and cone) beams require a rotation of at least $\pi+p$, where p is the angle of the fan (or cone). In theory parallel beams need fewer projections and a shorter total exposure.

Neutrograph, along with every other world-leading neutron imaging facility, uses a parallel beam as standard. This, however, is as much a practical necessity as a preference. X-rays can be generated at a point source, or even at a carefully contrived array of point sources, making the beam geometry a question of design. Neutrons, conversely, emerge randomly from multiple, randomly positioned point sources and dictating the precise geometry of the beam is significantly more difficult. One simple way of converting a divergent parallel beam into a cone beam is by passing it through a pinhole, which acts as a quasi point source. The best attainable resolution is roughly equal to the size of the pinhole, but the steep decrease in flux makes this option unfavourable in many instances.

3.2.3 Divergence

The divergence of the beam determines the extent to which it spreads out as it propagates – its parallelism – and has a direct bearing on the spatial resolution in the resulting image: the more parallel the beam, the greater the resolution. This can be demonstrated by considering a perfectly parallel beam from a point source to a point detector. Here, it is possible to trace a ray for its entire path and the acquired image is very sharp. If, on the other hand, the beam is not absolutely parallel, rays originating from different parts of the beam can cross paths leading to a penumbra around features in the generated image: the overall effect is that of blurring (Figure 3.4). This is an altogether separate issue to the beam geometry; even a wide angle fan beam can have a very small divergence.

For imaging instruments the most useful figure of merit of the divergence is the ratio of the beam's effective length to its diameter, L/D. From this value it is possible to gauge the maximum achievable spatial resolution, d, using simple geometry

$$\frac{L}{D} = \frac{l}{d} \qquad \text{Equation 3.1}$$

where l is the distance between the sample under investigation and the detector. A higher L/D value equates to a more parallel beam and returns sharper images.

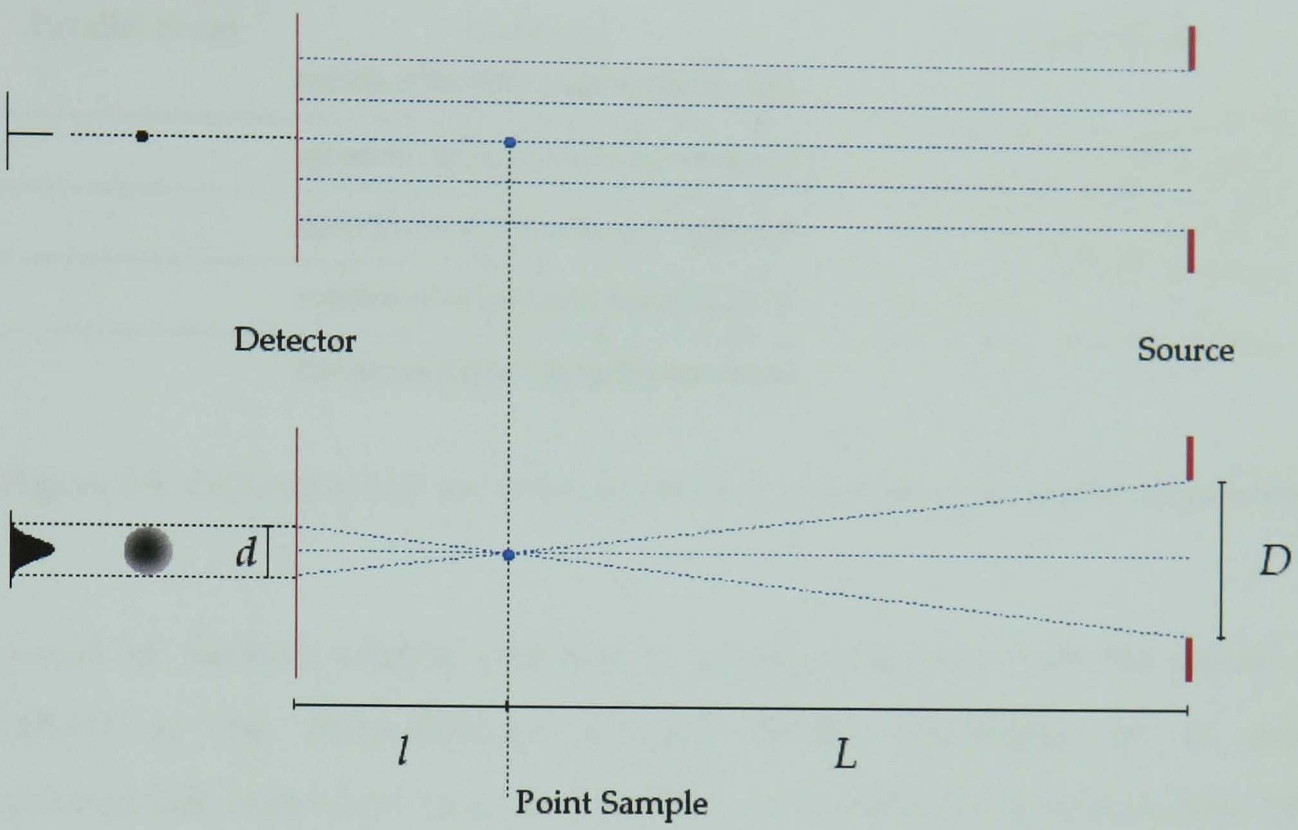

Figure 3.4: *A perfectly parallel beam (top) is the ideal situation for imaging, producing sharp images. Real beams have a measurable divergence (bottom), which limits spatial resolution.*

Of course, *L*/*D* could be increased arbitrarily by increasing *L* and/or decreasing *D*, but this is not without its drawbacks. A smaller beam diameter would decrease the field of view, and increasing the beam length, apart from potential impracticalities, would be detrimental to the available flux (the flux is inversely proportional to the square of the distance from the source). A further option is to place a collimator at the source, at the detector, or along the flight path. A collimator is a series of close-packed parallel channels in a radiation absorbing material such that only rays travelling in the direction of the channels are transmitted; all other radiation is absorbed (Figure 3.5). In essence, the parallelism of the beam is increased by removing any non-parallel components, and *L*/*D* now refers to the length of the collimator and the diameter of the channels. Inevitably, there will be a decrease in the flux, but the great advantage is the capacity to increase *L*/*D* without needing to lengthen the beamline or clip the field of view.

Two successful approaches to the trade-off between flux and divergence are the

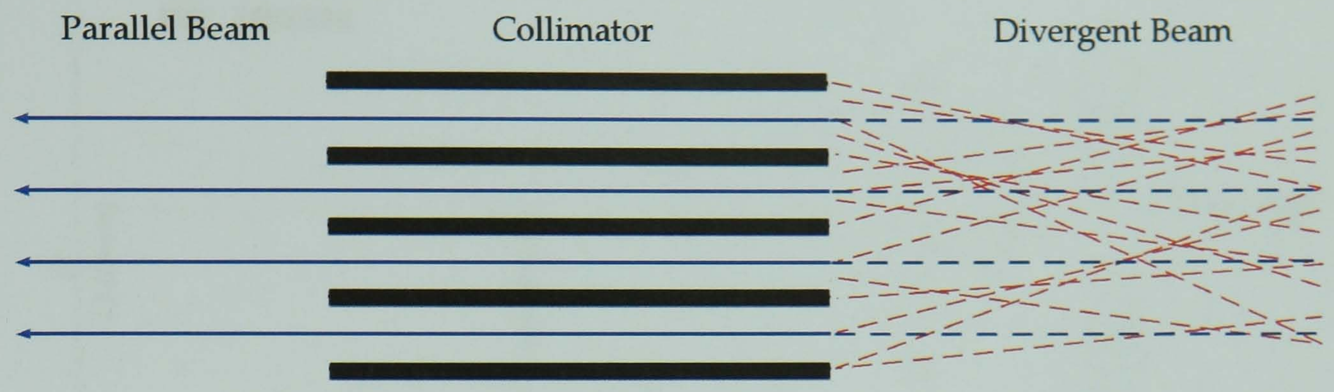

Figure 3.5: *Collimators increase beam parallelism by removing non-parallel components.*

provision of multiple sample positions at varying distances from the source (e.g. *CONRAD* at the Hahn-Meitner Institute, Berlin, Germany), or of several interchangeable collimators (e.g. *ANTARES* at the Forschungsneutronenquelle Heinz Maier-Leibnitz, Munich, Germany). Space constraints in the reactor hall encumber the former option for *Neutrograph,* but it is hoped to eventually furnish the beamline with a triple-barrel beam tube revolver in place of the current flight tube. The first tube will be empty (L/D ~150, flux ~3×10^9 $n\cdot cm^{-2}\cdot s^{-1}$; used for higher temporal resolution), the second tube will contain a collimator (L/D ~660, flux ~1×10^8 $n\cdot cm^{-2}\cdot s^{-1}$; used for higher spatial resolution), and the third tube will be left available for future installations.

The present horizontal divergence on *Neutrograph* has been measured by imaging a plate of sintered boron carbide (B_4C), *60 mm* wide and *2 mm* thick, at several distances, l, from the detection plane (Figure 3.6). Boron carbide is a strong absorber, so gives a high-contrast edge, which becomes increasingly distorted with increasing l, as illustrated by the attenuation profile plot (Figure 3.7). The "true edge" of the plate, the position of the edge in a perfectly sharp image, is estimated as the full width half maximum of the attenuation profile – a reasonable assumption, which measures the plate at *60.2 mm* wide. The width of the outside (inside) blurred region is calculated as the difference between the width of the plate and the distance between the point on either side of the plate where the attenuation is *10%* (*90%*) of the maximum. This width (the geometrical unsharpness) in each image is taken as a measure of the resolution, d, with which the plate edge can be determined. This method yields l/d (L/D) values of

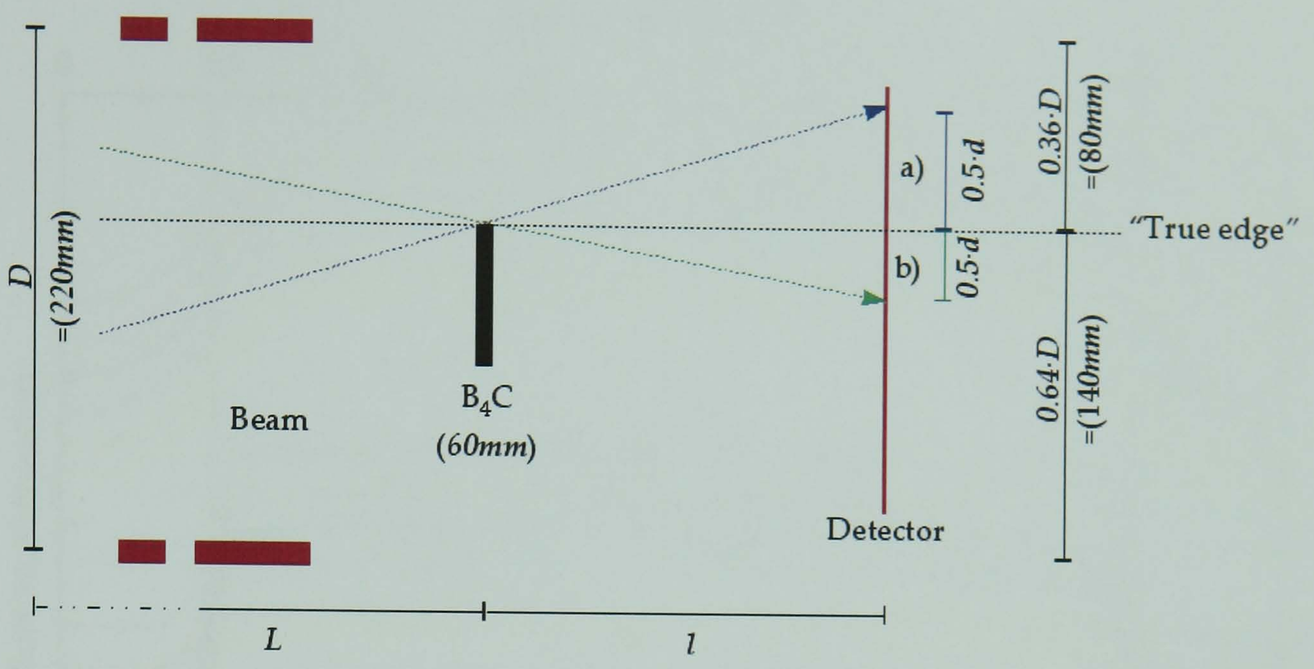

Figure 3.6: *The geometrical set up used to calculate L/D on Neutrograph. The beam divergence produces a blurred region (a) outside and (b) inside the "true edge" of the B_4C plate (horizontal black dashed line). A symmetrical effect would be produced by the opposite edge of the B_4C plate, but this is omitted for clarity.*

145 ± *7* and *151* ± *12* (Figure 3.8),which compare well with the value of *150*, an estimate based solely upon the geometry of the flight tube. Although not especially high, this is still competitive with other neutron facilities worldwide (Figure 3.9), and is capable of delivering a spatial resolution of *150-300 μm* at sample-detector separations of a few centimetres.

Since x-rays can, in effect, be emitted and detected at a point, some micro-tomography systems can achieve extremely high spatial resolutions down to *0.1 μm*. However, it is more informative to state that the actual resolution is *~1000* times smaller than the image field of view (this is approximately true for all imaging systems). Hence, for larger fields of view (in the range *~10 cm*) the resolution obtained with neutrons and x-rays is at least roughly equivalent. While ultra-high-resolution imaging has obvious benefits in being able to visualise very fine structures and details, it does bring some practical difficulties. Small variations in the motors used to manoeuvre and position samples, even vibrations, could disrupt an experiment. A shift of *1 μm* would almost certainly be undetectable at an image resolution of *100 μm* (being only a fraction of a pixel), but it would cause stark artifacts at a resolution of *1 μm*. Also, as pixel size

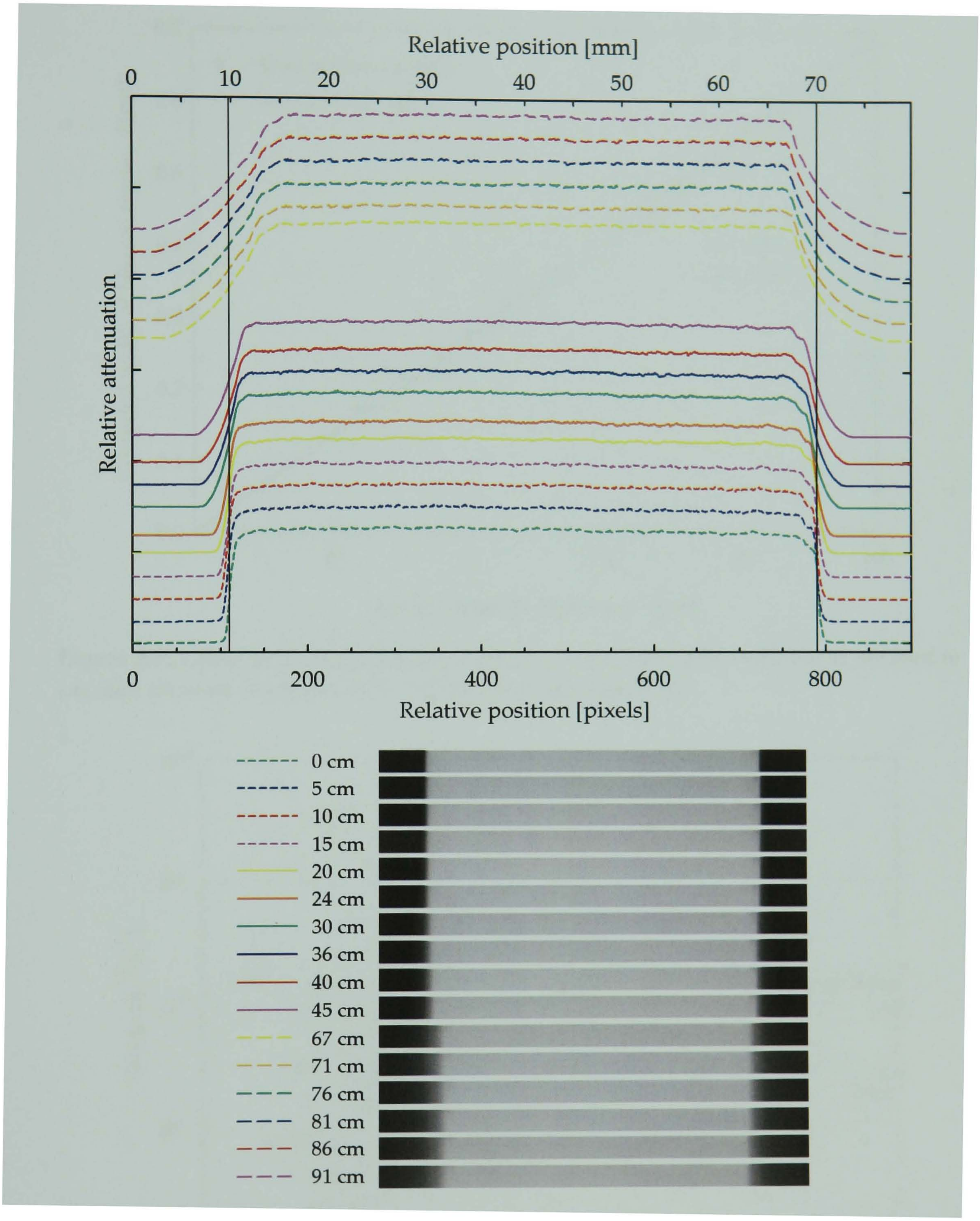

Figure 3.7: *Attenuation profile plots (top) and images (bottom) for a B_4C plate at various distances, l, from the detector. The spatial resolution, d, is calculated from the width of the blurred region. The vertical black lines indicate the position of the "true edges".*

becomes smaller, each pixel has a smaller field of view and accordingly receives a lower flux, which leads to an increase in the required exposure times.

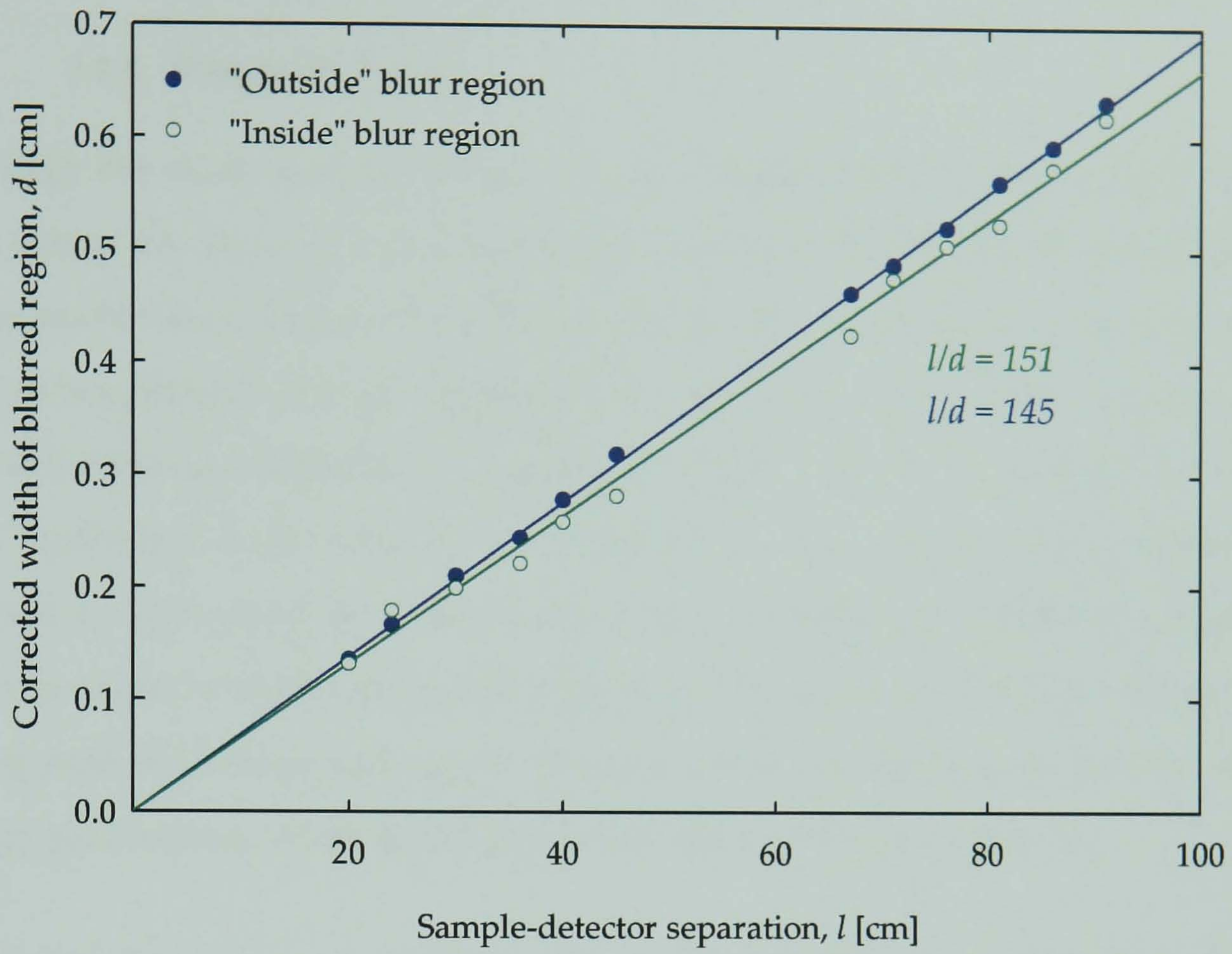

Figure 3.8: *Values for the sample-detector distance, l, and the spatial resolution, d, are used to calculate the beam divergence, L/D. The inverse gradient gives l/d.*

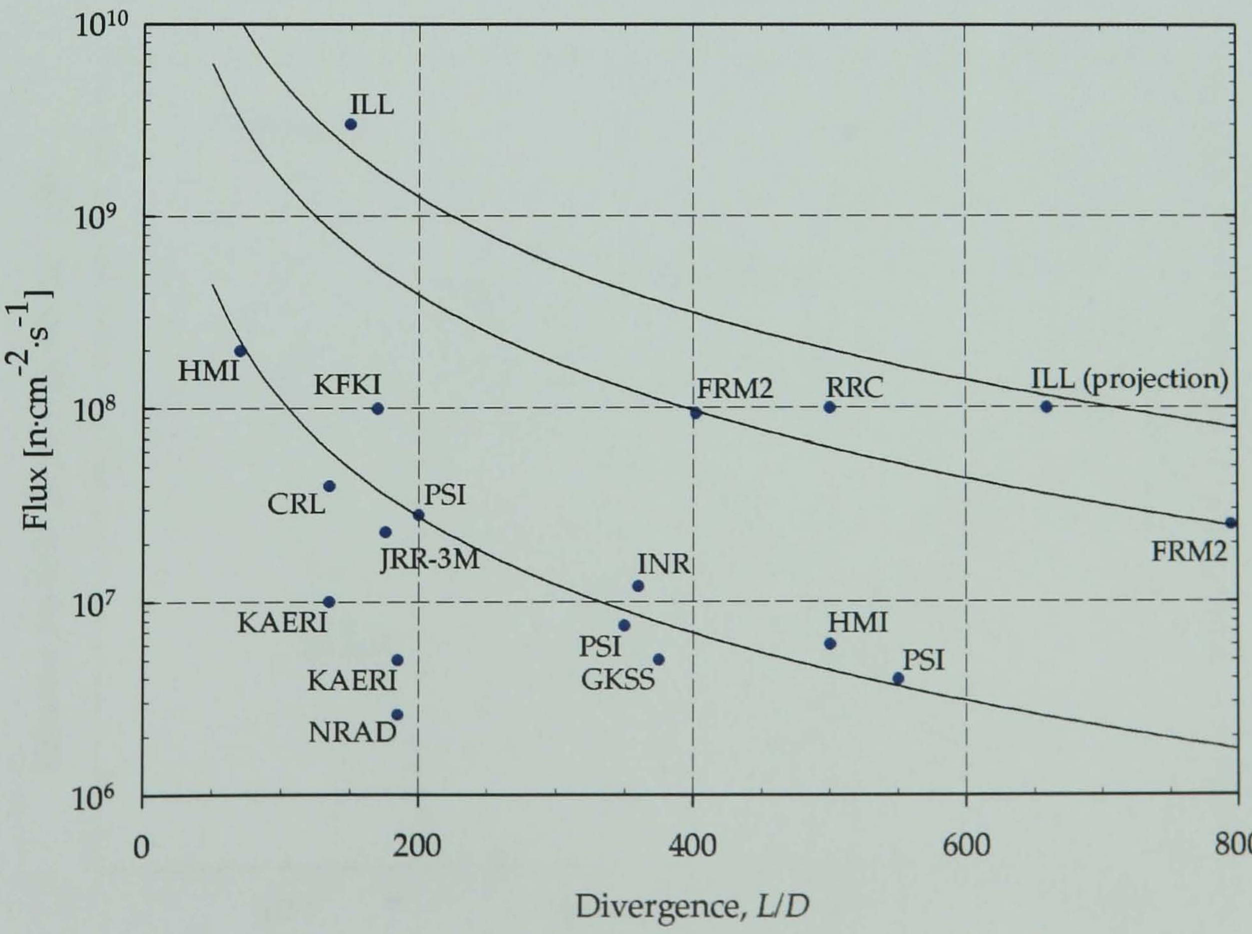

Figure 3.9: *The flux-divergence combinations of some world-leading neutron imaging facilities. The solid lines indicate the inverse dependence of flux on the square of the distance from the radiation source.*

3.2.4 Energy spectrum

Although the exact neutron energy spectrum at the experimental casemate has not been measured, there is no reason to expect that it might differ significantly from that of the reactor itself (Figure 3.10). The intensity at lower energies, where neutrons are approaching thermodynamic equilibrium with the moderator, is described by a broad Maxwell-Boltzmann distribution, peaking at *25 meV* (*300 K*) with a small contribution from epithermal (*~10%*) and fast (*~1%*) neutrons. Due to their lower probability of interaction, epithermal and fast neutrons will generally not contribute to imaging experiments (they will be attenuated very little) - those that are detected will serve only to augment the background signal. The beam also contains a large number of high energy gamma-rays, produced by the nuclear decay of fission fragments.

Thermal neutrons are well suited for imaging purposes, but cold neutrons are in some cases even more so because they have higher interaction cross-sections. This reduces

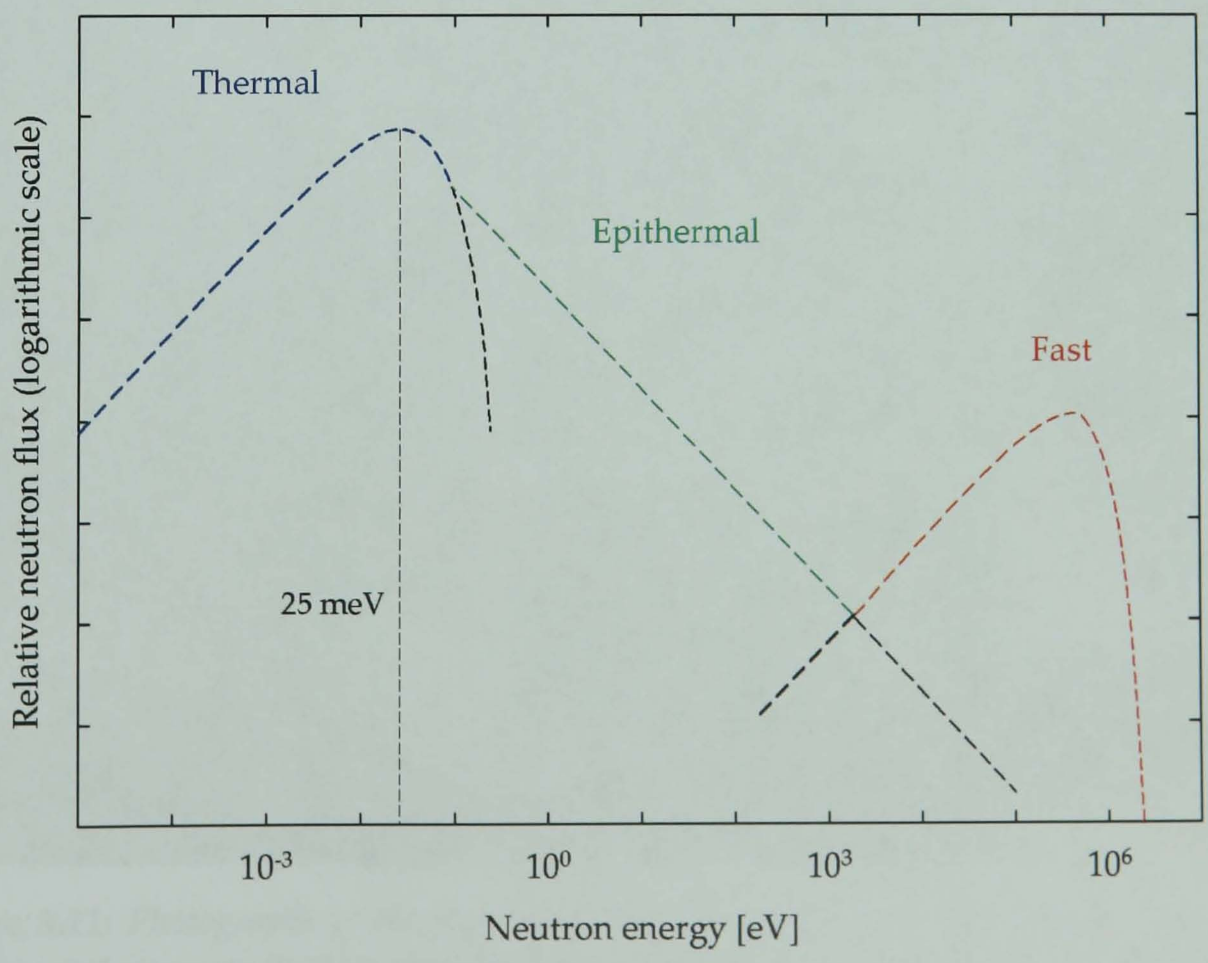

Figure 3.10: *A typical thermal reactor energy spectrum. The majority of the neutrons are thermal, peaking at 25 meV (300 K), with small epithermal and fast neutron components.*

the neutron penetrability, but has the benefit of increased sensitivity to these materials, and thus better contrast and higher detection efficiency. For this reason, some facilities utilise beams with high cold neutron components (e.g. *CONRAD* at the Hahn-Meitner Institute, Berlin, Germany).

3.3 Sample environment

Considering the extremely high radiation levels – $\sim 10^{12}\ n \cdot s^{-1}$ plus high intensity gamma-rays – effective shielding of the beamline and experimental zone is vital. The experimental casemate (Figures 3.1 and 3.11) is a high density concrete enclosure, the internal dimensions of which are *260×260×290 cm* (*w×l×h*). The front and rear walls (which cross the path of the beam), *100 cm* thick, and the side walls and roof, *80 cm* thick, are coated on the inner surface with a *5 mm* layer of rubberised boron carbide in order to reduce neutron activation. The floor is a *100 cm* thick block of standard

Figure 3.11: *Photographs of Neutrograph (left), the primary casemate (top centre), and the experimental casemate (bottom centre and right) showing (a) the primary beam shutter, (b) the flight tube, (c) the secondary beam shutter, (d) the linear motion table, (e) the lifting table, (f) the camera box, and (g) the neutron beam stop.*

concrete, which is overlaid with *50-100 mm* of lead beneath the sample position to protect the sensitive electronics housed in the reactor floor from any gamma-radiation scattered from the sample.

The neutron beam enters the experimental casemate via a *220×220 mm* aperture halfway up the front wall, which can be covered by a *45 mm* borated polyethylene secondary shutter to limit irradiation between individual exposures. On the back wall, directly in line with the beam, is a *5 mm* thick lithium fluoride beam stop (for neutrons) and beyond this, outside the casemate, lies a *100 mm* thick lead beam stop (for gamma-rays). The casemate is accessed from the rear by a winch-operated high density concrete door, *80 cm* thick. An interlock safety system prevents this door from being opened while the primary beam shutter is open and vice versa.

Further safety features include a warning light to signal when the beam is open, two surveillance cameras (monitored externally), an emergency stop/alarm button inside the casemate, a radiation detector that electronically holds the door locked until radiation levels stabilise below $100\ \mu Gy{\cdot}hr^{-1}$, and a carbon dioxide fire extinguisher.

3.3.1 Sample manipulation

Experiments on *Neutrograph* often require the ability to manipulate and align samples of various shapes, sizes and masses. Clearly, this cannot be done manually while the beam is open; sufficiently flexible mechanisation is needed to adjust samples in three dimensions. Moving a sample in a plane perpendicular to the beam propagation direction (up-and-down, and side-to-side) allows it to be positioned in the centre of the beam and thereby profit from the maximum possible flux, while rotation about the vertical axis is a requisite for tomography. Adjustments along the line of the beam are usually unnecessary as it is normally desirable to place samples as close to the detector as possible without disturbing (or being disturbed by) it. The vertical position of the sample is controlled by a manually-operated lifting table, on top of which computer-controlled linear and rotation stepper motion tables can be fixed (Table 3.1).

Table	Control	Axis	Range of motion *[cm]*	Precision of positioning	Maximum Load *[kg]*
Lifting	Manual	Vertical	90	~5 mm	300
Large linear	Computer	Horizontal	80	10 μm	30
Small linear	Computer	Horizontal	25	10 μm	5
Large rotation	Computer	Rotation	Continuous	0.0375 °	10
Medium rotation	Computer	Rotation	Continuous	0.0075 °	1
Small rotation	Computer	Rotation	Continuous	0.0025 °	0.5

Table 3.1: *Parameters of the motion tables used to align samples in the beam on Neutrograph.*

As on *Neutrograph,* large experimental facilities must perforce acquire projections for tomography by rotating the sample inside a static beam. Some smaller instruments, however, instead rotate the source-detector assembly around a static sample. This is particularly the case in x-ray equipment initially developed for medical applications, where patient comfort is of foremost concern.

3.4 Detector system

Radiography and tomography demand two-dimensional position-sensitive collection of data. A plethora of radiation detection options [38-40] is available (Table 3.2), and preference is based ultimately on two criteria: the time taken to expose and read-out (or develop) the image, and the maximum realisable spatial resolution. As a general rule, faster acquisition times tend to be connected with lower spatial resolution leaving substantial scope for compromise.

	X-ray film + neutron converter	Scintillator + CCD camera	Neutron imaging plate	Amorphous silicon flat panel	Track etch foil
Resolution *[μm]*	20 – 50	100 – 500	25 – 100	127 – 750	10 – 30
Exposure time *[s]*	300	10	20	5	900
Readout time	1500 s	10 ms	300 s	continuous	1500 s
Field of view *[cm²]*	30 × 30	30 × 30	20 × 30	30 × 40	10 × 10
Dynamic range	10^2	10^5	10^5	10^3	10^2
Linearity	non-linear	linear	linear	non-linear	linear
Digital format	8-bit	16-bit	16-bit	12-bit	8-bit
Detection efficiency		0.2 – 0.4		0.2	0.8
Comments	fast image series not possible, tomography impractical	real-time imaging possible	fast image series not possible	fast image series not possible	fast image series not possible, tomography impractical

Table 3.2: *Typical characteristics of some common neutron detectors used in imaging applications. (Values given are approximate and are intended only to give an idea of the performance of each system relative to the others.)* [40]

Since the neutron carries no net charge, it cannot be detected directly; capture or collision is required to produce detectable secondary particles or electromagnetic radiation. It is here that neutrons prosper most from antecedent imaging techniques, since a neutron conversion layer will transform much existing optical detection technology into neutron detection technology. *Neutrograph*'s detector is a scintillation screen in conjunction with a charge-coupled device (CCD) camera.

The scintillator is a homogeneous plastic sheet containing a conversion material, lithium-6 fluoride (6LiF), and a phosphor, copper-aluminium-and-gold-activated zinc sulphide (ZnS:Cu,Al,Au). The lithium absorbs neutrons to form energetic helium and tritium atoms

$$^{6}\mathrm{Li} + \mathrm{n} = {}^{3}\mathrm{H} + {}^{4}\mathrm{He} + 4.79\ MeV$$

which cause ionisation in the phosphor. Upon ionic relaxation, phosphorescent photons with a wavelength of *455 nm* (blue light) are emitted, stimulating electronic excitations. As the electrons return to their ground-states, they emit photons with a wavelength of *565 nm* (green light), which are detected by the CCD camera. The scintillator is also responsive to to gamma-rays, but the interaction cross-section is only ~10^{-4} that of neutrons.

The high density of lithium atoms, ~10^{22} cm^{-3}, and the high light yield, ~10^{5} emitted photons per captured neutron, mean the efficiency of the scintillator should be very high. This, however, is moderated by two counter influences. Firstly, the scintillator needs to be kept thin in order to suppress the likelihood of internal neutron and photon scattering (in other words, to limit the spot-size for the neutron-photon conversion process, which determines the resolution of the scintillator), which create spatial aberrations in the resulting images. Secondly, the scintillator is opaque to visible light, and only those photons emitted close to the surface will escape. As a consequence, the scintillators exploited on *Neutrograph* are *500 μm* thick, and have a conversion efficiency of *~30%* and a spot size of *~100 μm*.

Neutrograph uses two interchangeable CCD cameras – a PCO SensiCam for faster frame rates, and an Andor iXon for higher resolution and sensitivity (Table 3.3). The camera contains a semiconducting chip, which is covered by an array of microscopic, electrically-charged electrodes (photo-sites) each of which corresponds to one image pixel. Light impinging on a photo-site releases a number of electrons in proportion to its intensity, generating a voltage at that site. The voltage is read out and converted (using an analogue-to-digital converter) to an image grey value that scales with the magnitude of the attenuation of the material in the beam:

image grey-scale value $\propto$ photo-site voltage
$\propto$ number of photo-site electrons
$\propto$ impinging light intensity
$\propto$ neutron intensity at scintillator
$\propto$ attenuation by sample material

	PCO SensiCam [41]	Andor iXon [42]
Active Chip area *[pixels×pixels]* Pixel size *[μm^2]*	640 × 480 9.9 × 9.9	1004 × 1002 8.0 × 8.0
Quantum efficiency *[%]*	40 (at 550 nm)	65 (at 600 nm)
Operating temperature *[°C]*	-14	-75
Exposure time *[s]*	$10^{-3} - 10^{3}$ long mode $10^{-7} - 10^{-4}$ fast mode	10^{-3} - 10^{3}
Readout time *[ms]*	33 long mode 6.5 fast mode	33
Maximum frame rate *[Hz]*	30 long mode 154 fast mode	30
Digital format	12-bit	14-bit

Table 3.3: *Characteristics of the CCD cameras used on Neutrograph.*

In order to minimise radiation damage, the camera is situated far outside the neutron beam. This has the disadvantage that, since photons are emitted from the scintillator isotropically, only a tiny fraction of the light will ever reach the camera (the intensity scales inversely with the square of the separation). On the plus side, however, the space between the scintillator and the camera does provide the opportunity to enhance the optical quality of the image. A lens is used to focus the light onto the CCD chip, which allows the field of view to be enlarged considerably. Two mirrors are used to reflect the light through a total of $\pi/2$ ($\pi/4$ each) in order to remove gamma-rays, which would otherwise produce white spotting noise in images. The mirrors consist of a silicon wafer with a thin, sputtered layer of aluminium and coated with sapphire to stop oxidation.

The entire optical path from the scintillator to the camera is confined inside a box (Figure 3.12), which is light tight (to reduce background noise), made of aluminium (to limit neutron activation), painted matt black (to limit optical reflection and scattering), and shielded externally with boron carbide and lead (both to prevent radio-activation of the camera, and to reduce noise levels at the camera). The box is modular, with the

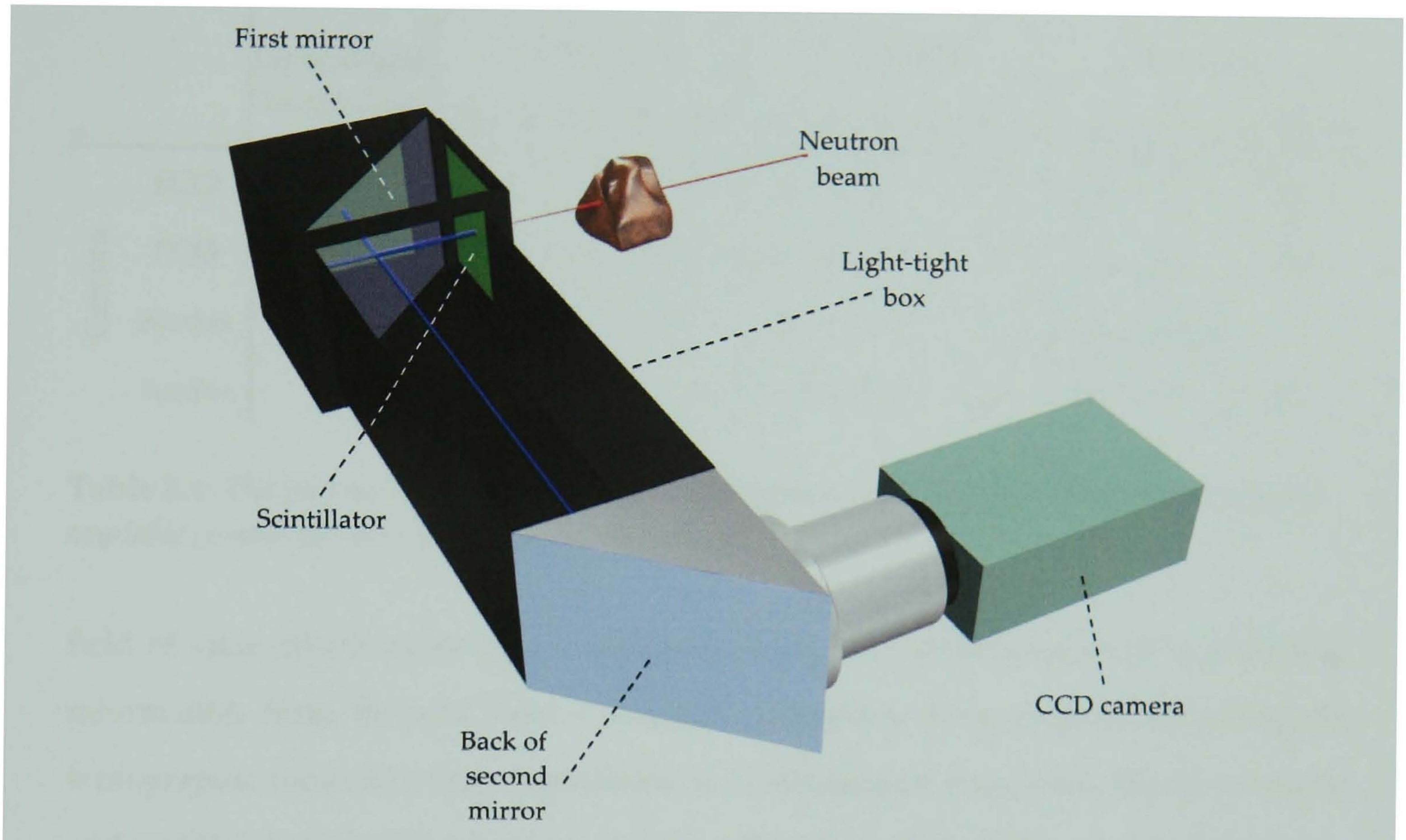

Figure 3.12: *Diagram of the camera box with the top removed. The neutron beam (red line) is converted to visible light (blue line) by the scintillator (yellow). The light is reflected by two mirrors before being detected by the CCD camera.*

housing for the first mirror and the second mirror at opposite ends, and a straight middle section, which comes in two sizes to allow variation in the length of the path – *70cm* or *100 cm*. Together with a selection of lenses – *35 mm, 50 mm* and *85 mm* – this brings diversity in the field of view projected onto the chip, and hence the pixel size (Table 3.4), and in the light intensity at the camera. It is perhaps worth pointing out that, as predicted by the Nyquist sampling theorem [43], the spatial resolution in any given image is (at least) twice as large as the pixel size.

3.5 Experimental set-up

The amount of time entailed in preparing samples, setting up equipment, and acquiring data depends heavily on the individual intricacies of the study undertaken, but, in general, it is relatively short. A standard set-up is minimal, involving only the alignment of the detector assembly with the beam, and fixing the sample within the

		Optical path length *[cm]*	*35 mm* lens		*50 mm* lens		*85 mm* lens	
			(a) *[w×h]*	(b) *[μm]*	(a) *[w×h]*	(b) *[μm]*	(a) *[w×h]*	(b) *[μm]*
Camera	PCO	70	11.9 × 8.9	185	8.4 × 6.7	131	4.5 × 3.3	70
	PCO	100	17.3 × 12.9	270	12.1 × 9.1	189	6.8 × 5.3	106
	Andor	70	15.2 × 15.2	151	10.6 × 10.6	106	cannot focus	-
	Andor	100	22.0 × 22.0	219	15.4 × 15.4	153	8.7 × 8.7	87

Table 3.4: *The (a) total field of view and (b) corresponding field of view per pixel given by the available combinations of camera and camera box.*

field of view. Much more time is normally needed to extract useful and quantitative information from the raw data – frequent processing steps include normalisation, tomographic reconstruction, quantification of attenuation properties, (hand-)selection and highlighting of salient features, and visualisation and rendering of data volumes.

Since both the scan field and tomography reconstruction volume is cylindrical (each slice being circular), the most efficient sample geometry is also a cylinder. Thus, whenever possible, it is preferable to opt for a cylindrical sample.

3.6 *Neutrograph*'s current capabilities

Undoubtedly, the major downside of using neutrons over x-rays is the maximum spatial resolution presently attainable, and this is the critical factor in most imaging applications. Some recent developments using gadolinium oxide scintillators have managed to achieve a resolution of *~50 μm* [44], but, until the new collimators are installed, the high divergence, not to mention that the cameras are focussed manually, will ensure that Neutrograph lags the field in this regard. Using a pinhole geometry is one possibility in partially rectifying this situation, but here *Neutrograph* suffers from a lack of space since a large cone beam field of view requires the pinhole to be located far from the sample position, and any beam modification must be done downstream of Lohengrin: in this case, a pinhole will give a microscopic field of view. Although still useful in performing high-resolution raster scanning of macroscopic samples, this is a very time-consuming method and higher resolution instruments (e.g. *CONRAD* at the Hahn-Meitner Institute in Berlin, Germany; and *NEUTRA* at the Paul Scherrer Institute, Villingen, Switzerland) are already beginning to produce comparable results much more efficiently [44]. Instead, the key applications of Neutrograph are those that focus on its strengths – those requiring a large field of view (large samples) and/or high flux (imaging fast dynamic processes and discrimination of low-contrast materials (Section 4.3)).

4 Data Evaluation

It is worth bearing in mind that a high spatial resolution is not the sole objective of radiographic imaging. Indeed, it would be entirely meaningless without the ability to also discern disparities in the intensity of the beam transmitted through different materials (or thicknesses) and, therewith, to form an image with identifiable contrast. High quality imaging thus relies on the precision and accuracy with which the beam intensity can be measured, as limited by systematic and statistical errors and the degree to which they can be corrected or minimised.

4.1 Image normalisation

Raw data always require two corrections: an offset related to fluctuations in the electronics of the CCD camera (dark current, readout noise and analog-digital conversion), and a normalisation related to inhomogeneities in the beam intensity and in the detection efficiency of the scintillator and the CCD chip. The magnitude of the dark noise offset, which can be reduced and stabilised (although not eliminated) through cooling, is found by measuring an image with no incident photons, i.e. an image where the neutron beam shutters and the internal camera shutter are closed. Normalisation is to the unperturbed or open beam, i.e. the intensity of the beam with nothing in the field of view. The beam attenuation, A, (Equation 2.2) is then given by

$$A = \int \alpha \, \mathrm{d}s = -\ln \frac{I}{I_0} = -\ln \left(\frac{\iota - \omega}{o - \omega} \right) \qquad \text{Equation 4.1}$$

where ι is the sample image, o is the open beam image, and ω is the dark image.

4.1.1 Image normalisation to a reference image

In some circumstances involving studies of dynamic processes, rather than normalising data images to the open beam, it can be more propitious to normalise data images to a reference image in which the state of the system being studied is known. Good examples of this might be an empty sample holder or the initial conditions of the system being studied. In this way, data are corrected not only for inherent instrument inhomogeneities, but also for intensity variations resulting from particular parts of the sample. In effect, the presence of the sample environment can be removed so that only changes in the system are visualised (Figure 4.1). This can be particularly useful when the attenuation caused by fluctuations in the system are much smaller than the total attenuation of the sample.

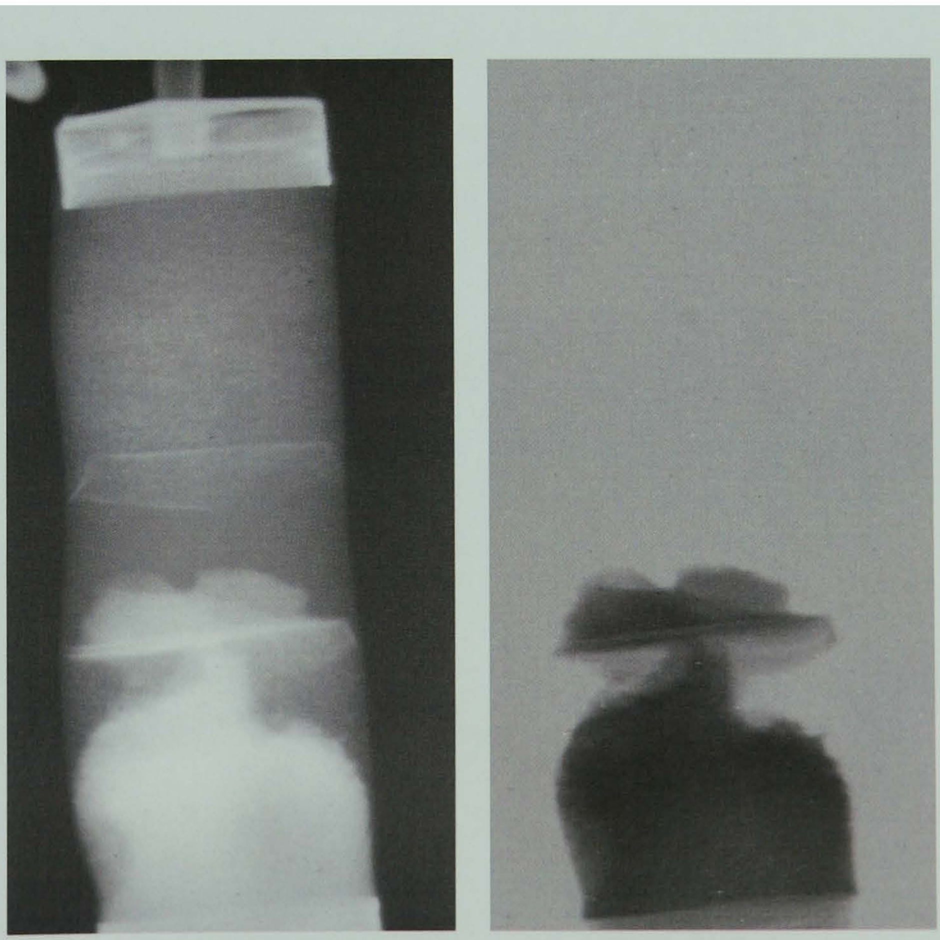

Figure 4.1: *The same radiographic image of water flowing through synthesised sandstone as normalised to the open beam to show the flow in the sample (left), and to initial conditions to show only the flow (right).*

4.1.2 Scintillator degradation and burning

As the scintillator is exposed to the neutron beam it is consumed and degrades, reducing the detection efficiency (and therefore the amount of light emitted) at an exponential rate that depends on the neutron intensity incident upon it (Figure 4.2). Consequently, those areas of the scintillator that are shielded from the beam by the sample remain, on average, more efficient and glow brighter. If samples are irradiated for long periods of time, this results in an image of the sample being burned onto the scintillator (Figure 4.3). This is corrected for during image normalisation, but, due to the ever-changing state of the scintillator, each open beam image must be measured either immediately before or immediately after the sample image. During longer experiments open beam images are taken intermittently throughout, with points in between calculated via linear interpolation. It is not clear whether the degradation is due to the conversion (and subsequent loss) of lithium to helium and tritium, or to scintillator damage caused by other particles in the beam (alpha particles, etc.).

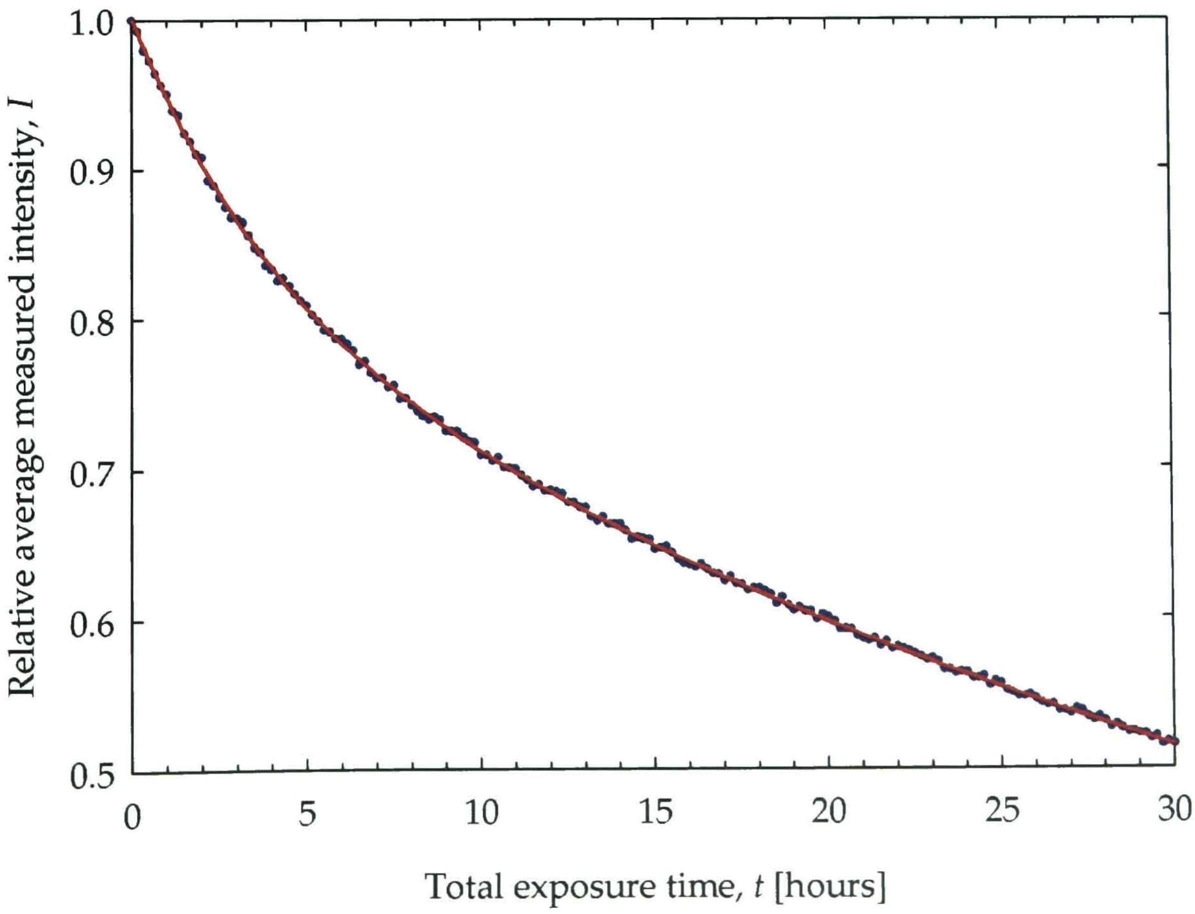

Figure 4.2: *A plot showing the measured scintillator degradation (blue points) and an exponential decay function (red line).*

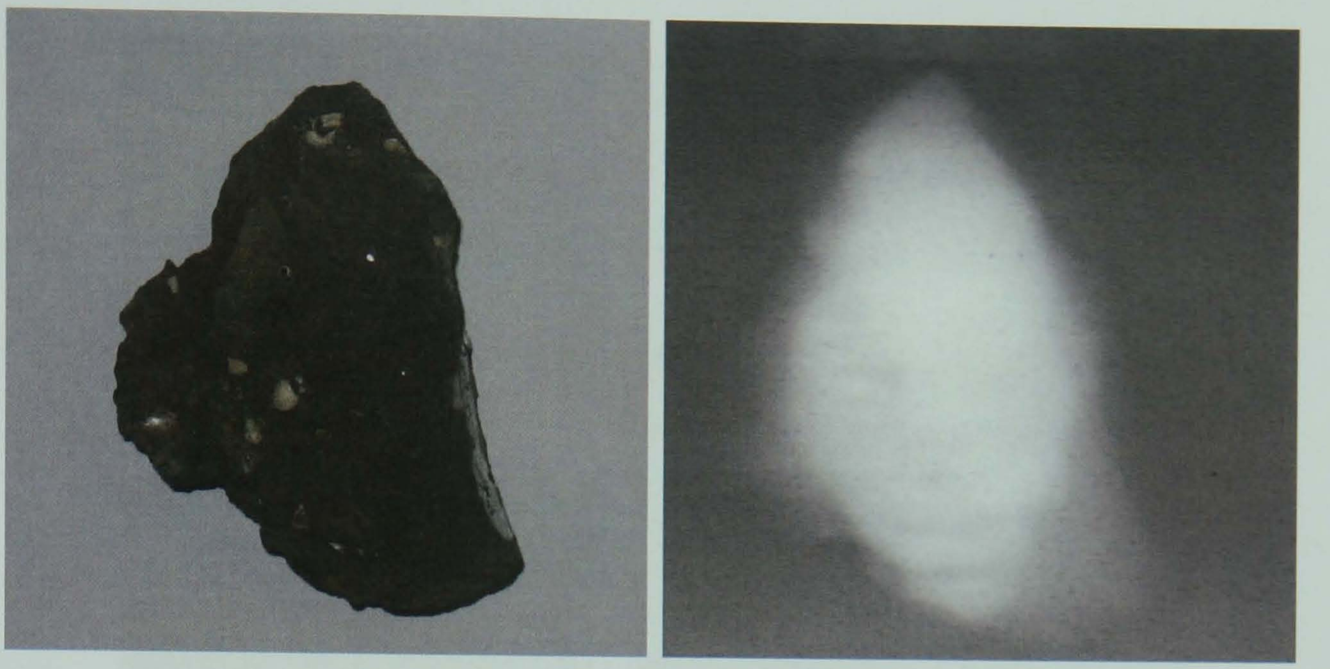

Figure 4.3: *A photograph of a fossil-containing rock (left) and an open beam image showing the rock's form burned onto the scintillator (right).*

4.2 Gamma noise minimisation

A major factor affecting the quality of images acquired on *Neutrograph* is the high gamma-ray flux coming both from radioactive decay within the reactor and from neutron activation of materials along the flight path. Any gamma photons impinging on the CCD chip will saturate the pixel(s) at that site, resulting in the complete loss of information at the corresponding point(s) in the subsequent image (appearing as white spots). Shielding with lead is very effective, but, unavoidably, always incomplete because the optical path to the camera must be left open to light emitted by the scintillator.

The existing solution is to calculate each image pixel as the mean value from multiple separate exposures; it being unlikely that gamma-spots will consistently occur in the same positions, their presence is averaged out and subdued (Figure 4.4). Despite some manifest flaws in this approach – it is not viable when investigating fast dynamic processes and it is not truly a filter for removing gamma-spots – it is, nonetheless, effective in most circumstances. Typically *100* exposures per image are sufficient, although, when time is limited, even *10* exposures per image give a notable improvement.

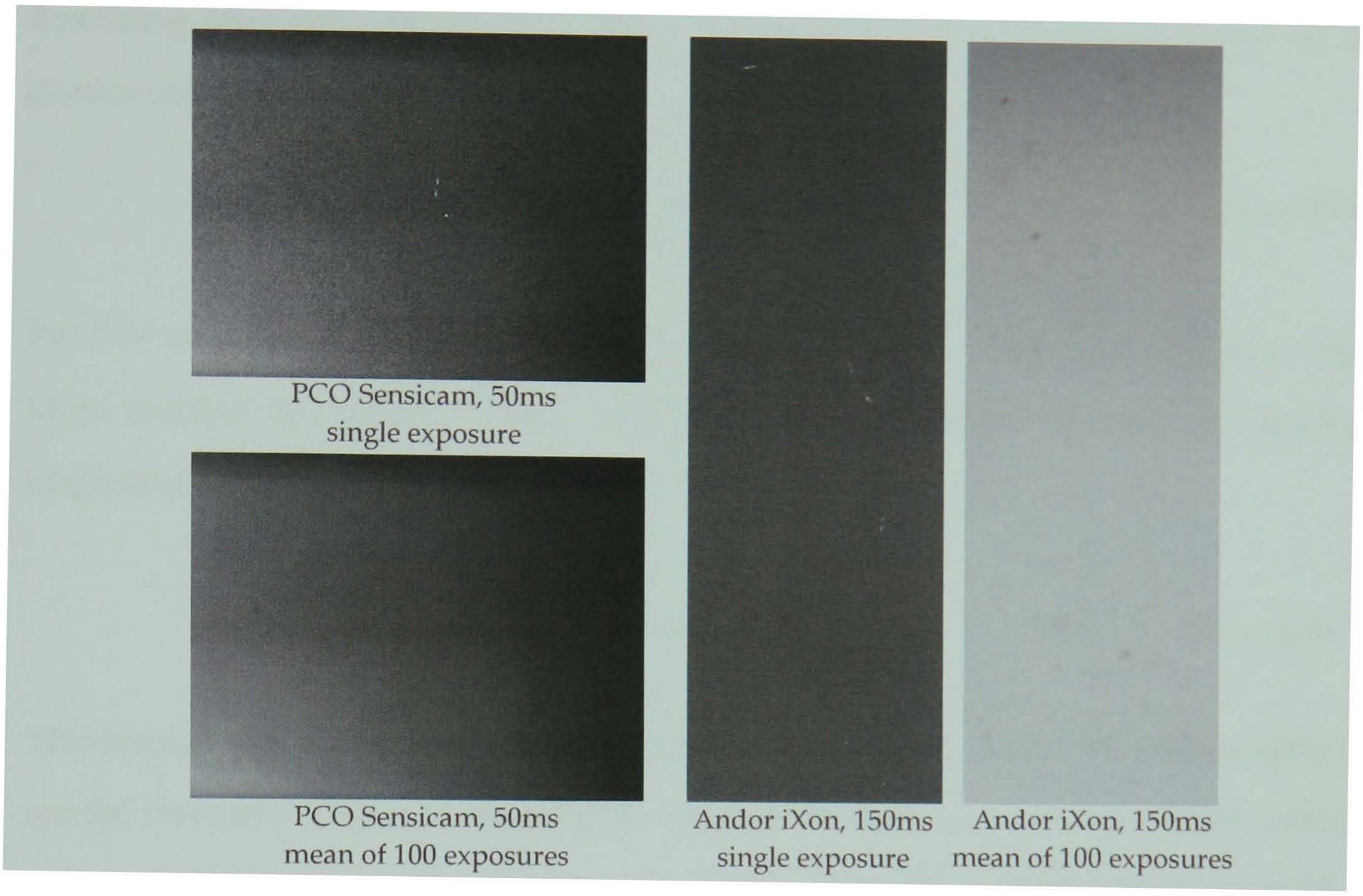

Figure 4.4: *Gamma noise (white spots) minimisation by averaging over multiple exposures. The darker spots indicate scintillator inhomogeneities.*

4.3 Contrast sensitivity

The beam attenuation, A, calculated from data collected in time, t, is given by (from Equation 4.1)

$$A = -\kappa \ln \frac{I}{I_0} = -\kappa \ln \left(\frac{\mathrm{d}N/\mathrm{d}t}{\mathrm{d}N_0/\mathrm{d}t} \right) \qquad \text{Equation 4.2}$$

where N is the number of transmission neutrons (taken from the data image), N_0 is the number of incident neutrons (taken from the open beam image), and κ is some coefficient related to the detection efficiency. Note that, because the attenuation information is transferred via multiple carriers during the imaging process (neutrons → photons → photons → electrons), N and N_0 should, strictly speaking, refer to the carrier that is least abundant. This is assumed to be neutrons since each conversion stage augments the number of carriers, but, in any case, the number of carriers would still be proportional to the number of neutrons, and the following discussion is still valid.

Assuming that other errors have been corrected or are negligible, the error in the attenuation is given by

$$\Delta A = \kappa \sqrt{\left(\frac{\Delta N}{N}\right)^2 + \left(\frac{\Delta N_0}{N_0}\right)^2} \qquad \text{Equation 4.3}$$

but this can be rewritten in terms of the standard deviation associated with counting a large number of random events, $\Delta N / N = 1/\sqrt{N}$ (recall that the neutron emission originates from radioactive decay).

$$\Delta A = \kappa \sqrt{\frac{1}{N} + \frac{1}{N_0}} \qquad \text{Equation 4.4}$$

This implies that a greater number of detected neutrons per unit area (as defined by the spatial resolution) leads to statistically superior data (data in which statistical noise is suppressed). Furthermore, as only attenuation differences greater than ΔA will be perceivable, such images will also have better contrast sensitivity. In this respect, a high neutron flux is clearly advantageous, especially in circumstances where the attenuation variation is only very slight. While true that it is possible to compensate for a decrease in flux with a proportionate increase in image exposure times (the physical limit of which is the point of detector saturation, whether by neutrons or gamma rays), this is not feasible when studying fast dynamic processes and may make the time-scale for other experiments (tomography, for example) impractically long.

It is in the regime of yielding statistically accurate results and good contrast with relatively short exposure times that *Neutrograph*, with its unrivalled flux, truly excels; a single radiographic image can require as little as *1 ms* exposure (although *50-250 ms* is more usual). Radiography measurements show that a ~*15 μm* thick polythene sheet is detectable with an exposure time of only *1.5 s* (*50×30 ms*), as is the ~*15 μm* thick layer of adhesive on the back of the aluminium tape used to secure it (Figure 4.5). This is equivalent to a beam attenuation of *0.0105*. The error in this value (as estimated from a region of constant attenuation) is *0.0009*, which is larger than the theoretical value of *0.0004* (from Equation 4.4, assuming a flux of $3\times10^9\ n\cdot cm^{-2}\cdot s^{-1}$, a pixel size of *150 μm*, and $\kappa = 0.3$), although it does include extra error contributions (gamma rays, etc.).

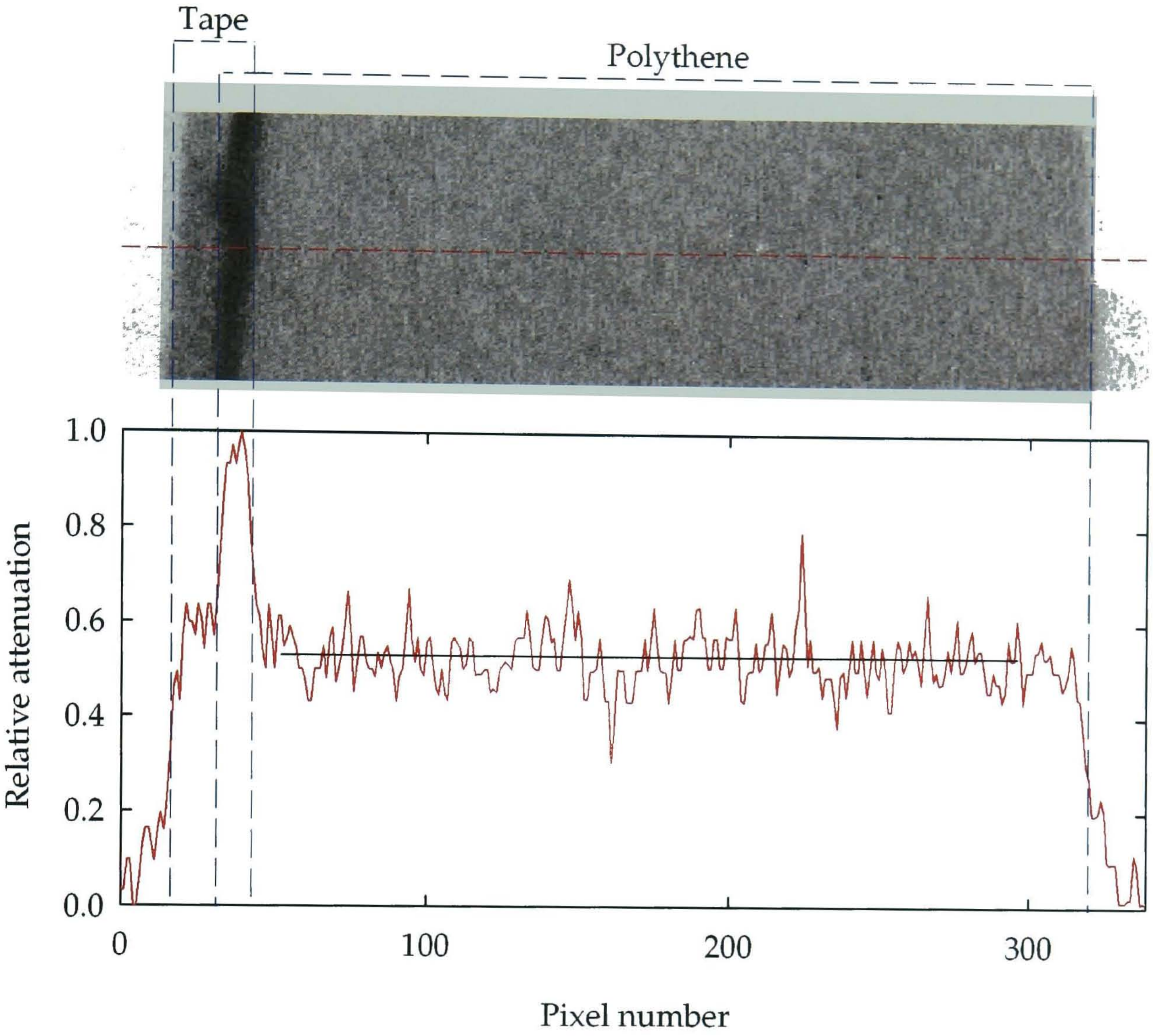

Figure 4.5: *Radiographic image of a sheet of polythene ~15 μm thick. The plot shows the attenuation profile along the red dashed line, and the mean (solid black line) in a region of constant attenuation.*

The statistical improvements that accompany higher flux can be seen by comparing reconstructed slices of the same sample (a monkey puzzle fossil inside a rock matrix) generated from tomography projections collected in similar experiments on *ANTARES* (at the Forschungsneutronenquelle Heinz Maier-Leibnitz, Munich, Germany) and on *Neutrograph* (Table 4.1 and Figure 4.6). It is important here not to place too much emphasis on the contrast between the fossil (lighter areas) and the rock matrix, since any inconsistencies may also be explained by differences in the neutron beam energy spectra; *Neutrograph* uses thermal neutrons, whereas *ANTARES* uses cold neutrons. Rather, it is the graininess that is significant. Also noteworthy is that fact that the slice reconstructed from the *ANTARES* data is visibly much sharper, owing to the much lower beam divergence.

	Neutrograph	*ANTARES*
Flux *[n·cm^{-2}·s^{-1}]*	3.0×10^9	2.5×10^7
L/D	150	795
Total rotation angle	π	π
Number of Projections	801	401
Exposure per projection *[s]*	10 [100×100 *ms*]	30 [1×30 *s*]
Total time for experiment *[mins]*	~200	~200

Table 4.1: *Experimental parameters used for a tomographic study of a fossil on two instruments, Neutrograph and ANTARES.*

Figure 4.6: *Slices of a monkey puzzle fossil reconstructed from data collected on Neutrograph (left) and ANTARES (right).*

4.3.1 Attenuation as a limit on spatial resolution

The beam attenuation, as given by $A = \alpha \cdot s$, is a measure of the probability that any given neutron passing through matter will interact (preferably be absorbed) within a length, s. As the thickness of the material tends towards zero, the probability of absorption also tends towards zero, and the material becomes undetectable (even if it is macroscopic in the plane perpendicular to beam propagation). This introduces a restriction on the dimensions of discernible features that is unrelated to the beam divergence, detection spot size or detector resolution. Clearly, the detectable thickness varies from material to material, but for a typical neutron linear attenuation coefficient of $0.1\ cm^{-1}$, a material thickness of $1\ \mu m$, a neutron flux of $3 \times 10^{9}\ n \cdot cm^{-2} \cdot s^{-1}$, and a pixel size of $200\ \mu m$, in order to achieve a (modest) noise level of $<10\%$ a single radiographic image would theoretically require a total exposure time of $\sim 10^{4}\ s$.

Of course, x-rays also experience this limitation, but it is generally less severe because x-ray linear attenuation coefficients are typically an order of magnitude higher than those of neutrons. It is also possible to reach much higher fluxes with x-rays than with neutrons ($\sim 10^{21}\ ph \cdot s^{-1}$ at the European Synchrotron Radiation Facility compared with $\sim 10^{12}\ n \cdot s^{-1}$ at the Institut Laue-Langevin), and it is also easier to focus x-rays to obtain even higher beam intensities (at the expense of the field of view).

In some instances it is possible to greatly improve the contrast by carefully and selectively altering the material in present in a region of interest - either by introducing additional material or by completely replacing the material with a new one. This contrast agent is usually chosen to be either a strong or a weak absorber (depending on the other materials present in the sample) such that the region of interest will contrast well with neighbouring regions. For neutrons, good examples of the former case are boron (or borated materials such as boron carbide or borated aluminium), water-soluble gadolinium salts, liquid gadolinium, and helium-3 (although infusing and containing a gas presents its own difficulties). The latter case may be particularly desirable (for example) with water, which may be exchanged with heavy water; water is a strong scatterer, while heavy water is not.

4.4 Scattering as a limit on spatial resolution

Scattering is not true attenuation, since the overall intensity of the beam is not reduced, but merely redistributed. This not only leads to blurring in resulting images, but some scattered neutrons will inevitably impinge arbitrarily upon the detector, causing a background signal and skewing the measured attenuation (the measured intensity will be higher than otherwise expected in these regions). Although the scattered signal is weaker than the straight-through signal, it is nonetheless detectable (Figure 4.7). Its strength increases with the path length, and provides the source of a physical limit on the attainable spatial resolution and contrast sensitivity.

Although the neutron's sensitivity to hydrogen is often viewed as one of its key plus-points in terms of imaging applications, it is important to realise that the vast majority of the neutron interaction cross-section of hydrogen is in the form of isotropic scattering (thermal neutrons: $\sigma_{scattering}=82.03$ *barn*, $\sigma_{absorption}=0.33$ *barn*) and to be aware of the effects that this will have in resulting images.

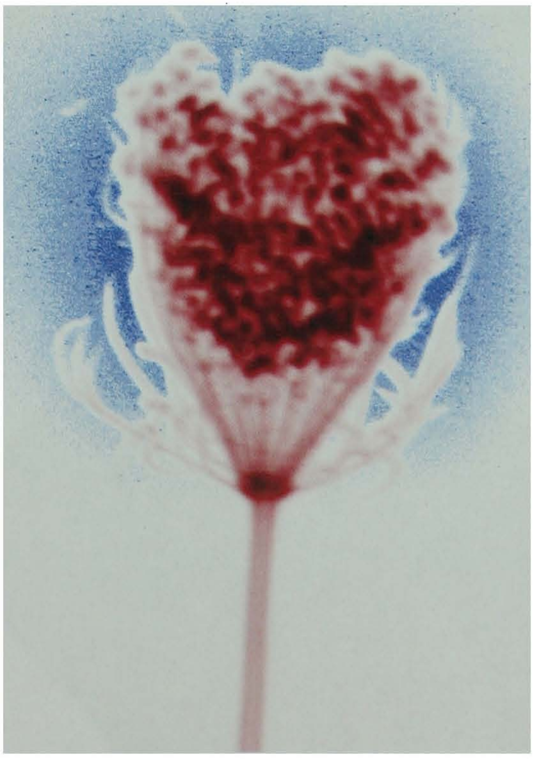

Figure 4.7: *A radiographic image of a thistle showing the attenuation of the straight-through beam (red) and a halo region of scattering around highly hydrogenous head (blue). The intensity of the scattered signal is ~3% that of the straight-through signal and would not be apparent in a standard grey-scale image .*

4.5 Reconstruction artifacts

The visual nature of imaging data means that it is relatively straightforward to explain and understand. However, artifacts caused by spurious, incomplete or missing data can lead to misrepresentations of the shapes of structures and the materials from which they are made, creating problems in eliciting quantitative information. Thus, it is important, although not always easy, to separate these errors from the real features.

4.5.1 Ringing

Ring artifacts arise when one or more pixels on the CCD chip consistently and systematically produce different signals to the ones surrounding them when exposed to light (i.e. they are not corrected by the dark image offset). In reconstructions these pixels produce a series of concentric rings around the axis of rotation (Figure 4.8). This can be particularly problematic when investigating samples that are either cylindrical or radially varying, where the rings may be mistaken for real properties.

Because they are present (if not always apparent) in all projections, these over-active pixels can easily be seen in the sinograms, where they produce vertical lines (Figure 2.5). At this stage it is possible to apply simple averaging correction filters, although this will inevitably lead to some degree of erasure or blurring. The presence of ringing can also be reduced experimentally, by varying the vertical position of the sample

Figure 4.8: *An example of ring artifacts in a reconstructed slice from a fossilised piece of whalebone.*

throughout data collection and realigning the projections afterwards such that the effect of the over-active pixels becomes smeared over multiple slices. The former strategy is not currently implemented in the reconstruction software used on *Neutrograph*, and, because the lifting table on *Neutrograph* is manually operated, the latter approach is not feasible.

4.5.2 Beam hardening

When a polychromatic beam passes through a thick or highly attenuating sample, the lower energy part of the spectrum is attenuated more readily than the higher energy radiation, resulting in a hardening of the beam. Although diminished in overall intensity, the average energy of the beam is increased, meaning that it passes through matter more easily. Consequently, as the beam propagates the effective attenuation coefficient of any material encountered decreases, giving the impression that longer paths are proportionally less attenuating than shorter paths (where beam hardening is less acute). This manifests itself in tomographic reconstructions as a darkening in the middle of long paths and a corresponding brightening at the edges. In the case of homogeneous samples, artificially lowered attenuation measurements translate to an apparently lower density towards the centre and a corresponding cupping in the attenuation profile.

The most effective way of avoiding beam hardening is to monochromate the beam using either a mechanical velocity selector or monochromating crystals [45, 46]. The problem with doing so, however, is that monochromation reduces the beam intensity, and image acquisition times are subsequently much longer. For this reason, monochromatic beams are generally only used for more specialised applications such as those in the developing field of Bragg-edge imaging [47-49]. Two further solutions to beam hardening are commonly employed. The first is to ensure that the beam is energetic enough to penetrate by filtering low energy components out of the beam before passing it through the sample. However, because higher energy radiation is less sensitive to changes in the material along the path, it may prove incapable of differentiating between regions of interest. The second is to scan a calibration phantom with similar attenuation properties to those of the sample in order to find the relationship between sample thickness and effective attenuation. This can then be used to correct each projection prior to reconstruction. However, this is limited to situations where the sample is (at least roughly) uniform in both material and density, and also requires knowledge of the sample thickness along every path; clearly this becomes very difficult when looking at geometrically irregular objects.

Beam hardening effects are well demonstrated by a neutron tomographic study of an assemblage of graptolite skeletons (graptolites are a class of extinct colonial marine invertebrates that were a major macroplanktonic element of the Early Palaeozoic seas (*500-400* million years ago)) discovered near Llandidloes in Powys, Wales. The skeletons are mostly carbon with an infilling of pyrite (FeS_2), inside a carbon-rich mudstone block (*130×42×39 mm*). X-ray radiography had already demonstrated that graptolites are abundant along the bedding planes of the sample (Figure 4.9), but neutrons reveal very few of them. In spite of the approximate homogeneity of the sample, the centre of each slice, as well as a stripe along the two longest paths

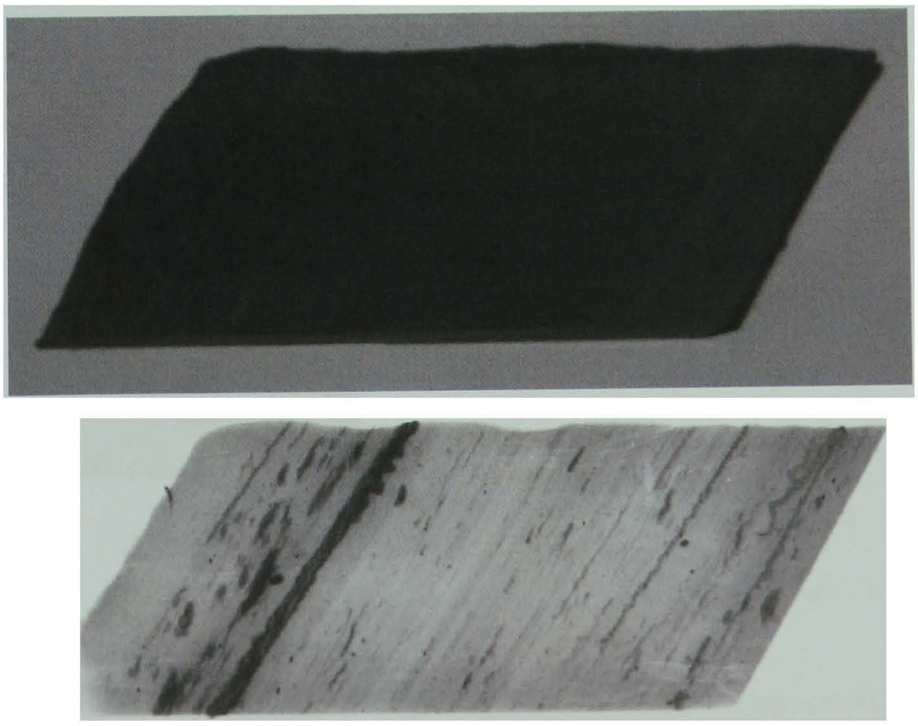

Figure 4.9: *A photograph (top) and an x-ray radiographic image (bottom) of graptolite fossils in a mudstone matrix.*

(diagonally from corner to corner), is anomalously ~60% less attenuating than the edges (Figure 4.10). Although x-rays would be expected to give better contrast anyway (thermal neutrons: $\sigma\{C\}$=*5.55 barn*, $\sigma\{FeS_2\}$=*17.70 barn*; *100 keV* x-rays: $\sigma\{C\}$=*3.00 barn*, $\sigma\{FeS_2\}$=*55.84 barn*), the neutrons' failure to sufficiently penetrate the sample undoubtedly exacerbates the situation.

The extent of the beam hardening can be seen by comparing the attenuation profile of the projections where the block's shortest cross-sectional axis (*39 mm*) and where its longest cross-sectional axis (*57 mm*) is parallel to the beam propagation direction. Despite there being a *50%* difference in the maximum thickness, the effective attenuation along these axes differs by only ~*10%* (Figure 4.11). Calculations of the true attenuation, based on measurements of the attenuation along short paths and assuming a homogeneous and regular sample, estimate the maximum thickness of this material that is penetrable before beam hardening begins to become noticeable to be ~*19 mm*.

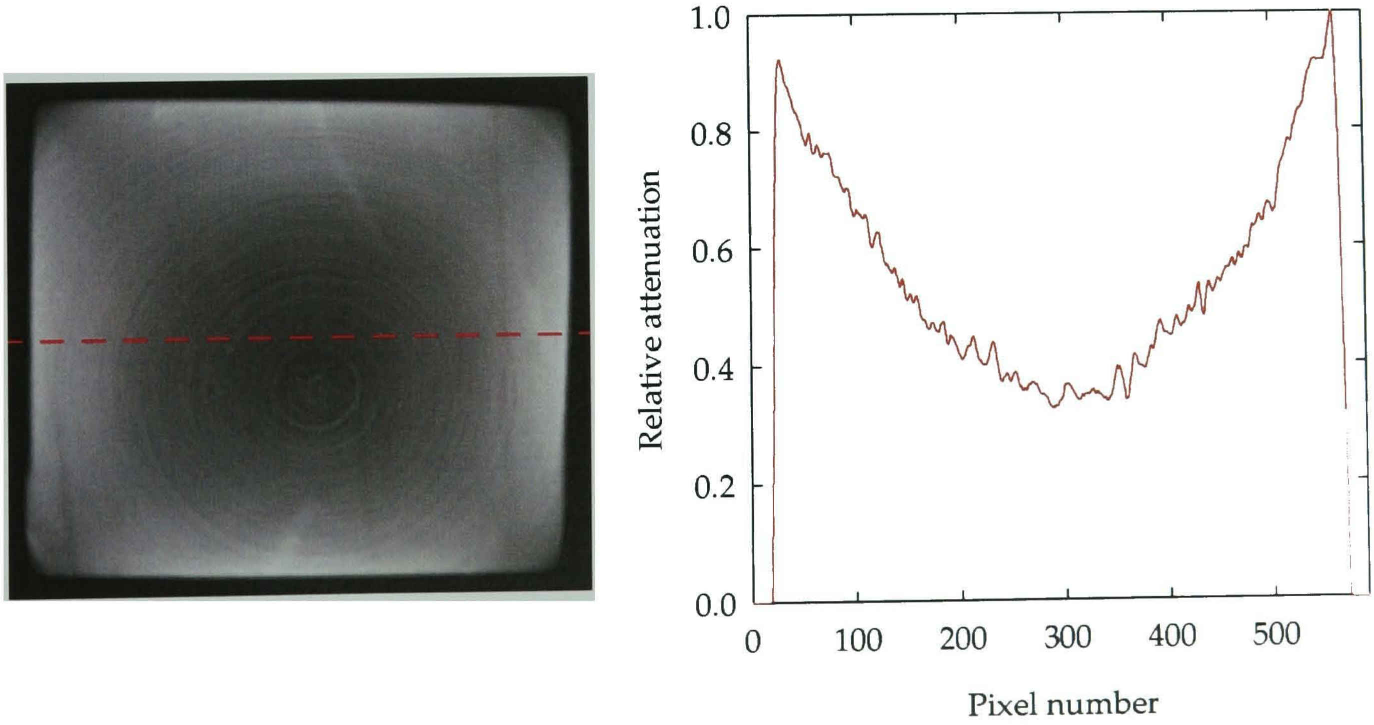

Figure 4.10: *Beam hardening causes a cupping in the attenuation profile (right) across the centre of a reconstructed slice (left) of the graptolite fossils. The white diagonal streaks at centre-top and centre-bottom of the slice are graptolites.*

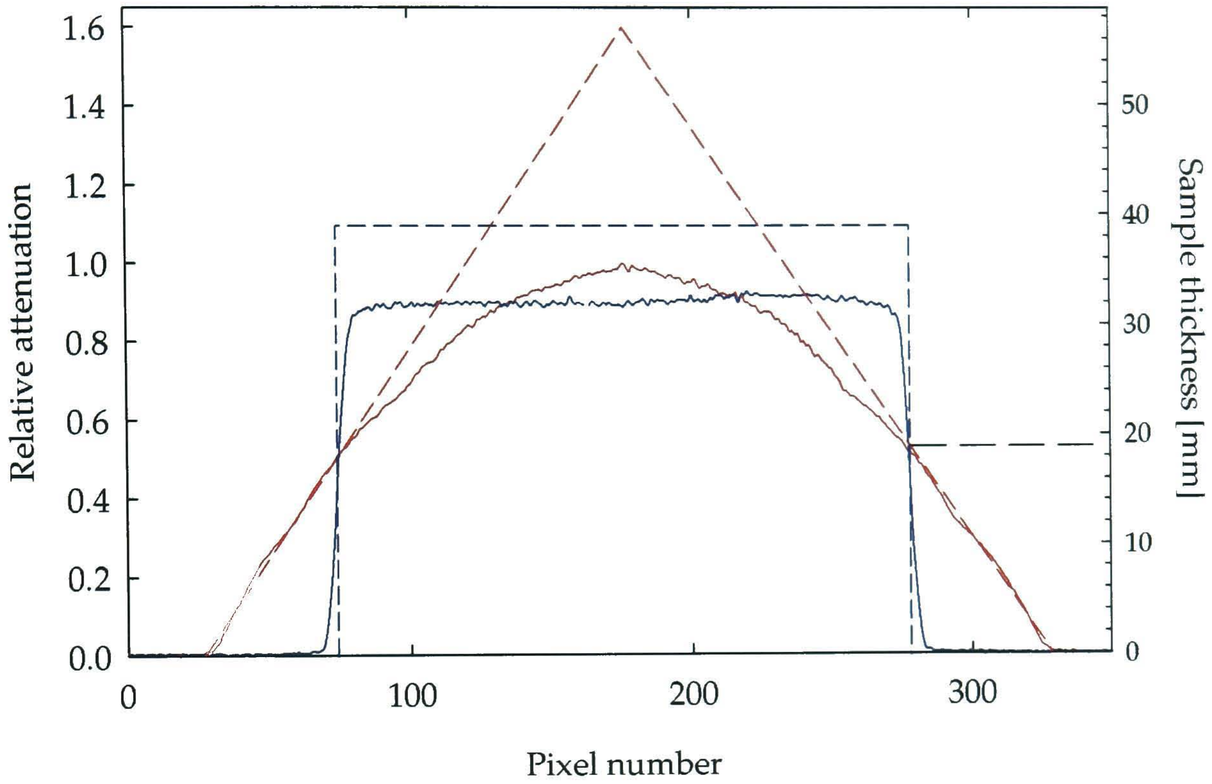

Figure 4.11: *A plot showing the attenuation profile of the graptolite sample when the shortest dimension (blue solid line) and the longest dimension (red solid line) is parallel to the beam propagation direction. Theoretical predictions of the attenuation profile, assuming a homogeneous and regular sample, are given by the corresponding dashed lines.*

4.5.3 Partial-volume effects

The finite resolution of imaging data will always produce blurring at material edges, where pixels and, subsequently, voxels will represent some average of the attenuation properties of the materials present across the boundary. Although blurring is normally undesirable, it can prove useful because even features much smaller than the voxel resolution will contribute to the overall value of a voxel. In some cases, this allows the inference of the presence of sub-voxel details.

4.5.4 Streaking

A highly attenuating feature will often have streaks protruding from it in reconstructed slices, resulting in obscured information both within that feature and in the immediate vicinity (Figure 4.12). This is especially noticeable if the region is angular (in which case streaks project from the corners), if the region is surrounded by a relatively weakly attenuating region (i.e. there is a high contrast edge), or if there are several such features in the same slice (in which case the streaks connect these features).

4.6 Quantifying attenuation coefficients

Accurately and precisely relating image grey-scale values to material linear attenuation coefficients requires ideal attenuation (i.e. no scattering, radiation is either transmitted or absorbed) of a monochromatic beam. (Knowledge of the detector pixel size is also required as this serves to provide information on the sample dimensions (the linear attenuation coefficient is expressed in units of cm^{-1})). The reason for the first restriction is that scattering causes a background signal, which skews the measured beam intensity (Section 4.4). The second stipulation arises because beam attenuation is dependent on the radiation energy (Section 2.3) and because beam hardening of a

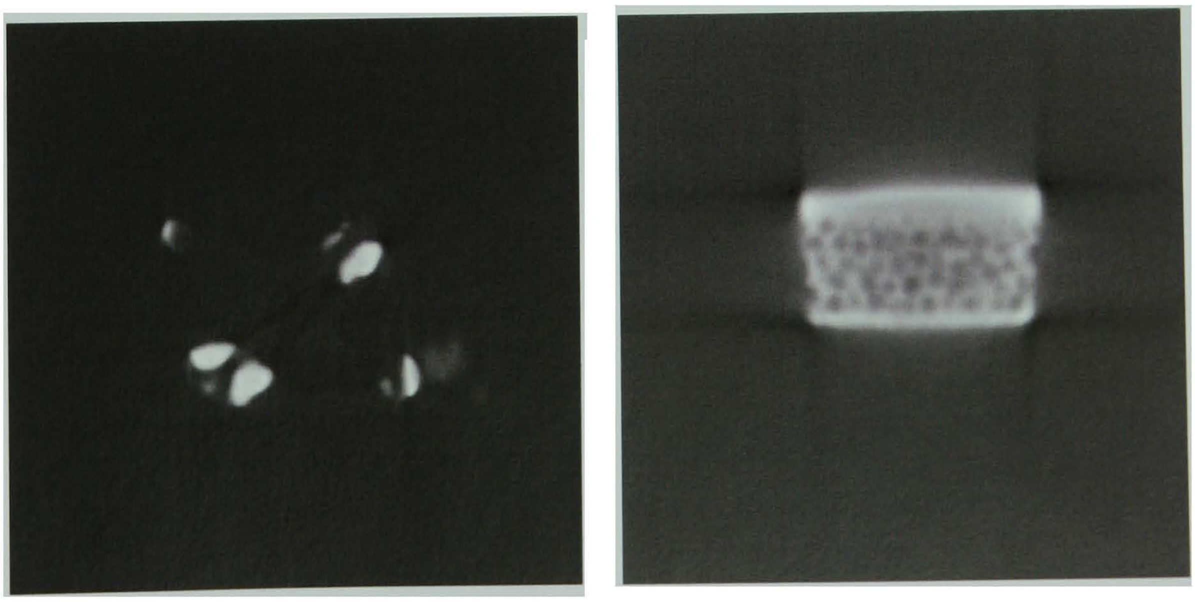

Figure 4.12: *Reconstructed slices showing streaks produced by highly attenuating features: pieces of a rubberised adhesive used to secure a sample in position (left) and a piece of aerated chocolate (right).*

polychromatic beam will cause the attenuation to be misrepresented (Section 4.5.2); both of these conditions are violated on *Neutrograph*.

Scattering represents the single most difficult obstacle to overcome in the retrieval of accurate neutron attenuation coefficients. It is possible to correct to some extent for scattering effects by modelling a scattering material as a system of scattering centres, each with an associated point scatter function [50]. This, however, requires an assumption of the shape of the scattering function, and knowledge of the location of the scattering centres. This becomes increasingly difficult as the complexity of the system increases, and in many cases it is only possible to compare approximately the relative magnitude of the attenuation coefficient of different regions of a sample.

5 Techniques

Standard radiography and tomography are already well-established diagnostic techniques, and their capabilities are continually being advanced by ongoing progress in instrumentation and refinements in experimental practices. Alongside these, a suite of supplementary techniques is also steadily being developed, offering flexibility in pushing the boundaries of what can be achieved in ever-growing and ever-diversifying fields of research.

5.1 2π-rotation tomography

Despite the previous assertion that tomographic imaging with a parallel beam only requires rotation about the sample of π (instead of 2π), since any projection, P_θ, will be an exact mirror image of the projection $P_{\theta+\pi}$ (Section 3.2.2), this is not quite true unless the beam divergence is very low. If the divergence is high, as is the case on *Neutrograph* (Section 3.2.3), then a rotation of just π produces a significant experimental asymmetry wherein some features of the sample will always be, on average, further away from the detection plane than others (Figure 5.1). Such features appear more blurred in projection data and, therefore, in reconstructed slices, and the attainable spatial resolution is thus diminished. Nevertheless, π-rotation tomography has been accepted as the convention on every world-leading neutron imaging beamline, *Neutrograph* included. However, at least as far as *Neutrograph* is concerned, the reasoning against 2π-rotation tomography – that it doubles both experiment times and data volumes with no tangible return – is erroneous.

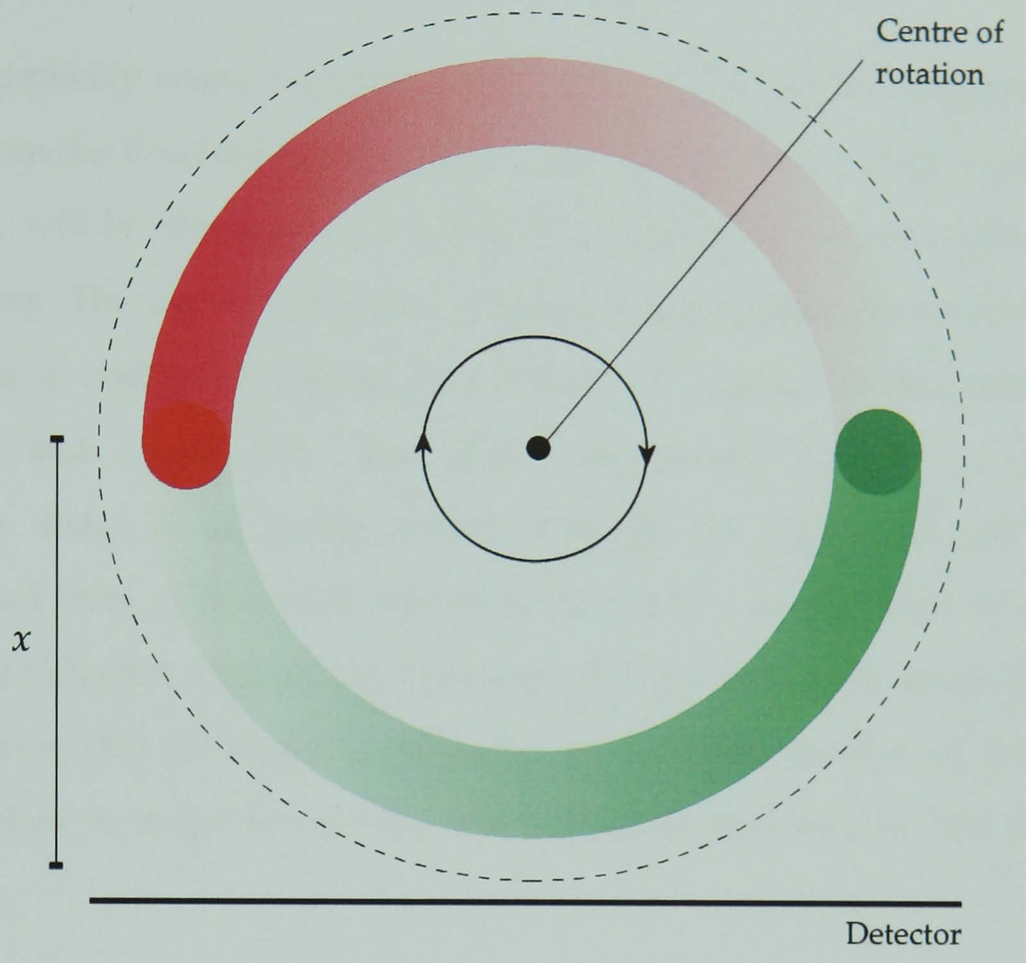

Figure 5.1: *A diagram illustrating the asymmetry of π-rotation tomography. The red feature will never be closer than x to the detection plane, while the green feature will never be further away than x. Consequently, the red feature will appear more blurred.*

Rather than acquiring a π-rotation tomography dataset, ψ, consisting of n projections, P_θ, in steps of θ (n is odd) such that

$$\psi = \{P_0, P_\theta, P_{2\theta}, \ldots\ldots, P_{\pi-2\theta}, P_{\pi-\theta}, P_\pi\} \qquad \text{Equation 5.1}$$

the data can instead be collected as a 2π-rotation tomography dataset, ψ', consisting of $n \pm 1$ (where n must be even) projections in steps of 2θ such that

$$\psi' = \{P_0, P_{2\theta}, \ldots\ldots, P_{\pi-\theta}, P_{\pi+\theta}, P_{\pi+3\theta}, \ldots \\ \ldots, P_{2\pi-2\theta}, P_{2\pi}\} \qquad \text{Equation 5.2}$$

The datasets ψ and ψ' are exactly the same size and (neglecting the very small difference in the times required to rotate the sample) can be acquired in the same length of time. Given that when one projection is mirrored horizontally

$$P_\theta \equiv P_{\pi+\theta},\ P_{3\theta} \equiv P_{\pi+3\theta}, \ldots$$
$$\ldots, P_{\pi-2\theta} \equiv P_{2\pi-2\theta},\ P_\pi \equiv P_{0,\,2\pi} \qquad \text{Equation 5.3}$$

they also explicitly contain the same data, but with one subtle difference: in ψ' the distance from the detection plane of every part of the sample, when averaged over all projections, will be identical. As a result all points in the reconstructed slice will be equally sharp. This can be confirmed by comparing the slices reconstructed from two sets of data ψ and ψ', collected for a bundle of tubular drinking straws (*Ø5 mm*) (Table 5.1 and Figure 5.2). The slice reconstructed from ψ' is, as surmised, consistently sharp at all points, while, although the right-hand side of the slice reconstructed from ψ is as well-defined as that of ψ', the left-hand side is visibly, if subtly, more blurred (Figure 5.3). That the left-hand side is the more distorted is as expected given that the image is orientated to the initial position of the sample, the detection plane is at the lower edge and rotation is clockwise (cf. the red feature in Figure 5.1).

Camera	PCO SensiCam
Lens	50 mm
Camera box *[cm]*	100
Rotation angle	π / 2π
Projections	801 / 800
Exposure per projection *[s]*	5 [100×50 ms]

Table 5.1: *Experimental parameters used to compare π- and 2π-rotation tomography.*

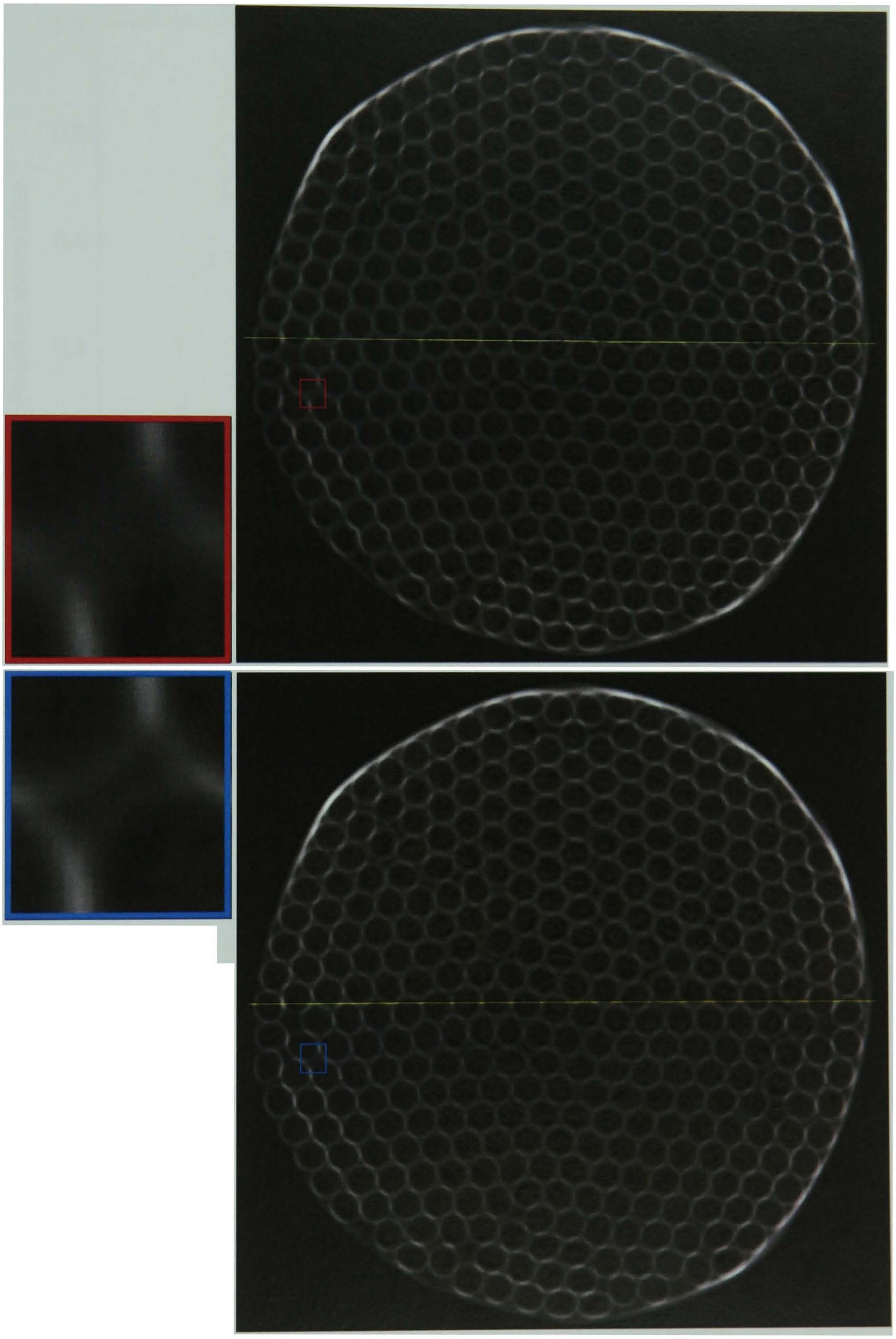

Figure 5.2: *Slices of a bundle of drinking straws (Ø5 mm) reconstructed from 801 projections taken π (top) and 800 projections taken 2π (bottom) around the sample.*

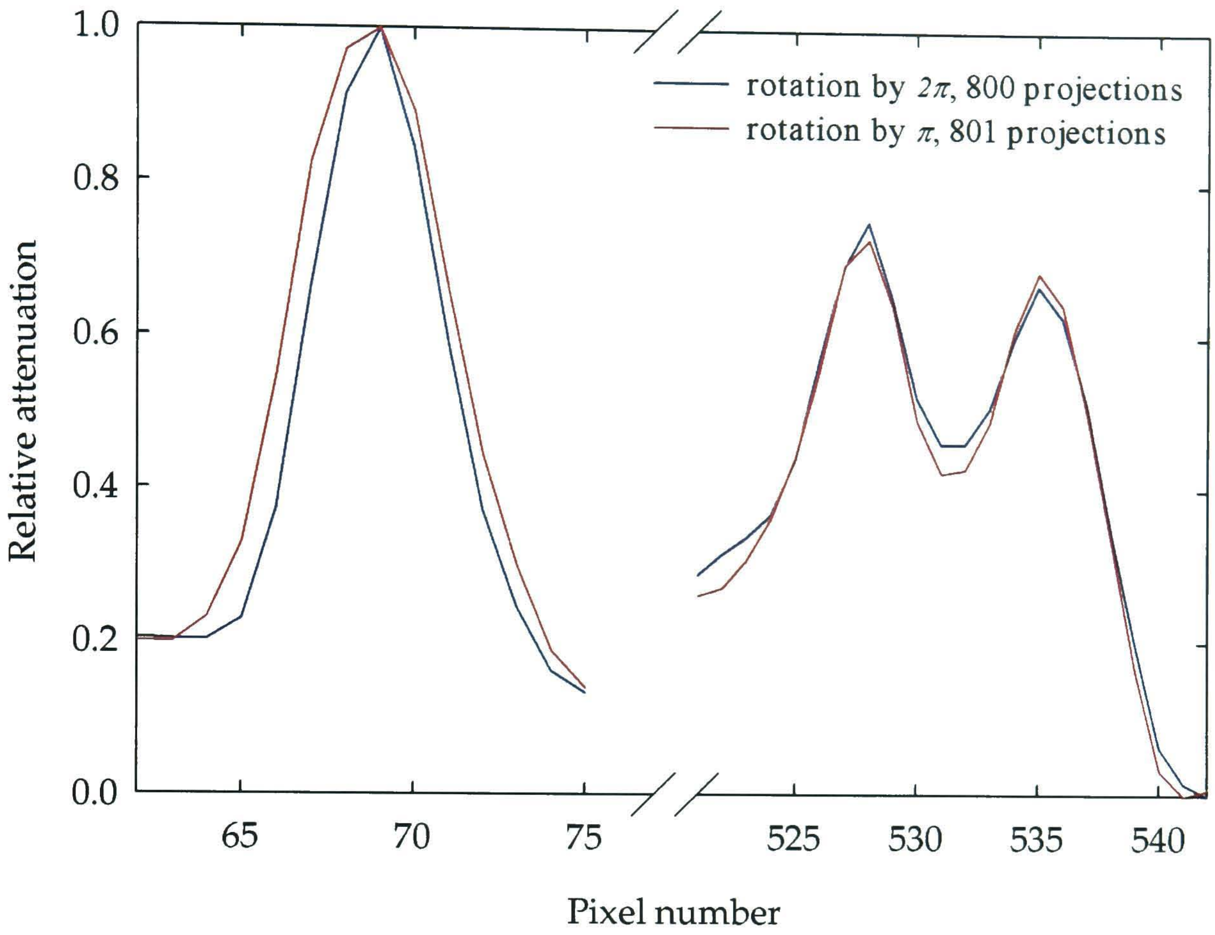

Figure 5.3: *A plot of the intensity profiles along the left and right extremes of the yellow lines in* Figure 5.2.

5.2 Rapid dynamic tomography

If a system changes on a time-scale longer than the time required for radiography (the sum of the exposure time and readout time) then it is possible to visualise the dynamics in two dimensions by taking a series of radiographic images. In the same way, if the process is much slower than the time, T_{tomo}, taken to obtain a set of tomography projections then there is the potential to study the time evolution of a three-dimensional system.

There are two possible modes of data acquisition: interrupted, where the sample is rotated stepwise to and imaged at a series of predefined positions; and uninterrupted, where the sample is rotated continuously and imaged at a predefined frequency while the sample is motion. The advantage of the latter is that it is faster because imaging and rotation are carried out simultaneously and there is no need for the continual and (relatively) time-consuming acceleration and deceleration of the rotation motor. However, this is counterbalanced by the disadvantage of every projection being subject to motion blur; during exposure time, t, any given feature will move a distance, β, related to the frequency of rotation, ν, and the distance of the feature from the axis of rotation, r, according to $\beta = 2\pi r \nu t$.

A combination of three factors affect the length of T_{tomo}: the projection acquisition time, the image readout rate, and the time taken to rotate the sample. As already discussed, rapid acquisition requires a high flux (Section 4.3), making *Neutrograph* ideal for such experiments; image acquisition times can be as short as *1 ms*. The limiting step will either be the camera's frame rate, *33 Hz* at *1 ms* exposure (although this decreases with increasing exposure time), or the speed of the rotation table, *7.2 s* for uninterrupted π-rotation [51] (for interrupted rotation this depends on the number of steps and the exposure time). The current physical limit for uninterrupted tomography on *Neutrograph* is *1 ms* exposure at *33 Hz* and *7.2 s* rotation → *237* projections per tomography (Table 5.2), but this could be improved upon with faster hardware.

Interrupted dynamic tomography has been used to observe spontaneous imbibition, the displacement of one fluid by the absorption of another (immiscible) fluid in porous media. The morphology and velocity with which an imbibition front progresses is governed by an interplay between the surface tension at the fluid interface (capillary action) and the viscosity of the fluids (drag forces) and is thus sensitive to the permeability and structure of the medium.

Two dry, red-sandstone rock cores (*Ø35×49 mm* and *Ø35×35 mm*) (Figure 5.4) were imaged as they imbibed deionised water from a Petri-dish reservoir at an average rate of ~$5\ mm{\cdot}hr^{-1}$ (experimental parameters given in Table 5.3). This equates to the front advancing ~*220 μm* in time T_{tomo}, *160 s*, producing only minute, imperceptible blur-artifacts in the reconstructed slices. The sandstone had relatively large pores, in the range ~*100 μm*, and a porosity of around *24%*, but was also criss-crossed by multiple fault zones, quartz cement, which had a much smaller pore size, in the range ~*0.1 μm*,

Projection exposure time *[ms]*	Camera frame rate *[Hz]*	Possible number of projections in *7.2 s*	Time required for 181 projections *[s]*
1	33.0	237	5.5 *
2	31.3	225	5.8 *
3	30.3	218	6.0 *
4	29.4	212	6.2 *
5	28.6	206	6.3 *
10	25.0	180	7.2
20	20.0	144	9.1
25	18.2	131	10.0
50	12.5	90	14.5
75	9.5	69	19.0
100	7.7	55	23.5
150	5.6	40	32.6
200	4.3	31	41.6
250	3.6	26	50.7
500	1.9	14	95.9
750	1.3	9	141.2
1000	1.0	7	186.4

Table 5.2: *Neutrograph's current hardware limitations for the time taken to acquire an uninterrupted π-rotation tomography dataset, assuming one exposure per projection using the CCD camera's maximum field of view. Entries marked * are beyond the speed of the rotation table; all other entries are limited by the frame rate of the camera.*

and a porosity of around *10%*. Although the unfaulted sandstone in direct contact with the reservoir fills with water very quickly (red regions in Figure 5.5), the fact that capillary pressure is inversely proportional to the capillary diameter (the pore size) means that, thereafter, the water flows preferentially through the faults (Figures 5.5-5.7).

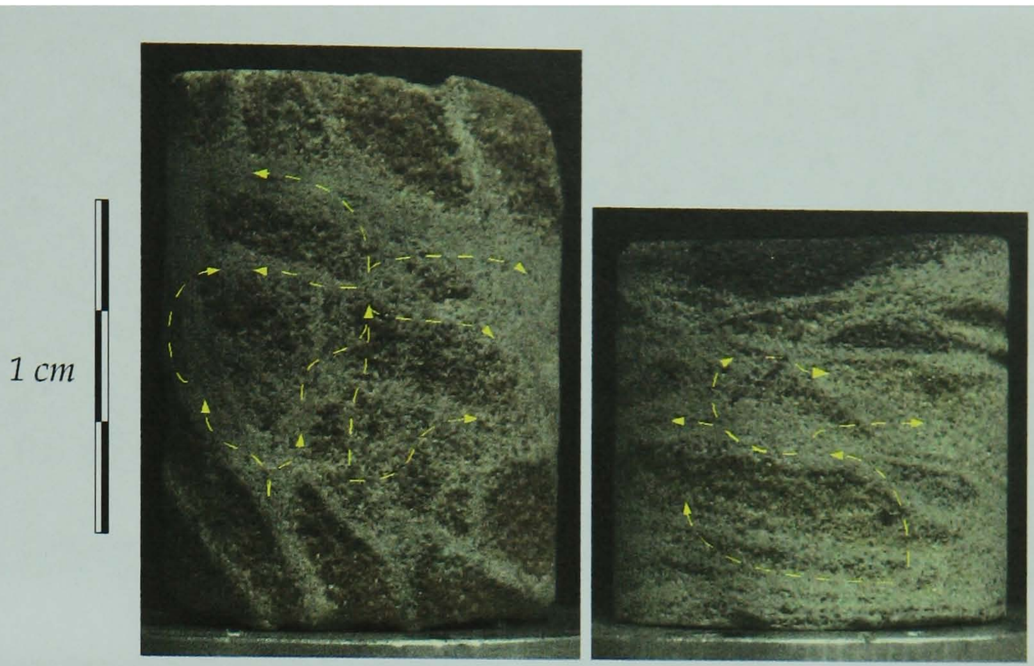

Figure 5.4: *Photograph of the two red-sandstone cores used to visualise imbibition processes. The yellow arrows indicate the approximate imbibition flow paths through the fault zones (lighter areas).*

Camera	Andor iXon
Lens	85 mm
Camera box *[cm]*	100
Rotation angle	π
Projections	181
Exposure per projection *[s]*	0.5 [10×50 ms]

Table 5.3: *Experimental parameters used for a dynamic tomographic study of imbibition.*

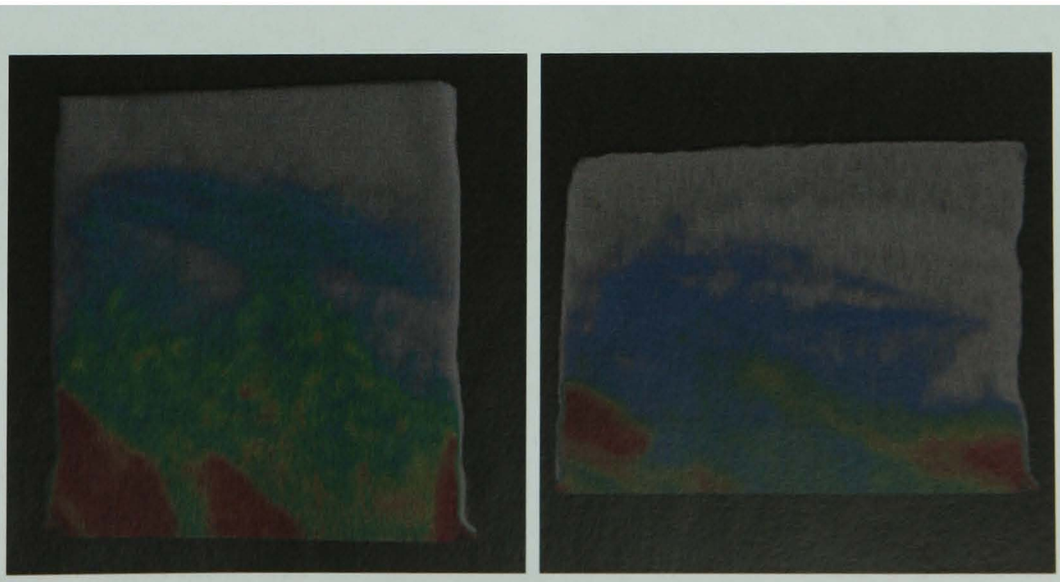

Figure 5.5: *Vertical cross-sections through the centre of the cores after three hours of imbibition (same orientation as in* Figure 5.4*). The reddest areas are wettest; white areas are still dry.*

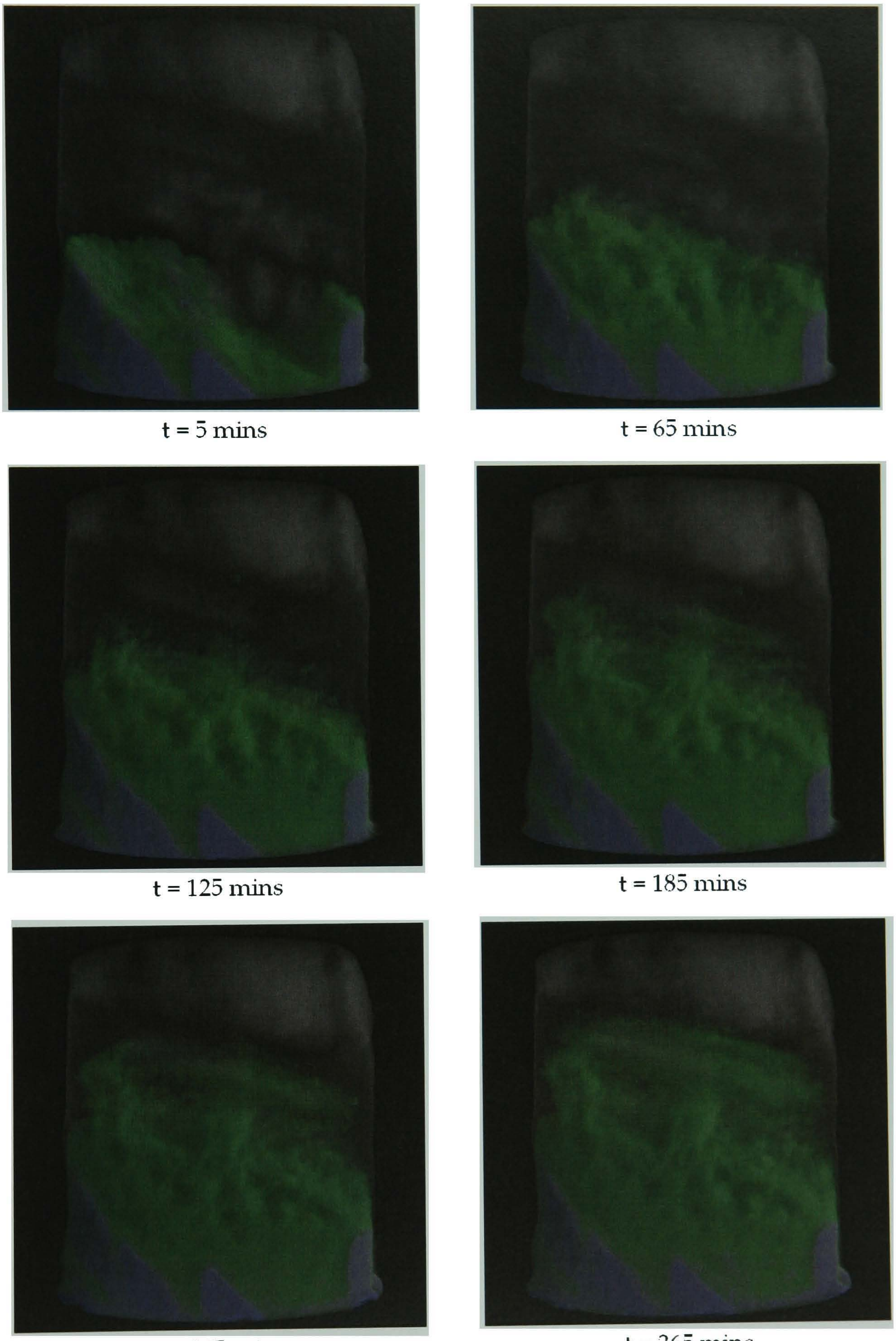

t = 5 mins

t = 65 mins

t = 125 mins

t = 185 mins

t = 245 mins

t = 365 mins

Figure 5.6: *A reconstruction of imbibition in the tall sandstone core. Purple areas are sandstone pockets in direct contact with the reservoir; green areas show the movement of the imbibition front. White areas are included to indicate the outline of the core.*

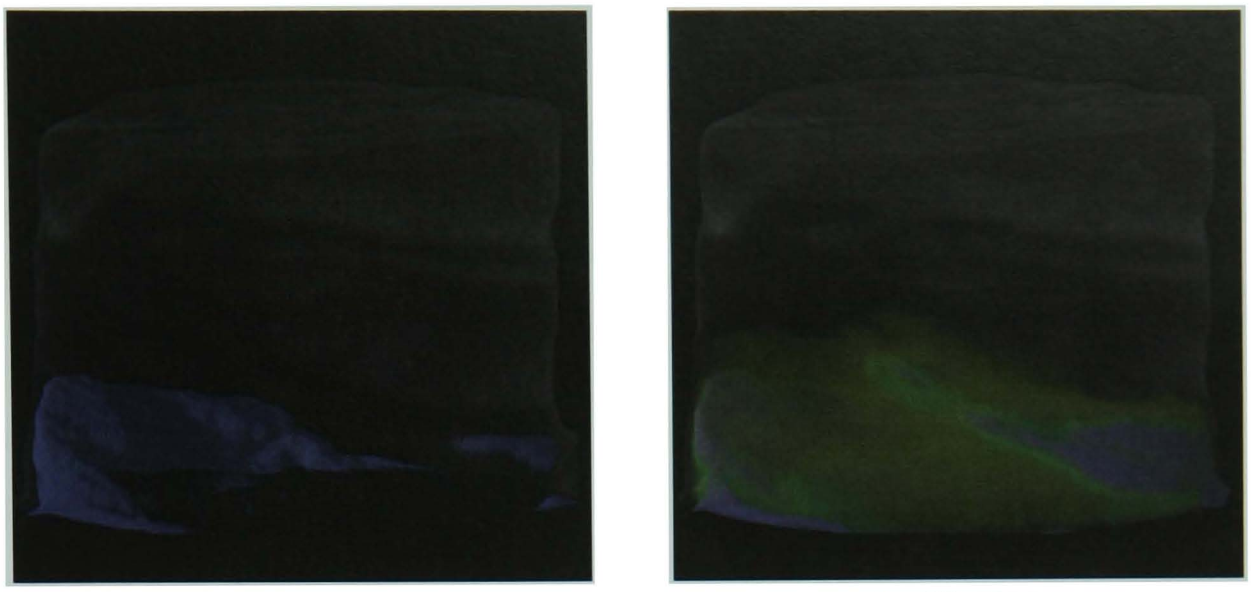

t = 5 mins

t = 35 mins

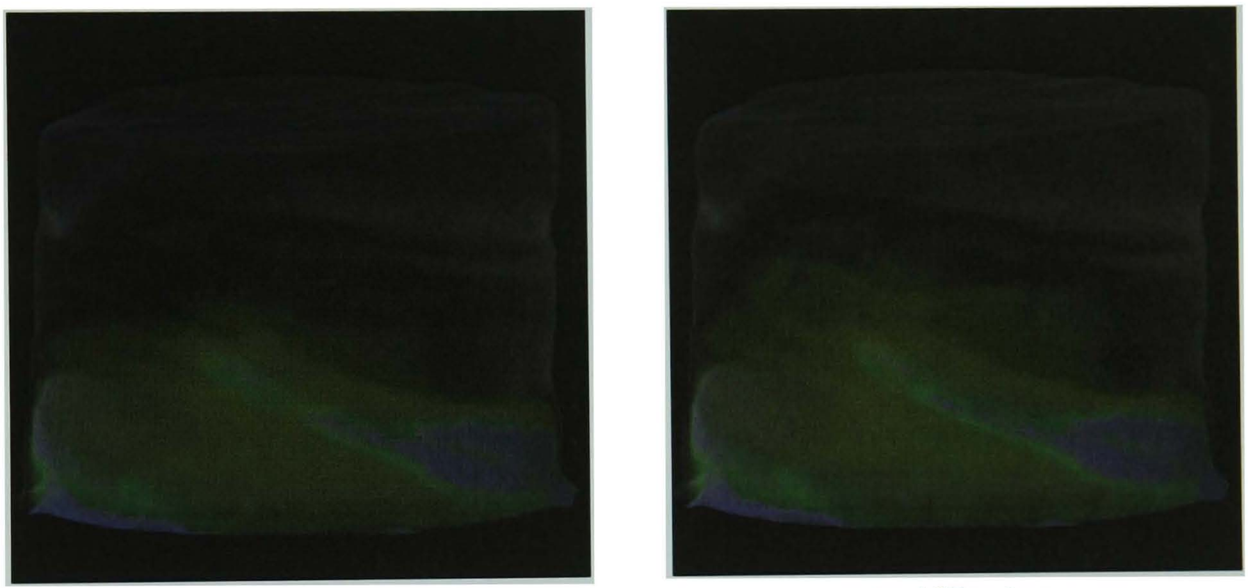

t = 65 mins

t = 185 mins

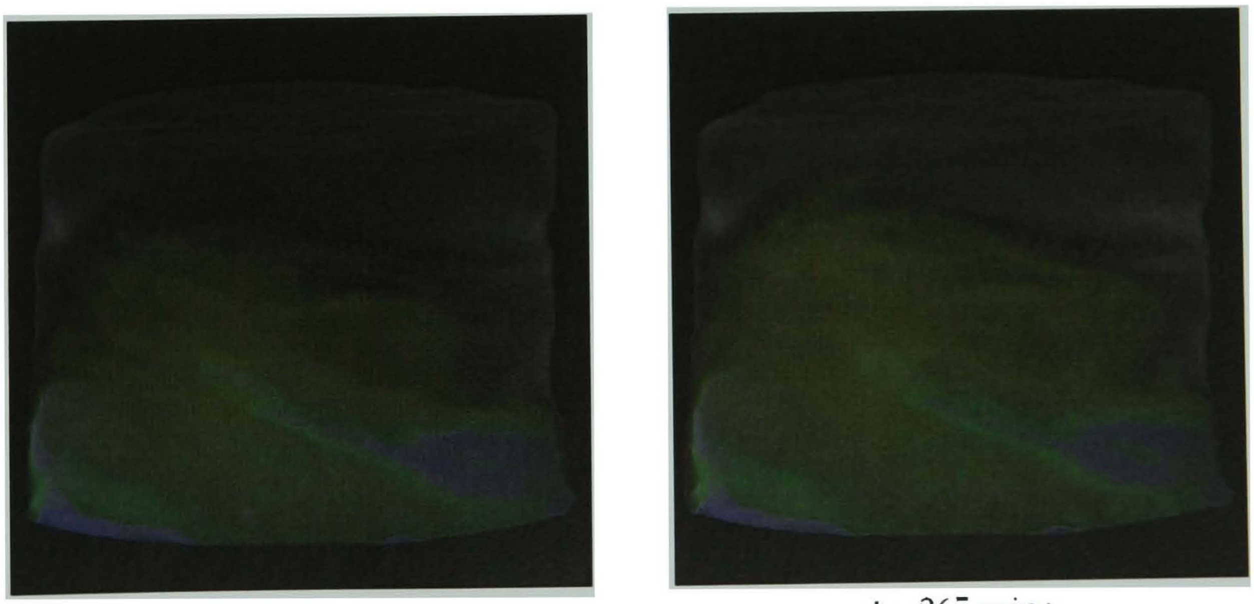

t = 245 mins

t = 365 mins

Figure 5.7: *A reconstruction of imbibition in the short sandstone core. Purple areas are sandstone pockets in direct contact with the reservoir; green and orange areas show the movement of the imbibition front. White areas are included to indicate the outline of the core.*

5.3 Imaging magnetic materials

Variation in neutron absorption (attenuation) is not the only measurable signal that is usable for imaging applications. Neutrons have a permanent magnetic dipole moment, $\vec{\mu}$ ($\mu = -9.66\times10^{-27}\ J\cdot T^{-1}$), which makes them sensitive to the atomic-scale magnetic fields produced by unpaired orbital electrons and unpaired nucleons in nuclei through an interaction whose strength is often comparable to that of the neutron-nucleus interaction. Consequently, neutrons can be used to probe the magnetic structures and properties of bulk materials [52, 53] (recall that charge neutrality means that neutrons can penetrate deeply into matter), assuming that the magnetic effects can somehow be separated from the nuclear effects (attenuation, for example).

The existence of a dipole moment and its direction are determined by the spin (quantum-mechanical, internal angular momentum) of the neutron, $\vec{S}$, which has a quantum number ½; the minus in front of the magnitude of the moment given above indicates that the moment is always oriented anti-parallel to the spin axis. (Studying the interactions of the spin is thus equivalent to studying the interactions of the magnetic moment). Under the influence of an external magnetic field, $\vec{B}$, the time-dependent behaviour of the spin orientation can be completely described by the wave equation [52]

$$\frac{\mathrm{d}}{\mathrm{d}t}\vec{S} = \gamma_L\left[\vec{S}(t)\times\vec{B}(t)\right] \qquad \text{Equation 5.4}$$

where γ_L is the gyromagnetic ratio of the neutron ($-1.832\times10^{-8}\ rad\cdot s^{-1}\cdot T^{-1}$). The presence of an applied field has two important consequences (Figure 5.8). Firstly, within the field the Zeeman effect will cause the neutrons to split into two energy levels

$$E = E_0 \pm \tfrac{1}{2}\mu B \qquad \text{Equation 5.5}$$

Consequently, there are only two possible neutron spin orientations: parallel, ↑ (+,

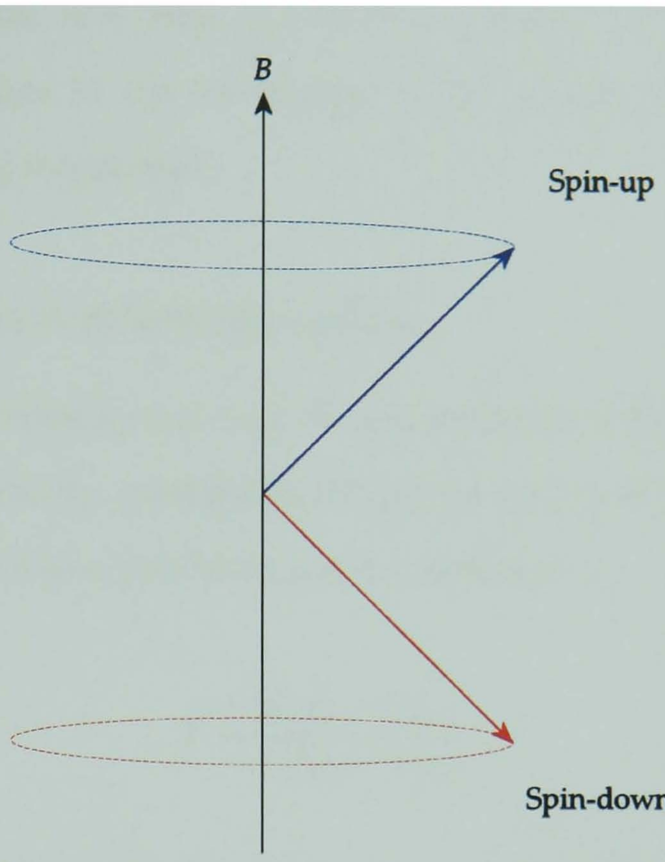

Figure 5.8: *A diagram showing neutron spins precessing around a quantisation axis defined by an applied magnetic field,* $\vec{B}$.

spin-up), or anti-parallel, ↓ (–, spin-down), i.e. the applied field acts as a quantisation axis. Secondly, the field exerts a torque on the spin axis, causing it to undergo Larmor precession around the field with a frequency given by

$$\omega_L = \gamma_L B \qquad \text{Equation 5.6}$$

where B is the magnitude of the magnetic field. For a neutron travelling along a path, s, with a velocity, v, the total precession angle is

$$\Delta \vartheta = \omega_L \frac{\mathrm{d}s}{v} \qquad \text{Equation 5.7}$$

which can be expressed in terms of the neutron wavelength, λ, as

$$\Delta \vartheta = \frac{\gamma_L \lambda m}{h} \int B \, \mathrm{d}s \qquad \text{Equation 5.8}$$

where m is the neutron rest mass (1.675×10^{-27} kg) and h is the Planck constant (6.626×10^{-34} $J\cdot s^{-1}$). Changes in the orientation of the neutron spin will therefore be indicative of underlying magnetism.

5.3.1 Principles of polarisation analysis

An analysis of the spin rotation can only be accomplished if the neutron beam is first polarised, i.e. if the majority (preferably all) of the neutrons are in one of the two possible spin states. The scalar polarisation is quantified as

$$P = \frac{N(\uparrow) - N(\downarrow)}{N(\uparrow) + N(\downarrow)} \qquad \text{Equation 5.9}$$

where $N(\uparrow)$ is the number of neutrons in the spin-up state and $N(\downarrow)$ is the number of neutrons in the spin-down state. $P = 1$ describes a beam polarised perfectly in the up direction, $P = -1$ describes a beam polarised perfectly in the down direction, and $P = 0$ describes an unpolarised beam (one in which the two spin-states are equally populated). This can be expressed in vector form as the average over all neutron spins normalised to the modulus

$$\vec{P} = \frac{\langle\vec{S}\rangle}{½} = 2\,\langle\vec{S}\rangle \qquad \text{Equation 5.10}$$

Thus, rather than considering the interactions of each neutron spin with a magnetic field, it is possible to consider the changes in the polarisation that result from these interactions, and Equation 5.4 can be rewritten accordingly as

$$\frac{\mathrm{d}}{\mathrm{d}t}\vec{P} = \gamma_L\left[\vec{P}(t)\times\vec{B}(t)\right] \qquad \text{Equation 5.11}$$

As a polarised neutron beam passes through a magnetic field the polarisation axis will therefore precess (Figure 5.9). If the field component perpendicular to the polarisation axis is negligible, then the polarisation will be preserved. If, however, the field

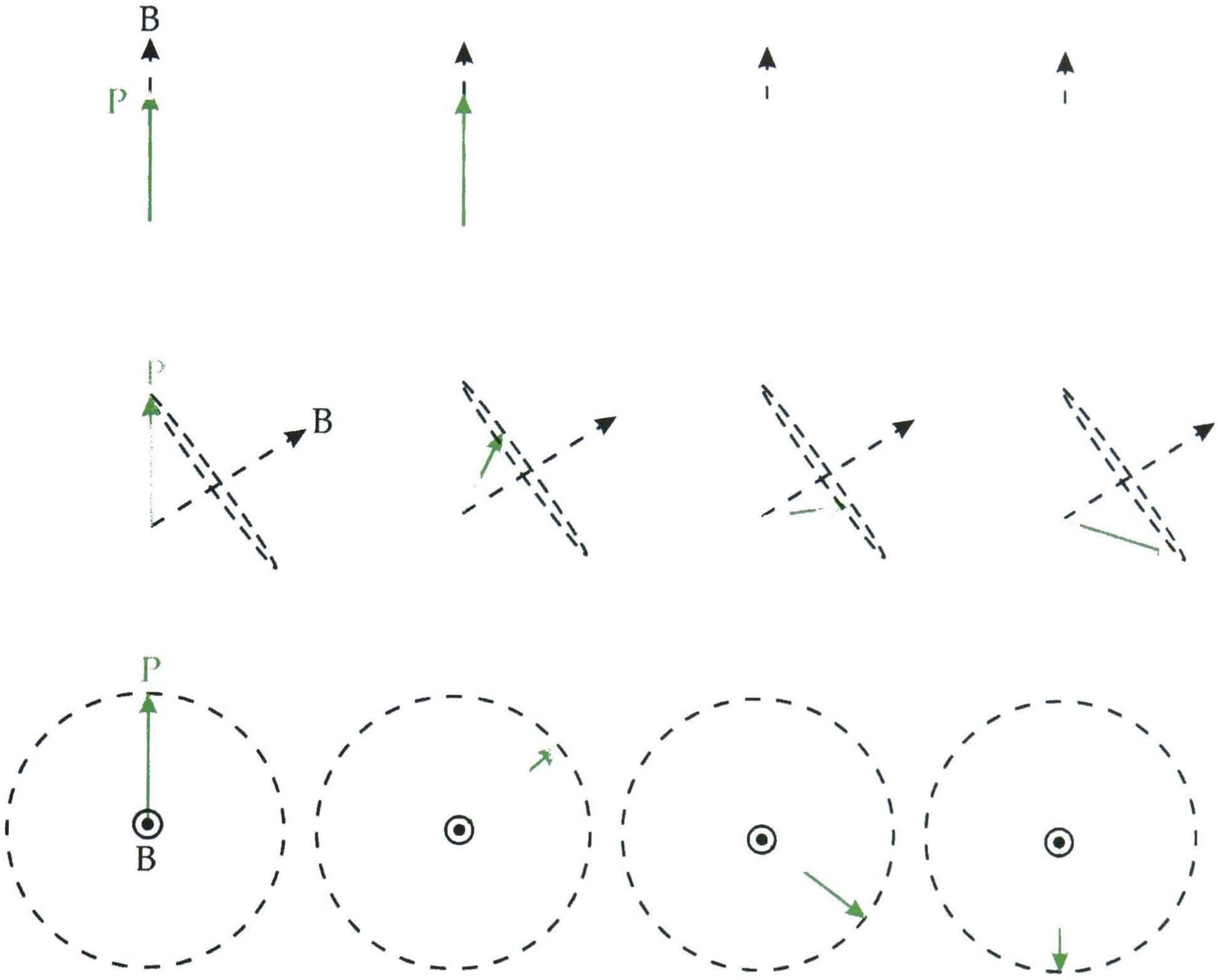

Figure 5.9: *The orientation of the polarisation axis will be preserved if it is parallel to an applied magnetic field (top), but will flip if there is a significant perpendicular magnetic field component.*

component perpendicular to the polarisation axis is significant, then the polarisation axis will rotate, beating between up and down; in relation to the initial polarisation axis, the beam will depolarise.

The changes in the polarisation can be described by

$$\vec{P}_1 = D\,\vec{P}_0 \qquad \text{Equation 5.12}$$

where $\vec{P}_1$ and $\vec{P}_0$ are the final and initial polarisation, and D is a 3×3 depolarisation matrix. The elements of the depolarisation matrix can be determined by measuring the polarisation in three mutually orthogonal directions, which can be achieved using the experimental set-up shown in Figure 5.10. It consists of two polarisers, one to polarise the beam and one to analyse the beam (the polariser and analyser are usually aligned

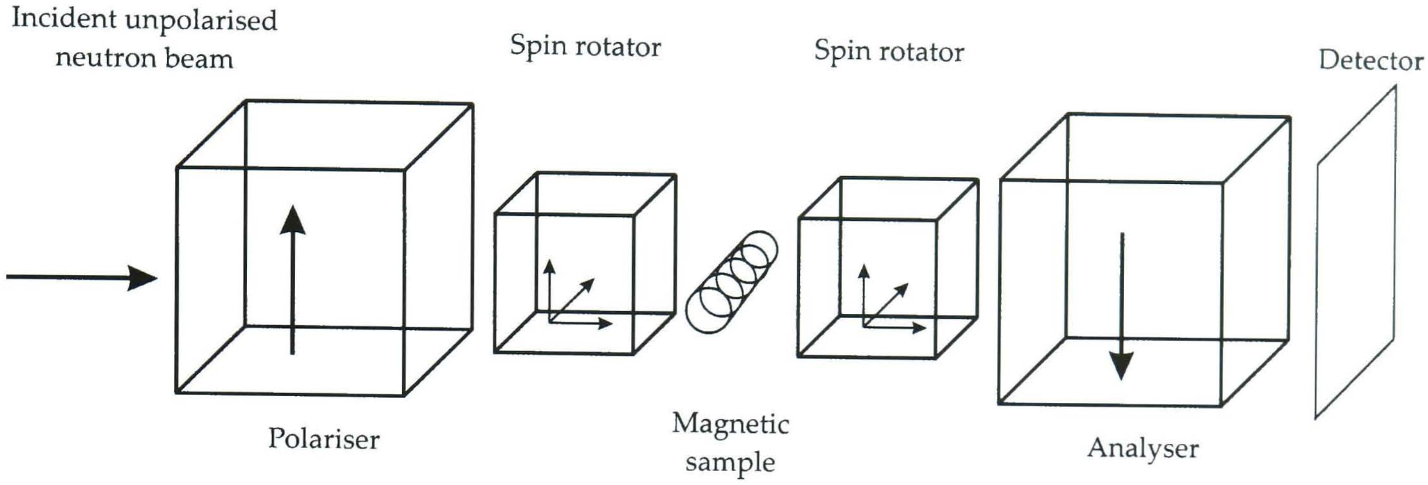

Figure 5.10: *A typical experimental set-up used to analyse a polarised neutron beam. The spin rotators allow the polarisation and analysis axis to be orientated arbitrarily relative to the sample.*

anti-parallel), and two spin rotators, which allow the beam polarisation to be rotated arbitrarily into any direction relative to the sample. The analyser will only transmit the component of the polarisation that is parallel to its own polarisation and this is represented in the intensity measured in the detection plane. The depolarisation is then given by

$$D = D_{ij} = 1 - \frac{I_{ij}}{I_s} \qquad \text{Equation 5.13}$$

where i indicates the axis of polarisation, j indicates the axis of analysis, $I_{i,j}$ is the intensity measured behind the analyser, and I_s is the intensity incident on the sample [54, 55]. The depolarisation matrix is directly related to the magnetic structure of the sample, but, even given all elements, it is very difficult to reconstruct the latter from the former. The difficulties lie in the fact that, although a given magnetic field distribution will always be described by the same depolarisation matrix, the reverse is not true; any number of other field distributions could produce an identical matrix. Some success can be achieved through reverse approaches based on information about the magnetic structure that is well-known (a simple dipole magnet) or calculable [56] (for example, by the Biot-Savart Law), but, despite efforts in this field [57-60], there is currently no way to solve this problem analytically.

Polarisation analysis with a polychromatic neutron beam carries a further complication because the total angle of precession (although not the rate of precession) is proportional to the neutron wavelength (Equation 5.7). Consequently, precession will cause a polychromatic neutron beam to dephase (the polarisation axes for neutrons of different wavelengths will shift relative to one another), resulting in a loss of polarisation (Figure 5.11) in the plane perpendicular to the field direction. An ideal monochromatic beam will not dephase in this way, but since a practical monochromatic beam typically has a 1-2% wavelength spread $(\Delta\lambda/\lambda)$, given enough precessions (i.e. a strong enough magnetic field) it too will dephase and depolarise.

5.3.2 Principles of helium-3 spin-filters

Several techniques exist for polarising neutron beams including preferential reflection from magnetic mirrors or supermirrors [61-63], and preferential diffraction from magnetic materials (such as Heusler crystals) [64, 65]. However, the method selected for polarised neutron studies on *Neutrograph* utilised helium-3 spin-filters, since this approach is relatively simple to set up, and the Institut Laue-Langevin has a well-equipped group that specialises in building and developing helium-3 spin-filter technology.

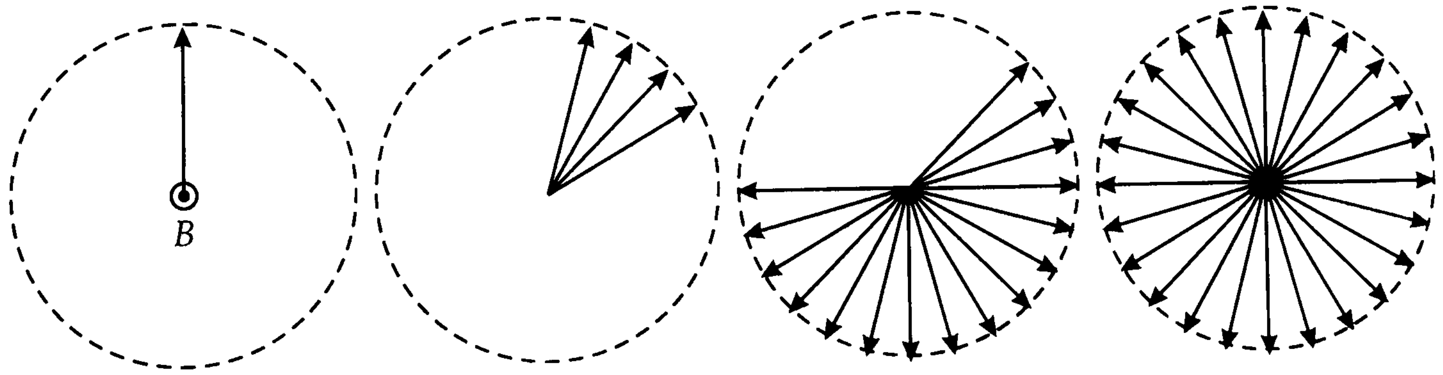

Figure 5.11: *Precession will cause a polychromatic neutron beam to dephase and depolarise in the plane perpendicular to the field direction. The arrows indicate the vector polarisation for neutrons of different wavelengths, with time increasing from left to right.*

The underlying principle of helium-3 spin-filters is that helium-3 has a highly spin-dependent neutron capture cross-section, strongly absorbing those neutrons with the spin-state that is opposite to that of the helium-3 nucleus (thermal neutrons: $\sigma\{\mathrm{He}(\uparrow)n(\downarrow)\}$=*6000 barn*, $\sigma\{\mathrm{He}(\uparrow)n(\uparrow)\}$=3 *barn*, the scattering cross-section is negligible)

$$^{3}\mathrm{He}\binom{\uparrow}{\downarrow} + n\binom{\downarrow}{\uparrow} \rightarrow {}^{4}\mathrm{He}^{*} \rightarrow {}^{3}\mathrm{H} + p + 740\ keV \qquad \text{Equation 5.14}$$

A sufficiently high column density of perfectly polarised helium-3 would thus remove all (and almost only) anti-parallel neutrons, leaving the emergent beam polarised parallel to the filter. In practice, the helium-3 polarisation will not be perfect, necessitating a compromise between the polarisation and the transmission of the neutron beam (a sufficiently high column density of imperfectly polarised helium-3 would be completely opaque, removing all neutrons from the beam). In general, the transmission of neutrons through a polarised helium-3 cell is given by

$$T\binom{\uparrow}{\downarrow} = \mathrm{e}^{-(1 \mp P\{\mathrm{He}\}) \cdot N\{\mathrm{He}\} \cdot \sigma \cdot l} \qquad \text{Equation 5.15}$$

where $\uparrow$ ($\downarrow$) signifies the component with the neutron spin parallel (anti-parallel) to the helium-3 nuclear spin, $P\{\mathrm{He}\}$ is the polarisation of the helium-3, $N\{\mathrm{He}\}$ is the number density of helium-3 nuclei in the filter, σ is the absorption cross-section for unpolarised neutrons, and l is the length of the filter [66].

The advantageous properties of helium-3 spin-filters are that the resulting polarisation is roughly homogeneous over the whole beam; they are based solely on simple transmission, which means that the angular distribution of the beam is unperturbed and neutrons over a large solid angle will be accepted (even a poorly-collimated beam can be polarised effectively without excessive intensity losses); and they are effective across a relatively broad energy spectrum, which can be manipulated and optimised by adjusting the pressure of the helium (recall that the interaction cross-section, σ, in Equation 5.14 is energy-dependent).

5.3.3 Polarisation of helium-3

At the Institut Laue-Langevin, the *Tyrex* filling station [67, 68] is used to polarise helium-3 gas at a pressure of *~1 mbar* via metastability-exchange optical pumping (MEOP) [69, 70]. In this method a radio frequency plasma discharge is used to excite a small number of helium-3 atoms from the electronic ground-state, 1^1S_0, to the metastable 2^3S_1 state. Optical pumping with circularly polarised light from an infra-red ytterbium-fibre laser (*1083 nm*) promotes $2^3S_1 \rightarrow 2^3P_0$ transitions for a single spin-state, producing an electronic polarisation that is rapidly transferred to the nucleus via the hyperfine interaction and then to a ground-state helium-3 nucleus via exchange collisions. The polarised gas is then compressed by a hydraulic titanium-alloy piston to a pressure of several *bar* and drawn off into a valve-sealed cell (currently GE180 aluminosilicate glass, GE224 quartz glass, or Pyrex glass with single-crystal silicon windows). *Tyrex* is currently capable of providing around $1.3\ bar{\cdot}l{\cdot}hr^{-1}$ of helium-3 with a polarisation of *~75-80%*.

Polarised helium-3 nuclei will rapidly relax under normal conditions as a result of dipole-dipole interactions, collisions with container walls, and interactions with stray magnetic fields (or field homogeneities or gradients). The first two effects are limited by low working pressures (at the cost of requiring longer cells), with the second effect being reduced further by coating the inner surfaces of the cells with a layer of caesium (this prevents gas diffusing into the glass, which is a dominant relaxation mechanism [71, 72]). The third effect requires that the helium-3 be confined to a uniform magnetic field. Throughout the polarisation process, this field is maintained by a system of nine electromagnetic coils (*Ø2 m*), which provide a cylindrical region (*Ø0.9×2.5 m*) with a field of *10 G* and a relative gradient ($1/B{\cdot}\mathrm{d}B/\mathrm{d}x$) of $\sim 10^{-4}$. Thereafter, both during transportation and while installed on an instrument, a cell is stored inside a specially designed magneto-static cavity (a "magic box") containing either μ-metal and an array of permanent ferromagnets, or an electromagnetic solenoid (a helium-3 spin-filter should thus be considered as a gas cell in conjunction with a magneto-static cavity). Using this combination of methods, the relaxation time for the helium-3 is typically upwards of *100 hr*.

5.3.4 Radiography with polarised neutrons

The initial testing of a polarised neutron imaging on *Neutrograph* was intended only as a feasibility study, using only uniaxial polarisation analysis to differentiate between magnetic and non-magnetic regions. The experimental arrangement consisted of two spin-filters (Figure 5.12) – one polariser and one analyser – each containing a

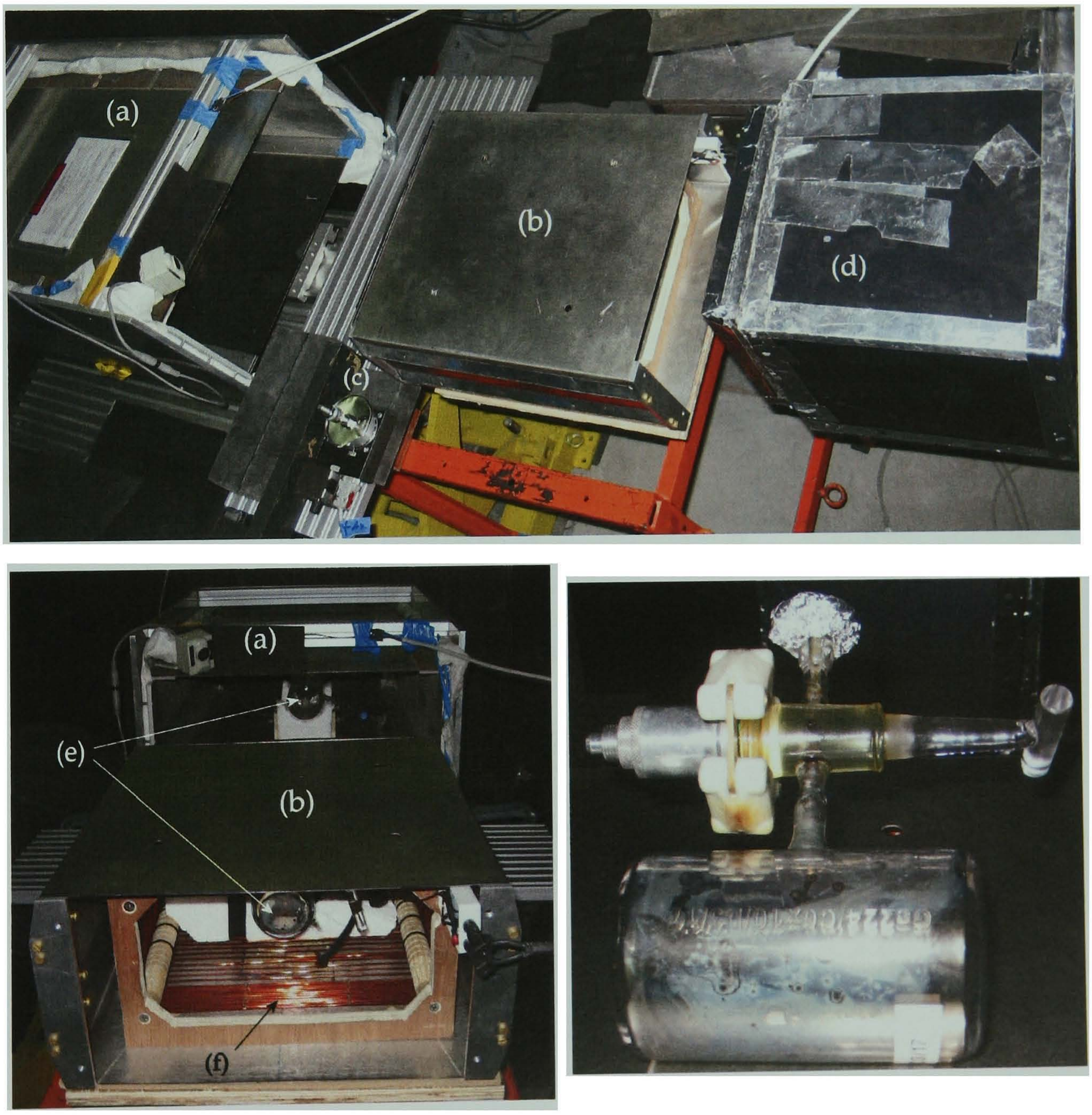

Figure 5.12: *Photographs of the experimental arrangement used for polarised neutron imaging from above (top) and looking back along the beam propagation direction (left), and of a helium-3 cell (right). The various pieces of equipment are (a) the magneto-static box used to hold the polarising helium-3 cell, (b) magneto-static box used to hold the analysing helium-3 cell, (c) the sample space, (d) the camera box, (e) the helium-3 cells, and (f) the radio frequency spin flipper.*

cylindrical, GE180 aluminosilicate glass cell (*Ø60×100 mm*) filled with helium-3 to a pressure of ~*2 mbar* (optimised for thermal neutrons, ~*1.5 Å*). Both filters were shielded with boron carbide screens that restricted the beam to the field of view of the helium-3 cell (~*Ø50 mm*, the side walls of the cells curved into the faces, making the usable field of view slightly smaller than the full diameter). This served both to limit radiation damage to and to reduce the contribution of neutrons scattering from the polarisation equipment. The analyser also had an integrated solenoid, which, by emitting a radio frequency pulse tuned to the Larmor frequency for helium-3 nuclei for the homogeneous field inside the magneto-static cavity, could be used to induce transitions between the helium-3 spin-states, and thus allow the polariser and analyser to be aligned parallel or anti-parallel. Flipping the polarisation of the spin-filter is equivalent (in terms of the transmission of the filter) to flipping the polarisation of the incident beam with an efficiency of *100%* regardless of the neutron wavelength (although, in practice, there is a loss in polarisation of ~10^{-5} for each flip).

Aligning the polariser and analyser parallel (anti-parallel) it is possible to form radiographic images using only the non-spin-flipped (spin-flipped) neutrons (Figure 5.13), which can then be normalised as per conventional radiography (Section 4.1) to the non-spin-flipped open beam. The intensity measured in these images is a superimposition of magnetic effects and attenuation, which give some effective attenuation. In the non-spin-flipped image any region that flips neutrons will appear more attenuating than usual (flipped neutrons will not be transmitted by the analyser), while in the spin-flipped image any region that does not flip neutrons will appear more attenuating than usual (non-flipped neutrons will not be transmitted by the analyser). The absorption attenuation will be approximately equal in both cases and its effect can be removed by taking the ratio of the two images

$$F = \frac{N(\uparrow)}{N(\downarrow)} \qquad \text{Equation 5.16}$$

where F is the flipping ratio, $N(\uparrow)$ is the non-spin-flipped image, and $N(\downarrow)$ is the

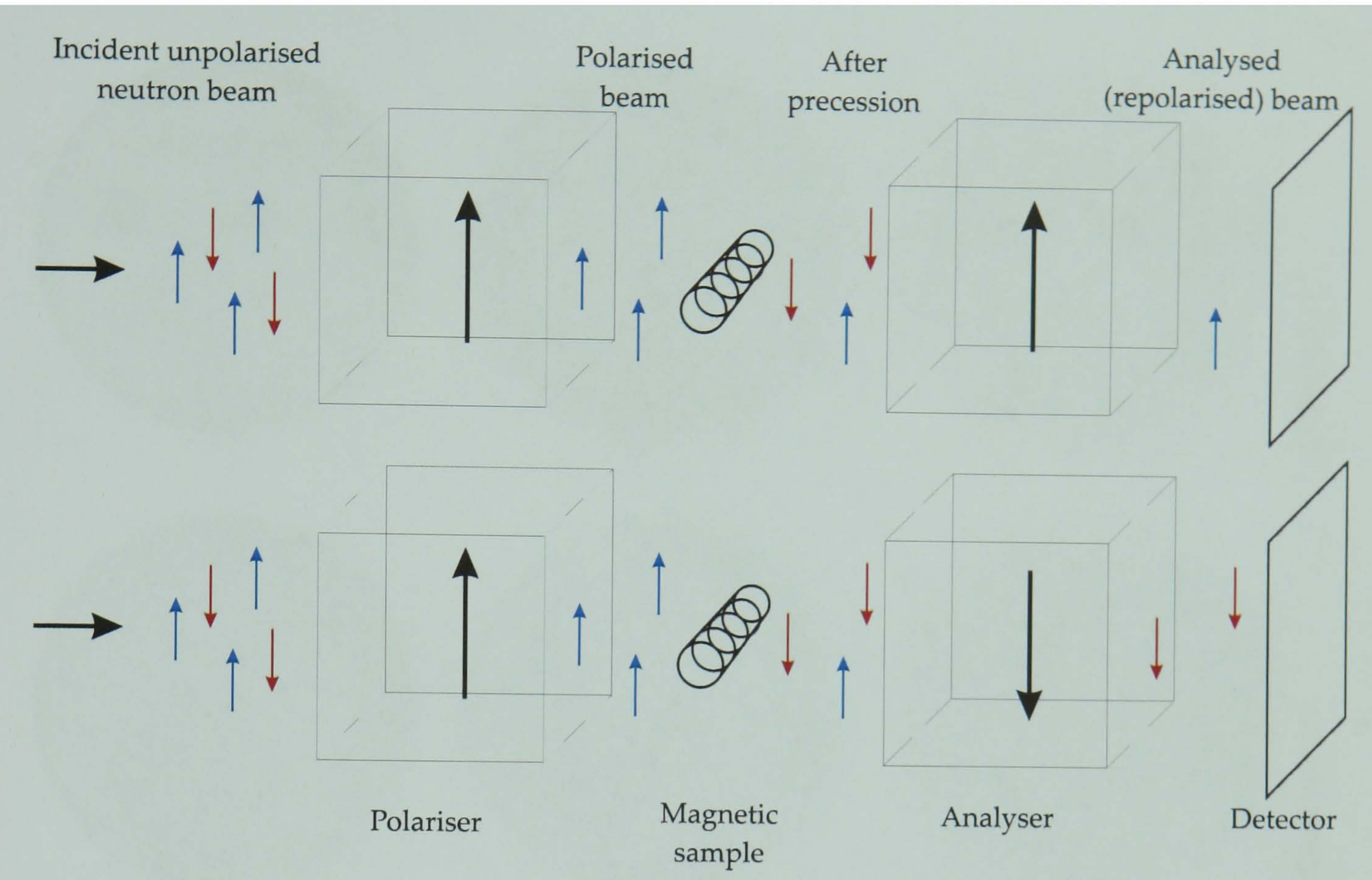

Figure 5.13: *The basic principle of image formation using only non-spin-flipped and only spin-flipped neutrons. The number of neutrons in each state is related to the magnetic field distribution of the sample.*

spin-flipped image. The flipping ratio is related to the depolarisation and polarisation by

$$D = 1 - \left(\frac{F - 1}{F + 1} \right) = 1 - |P| \qquad \text{Equation 5.17}$$

(In order to measure the depolarisation directly, the spin-flipped image should be divided by an image formed using the polarised beam in the absence of an analyser.)

Figure 5.14 shows the non-spin-flipped, spin-flipped, and depolarisation images for three samples: a steel sheet (~*50 μm* thick) with three bored holes (*1, 3,* and *5 mm*) and a cut slit; a rusted steel sheet (~*100 μm* thick); and an assortment of steel and stainless steel nuts, bolts and washers.

The non-magnetic regions of the *50 μm* steel (the holes) have a low effective

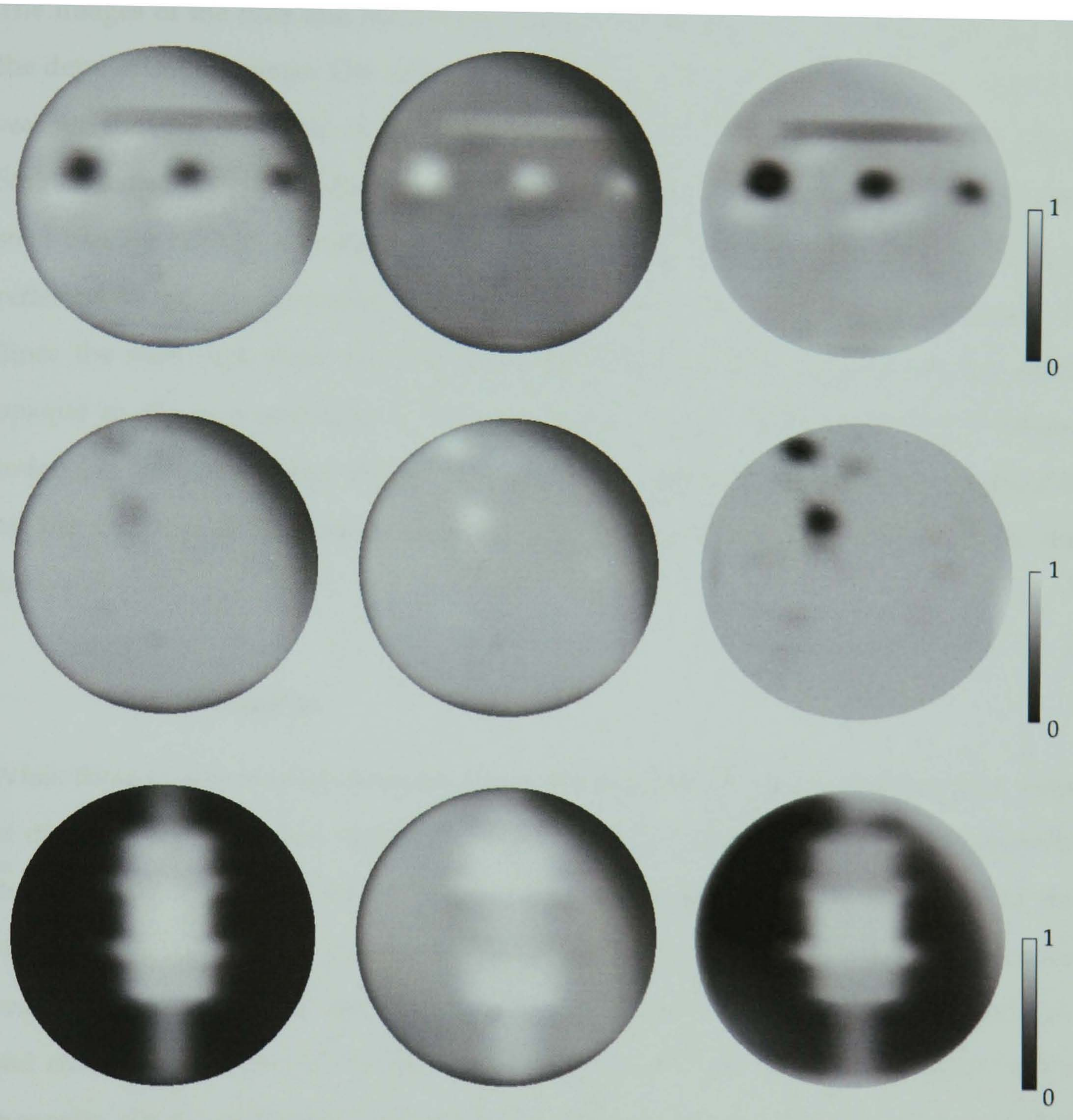

Figure 5.14: *Non-spin-flipped (left), spin-flipped (centre), and the depolarisation (right) images for a steel sheet with three bored holes (5, 3, and 1 mm, from left to right) and a cut slit (top); a rusted steel sheet (centre); and an arrangement of steel and stainless steel nuts, bolts and washers (bottom). The scale bars show the depolarisation. The field of view is 50 mm.*

attenuation (black) in the non-spin-flipped image, a high effective attenuation (white) in the spin-flipped image and have zero (black) depolarisation. The steel itself has a depolarisation of *~0.8*, although there are regions around each of the bored holes where the depolarisation rises to *1*, indicative of some magnetisation induced by changes in the structure of the steel. The steel in the in the *100 μm* sheet has a depolarisation of *~0.9*, although this falls to zero in several places where the rust penetrates the sheet.

The images of the nuts and bolts is most easily understood working backwards from the depolarisation image. The central nut and the washer beneath it are steel, while the washer above it, the nuts at the top and bottom and the bolt are all stainless steel. Stainless steel usually has the magnetic, austenite structure (face-centred cubic), while steel usually has the non-magnetic, ferrite structure (body-centred cubic), and this is reflected in the depolarisation of the stainless steel, *~0.85*, compared to the steel, *~1*. Since the steel flips more neutrons than the stainless steel it appears slightly more opaque in the non-spin-flipped image, and less opaque in the spin-flipped image. Indeed, in the spin-flipped image the attenuation of the steel is roughly cancelled out by the fact that it flips more neutrons (which are more easily transmitted by the analyser).

5.3.5 Discussion

While these results may be viewed in one sense as trivial (there are much simpler ways of distinguishing between steel and stainless steel, for example), they do demonstrate the first stages in what could develop into an extremely useful technique in the visualisation of magnetic structures. Once refined, imaging with polarised neutrons could find multitudinous applications throughout science: the investigation of stress- and strain-induced changes in the magnetic properties of materials; the study of the magnetic effects associated with superconductivity and electrical currents; and (the ultimate goal) the three-dimensional imaging of individual magnetic domains.

One obvious (and much needed) improvement is in the spatial resolution (*~1 mm*), which requires the sample-detector distance to be reduced. Currently this is not possible because the positioning of the analyser means that this distance is *~30 cm*, but it may be possible to design a magneto-static cavity with a more open structure that allows samples and detectors to be positioned very close to the faces of the helium-3 cell; this would certainly be a worthwhile development. A further challenge still is the development of reliable algorithms to assist in the extraction, analysis and visualisation of the magnetic structure information.

6 Applications

Over the past decade, neutron imaging techniques have gradually gained in importance for scientific and industrial investigations, although they are nowhere near as widely exploited as x-rays because they generally have a coarser spatial resolution and a lower radiation flux, and there are relatively few neutron imaging instruments worldwide. Neutrons do, however, have several advantages over x-rays, including their ability to penetrate thick layers of heavy metals, to distinguish between many elements of similar atomic number and isotopes of the same element, and to detect small amounts of light elements such as boron, lithium and hydrogen. This final point can be important, since many chemical, biological and industrial processes involve hydrogenous material (water, organic solvents, adhesives, petrochemical derivatives, biological tissue, etc.).

Palaeontology

Studying the history of life on Earth through fossilised remains (skeletons, shells, eggs and tracks) and the rocks in which they are found can give a valuable understanding of the evolutionary relationships between different species and the environments in which they lived, and the occurrence of geological events. Although x-ray imaging has been successfully employed in palaeontology [73, 74], one difficulty faced is that fossils often have a very similar chemistry to the sediments in which they are found, meaning that there is little attenuation contrast between the two. Neutrons will also usually fail in such cases, unless there are traces of remnant organic material – recall that neutrons are highly sensitive to hydrogen, while x-rays are not (Figure 2.8).

6.1.1 *Araucaria* fossil

Abundant fossilised remains of a new flora have been discovered in sedimentary La Meseta strata on Seymour Island, West Antarctica [75]. This plant material is exceptionally well-preserved (branches, twigs, leaves, cone scales and seeds are all present) and has been identified as an extinct relative of *Araucaria araucana*, the Monkey Puzzle tree. These conifers are althought to represent the dominant vegetation growing in dense forests on the slopes of an active volcanic arc at 65°S (now the Antarctic Peninsula) during the the late Early Eocene Era (approximately 53 million years ago), where the environment and climate were probably similar to the natural habitat of *Araucaria araucana*: the lower slopes of the south-central Andes of Argentina and Chile, South America, where the volcanic soil is fertile and well-drained, the rainfall is high and reliable, and the temperature is mild with a narrow annual swing between seasons.

Analysis of the mineralogy using x-ray diffraction, cathode luminescence and scanning electron microscopy indicates that the rock matrix is a quartz-feldspar carbonate-cemented sandstone concretion and that the fossils were permineralised by calcite, although some lignified organic matter has been retained. While possible to demarcate the fossil-matrix boundary optically (Figure 6.1), it is expected that the chemical make-up is too uniform (the ensemble is primarily calcium carbonate) to be differentiated by x-rays, although this has not yet been verified. Neutron tomography (experimental parameters given in Table 6.1) of a medium-sized sample *(101×49×106 mm)*, however, yielded an identifiable contrast, with the fossil being *~9%* more attenuating than the matrix (Figures 6.2 and 6.3). This is surmised to result from the presence of organic material, which (assuming this is true) accounts for *~3-5%* of the fossil material in this specimen (thermal neutrons: $\sigma\{\mathrm{H}\}=82.36$ *barn*, $\sigma\{\mathrm{CaCO_3}\}=21.56$ *barn*). The fossil has been

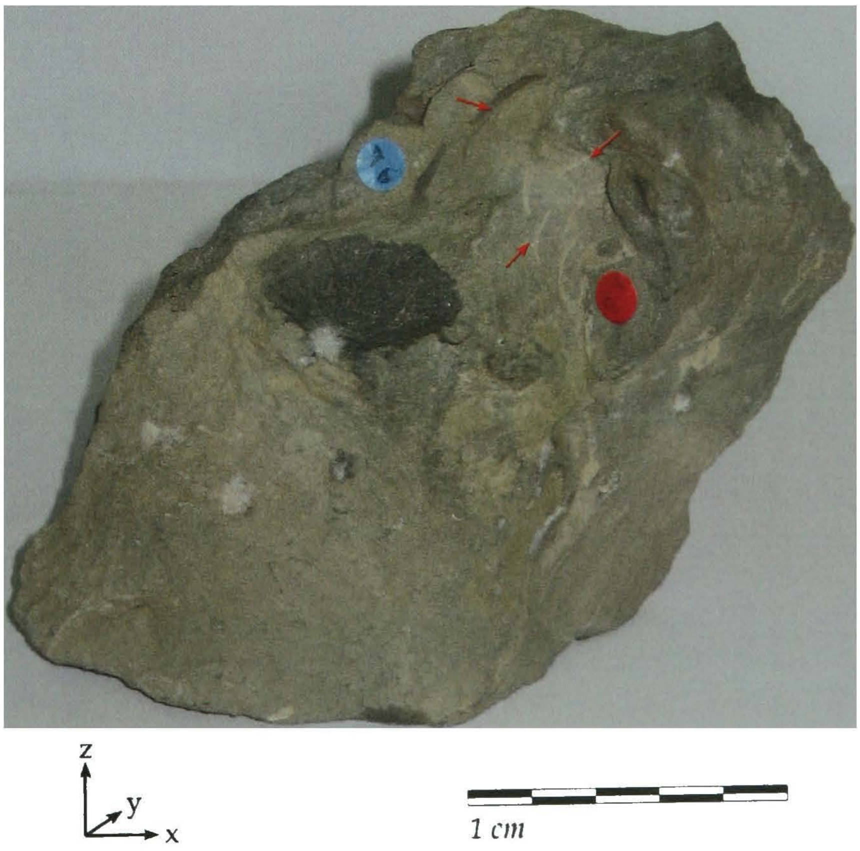

Figure 6.1: *A photograph of a carbonate concretion containing a fossil (parts indicated by red arrows) of a new flora discovered on Seymour Island, West Antarctica.*

preserved in its original three-dimensional form – a spiral of thick, triangular leaves winding around a central branch – making its resemblance to *Araucaria araucana* particularly evident (Figure 6.4).

Camera	Andor iXon
Lens	35 mm
Camera box *[cm]*	100
Rotation angle	π
Projections	801
Exposure per projection *[s]*	10 [100×100 ms]

Table 6.1: *Experimental parameters used for a tomographic study of a fossilised Araucaria plant.*

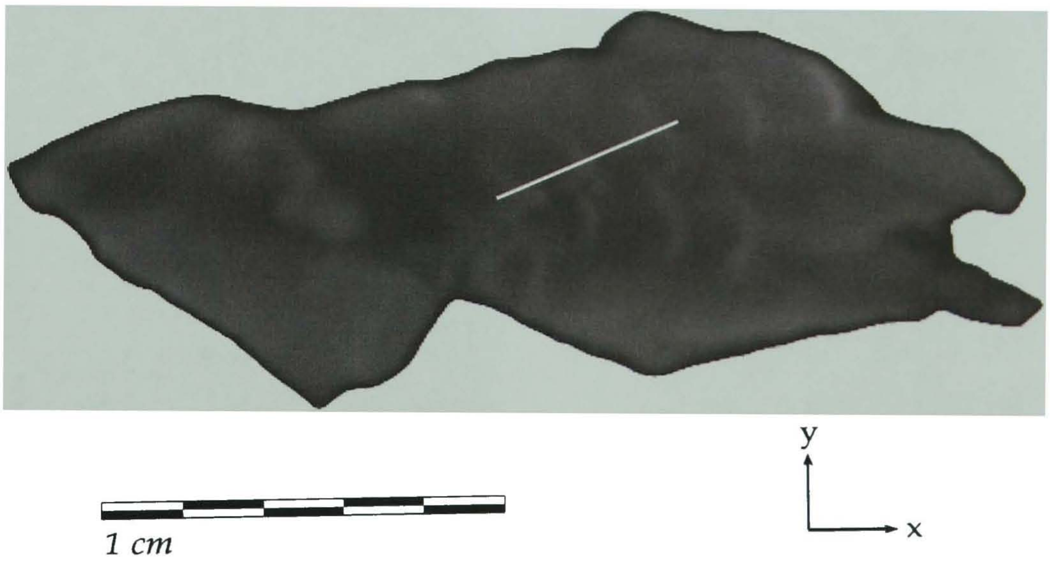

Figure 6.2: *A reconstructed slice (72 mm from the bottom) of an Araucaria fossil (brighter areas) inside a rock matrix.*

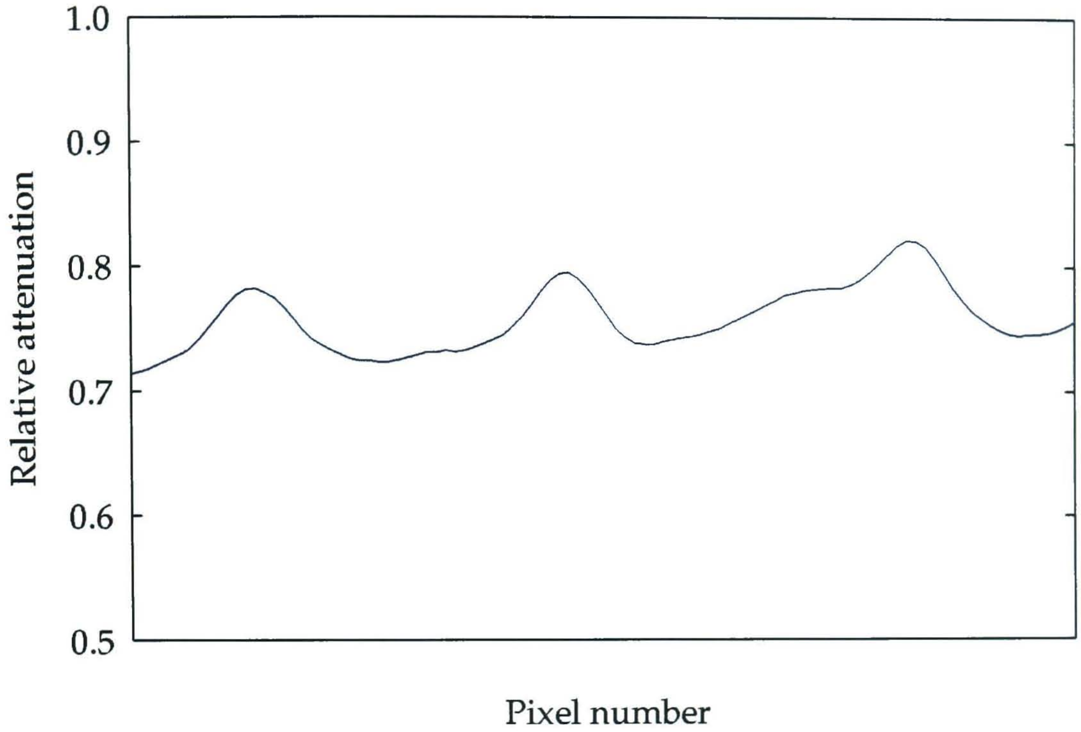

Figure 6.3: *A plot of the relative attenuation values along the white line in* Figure 6.2. *The peaks correspond to the position of the leaves.*

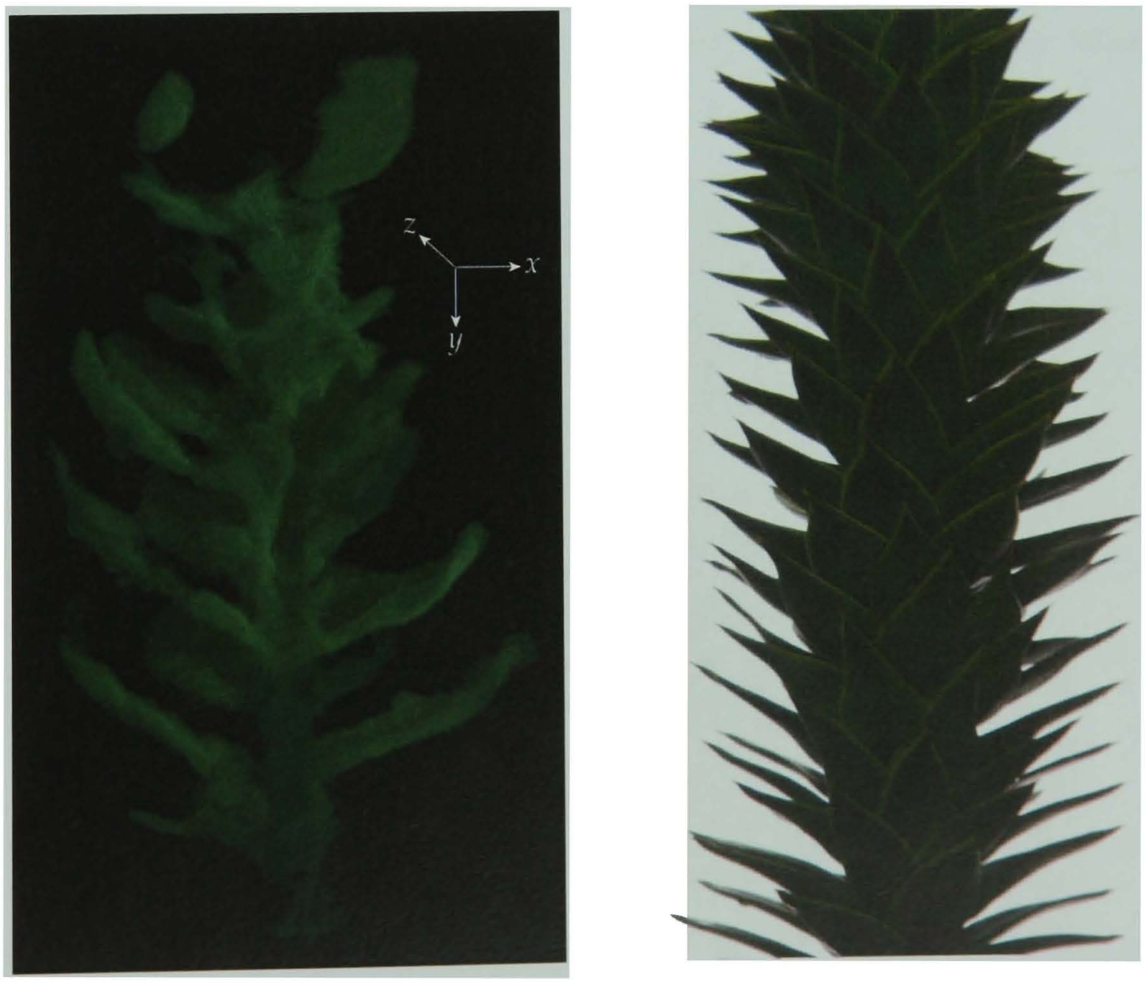

Figure 6.4: *A reconstructed 3-D rendering of an Araucaria fossil (left) still held in its three-dimensional form, much resembling Araucaria araucana, the Monkey Puzzle tree (right).*

6.1.2 Mysticete whalebone

A fossilised piece of whalebone (*30×15×20 mm*) (Figure 6.5) was imaged with neutrons (experimental parameters given in Table 6.2) in order to track the internal paths of several interesting features that are visible at the surface and to determine their probable functions and origins. The piece of bone was found in the lower Pysht Formation of the Olympic Peninsula in Washington State, USA, and came from the top of the skull of a mysticete whale living in the Early Oligocene Era (approximately 31 million years ago).

The mineral composition of the fossil, as determined by scanning electron microscope, is micritic calcium carbonate, while the features, once cavities within the bone, are now also filled with micritic calcium carbonate, but lined with pyrite [76]. Despite having the same composition, the filled-in regions are less attenuating than the bone matrix, presumably because they have a lower density (Figure 6.6). Most of the channels are straight, smooth, and tubular in shape, run roughly parallel to one another, and range in diameter from *~0.5-1.5 mm*, although one is much larger, *~3 mm* in diameter. These

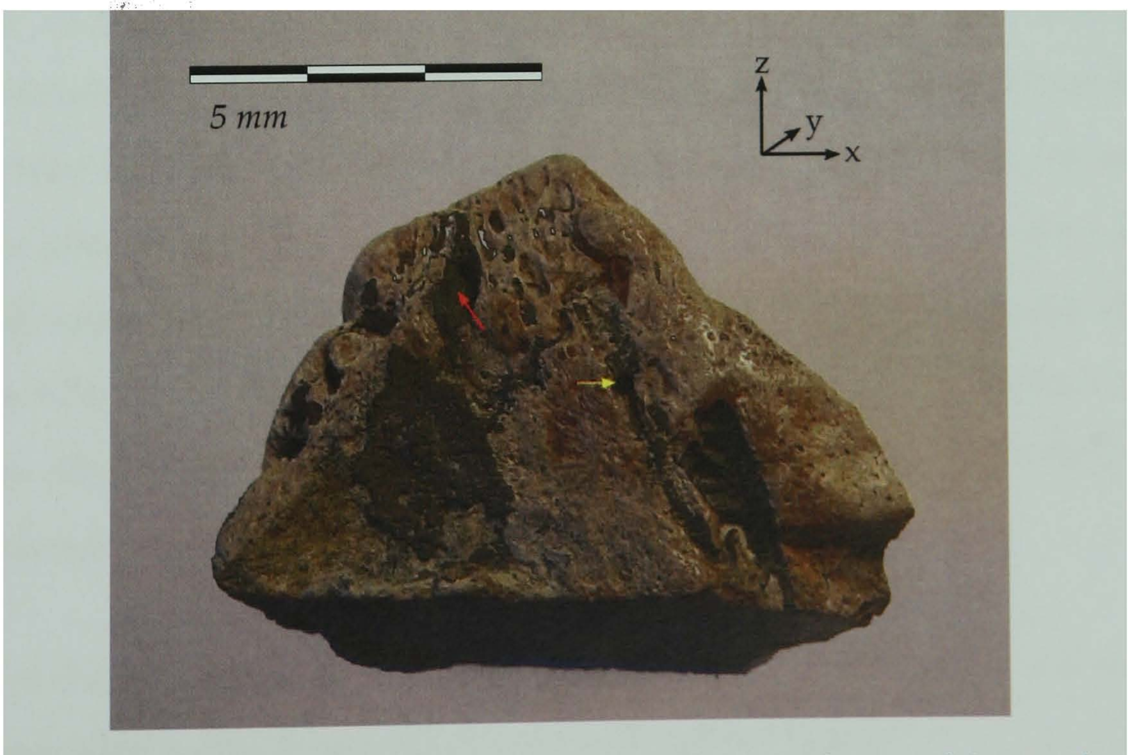

Figure 6.5: *A photograph of a fossilised piece of whalebone with several interesting features, such as the large (red arrow) and small (yellow arrow) channels, interpreted as Haversian canals.*

Camera	Andor iXon
Lens	50 mm
Camera box *[cm]*	70
Rotation angle	π
Projections	801
Exposure per projection *[s]*	8 [100×80 ms]

Table 6.2: *Experimental parameters used for a tomographic study of fossilised whalebone.*

are interpreted as being Haversian canals, passages for blood vessels and nerves through compact bone. There is also a winding channel running roughly perpendicular to the others, which appears to join several of the Haversian canals together. One possibility is that this is a Volkmann's canal, a passage that connects the Haversian system to the periosteum (the dense fibrous membrane covering the surface of bones).

Curiously, x-rays reveal very little of the structure present in the neutron data (thermal neutrons: $\sigma\{\mathrm{CaCO_3}\}$=*21.56 barn*, $\sigma\{\mathrm{FeS_2}\}$=*17.70 barn; 100 keV* x-rays: $\sigma\{\mathrm{CaCO_3}\}$=*32.50 barn*, $\sigma\{\mathrm{FeS_2}\}$=*55.84 barn*) (Figure 6.7). Although several of the smaller Haversian canals contrast very well (being less attenuating, which again suggests that the in-filling is less dense than the surrounding matrix), little of the pyrite lining is evident. Either the pyrite only exists close to the surface (cf. the brightest regions on the right hand surface in Figure 6.7), or the layer is too thin to be effectively detected. Indeed, the larger Haversian canal is almost completely imperceptible and can only be inferred through the knowledge of its position imparted by the neutron data.

It is hoped that the future serial grinding and optical examination of this sample will shed further light on the identity and function of these features.

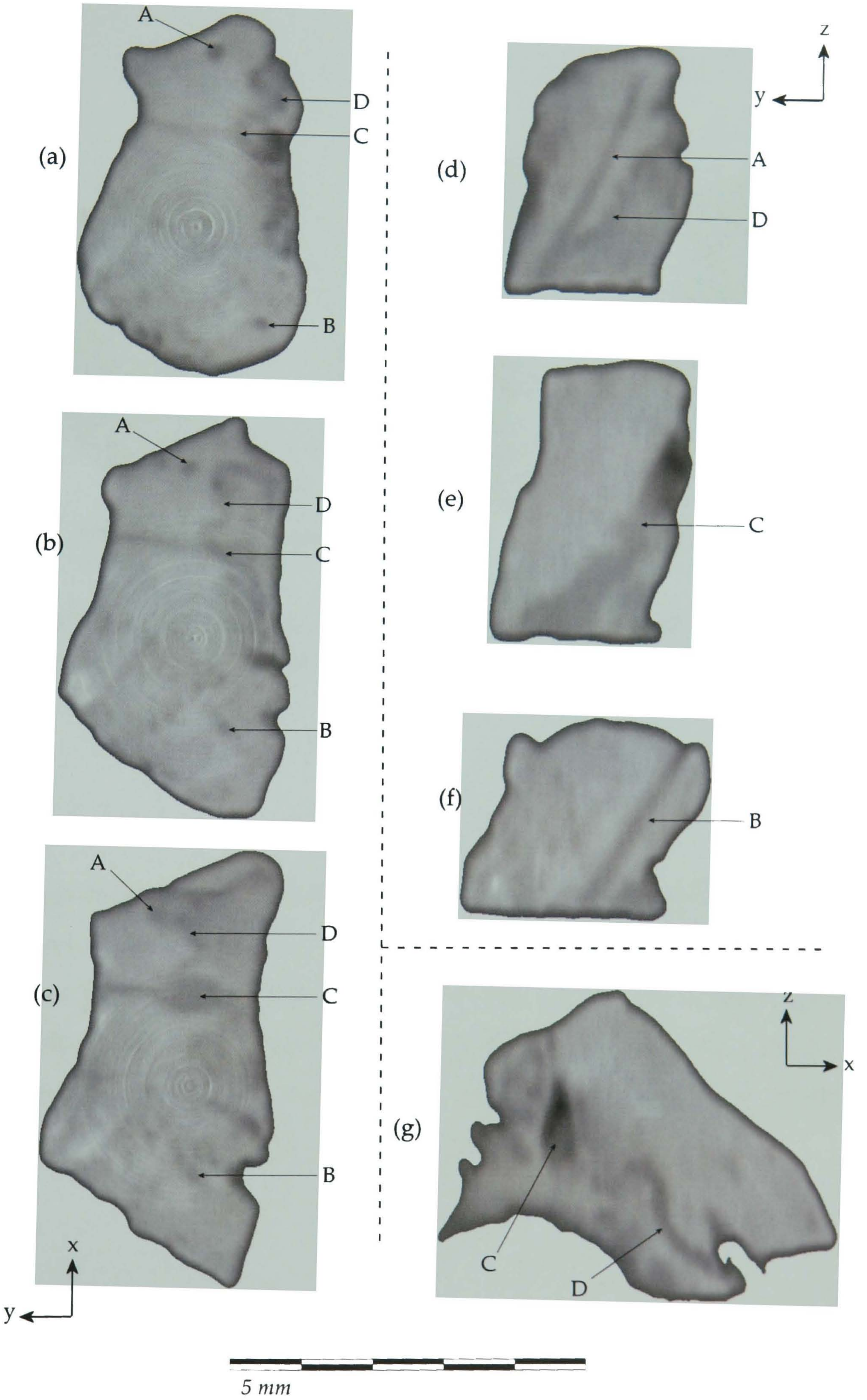

Figure 6.6: *Slices reconstructed from neutron data of the fossilised piece of whalebone (a) 10 mm, (b) 6 mm, and (c) 3 mm from the bottom, highlighting two small (A and B) and one large (C) suspected Haverisan canals, and one suspected Volkmann's canal connecting the three (D).*

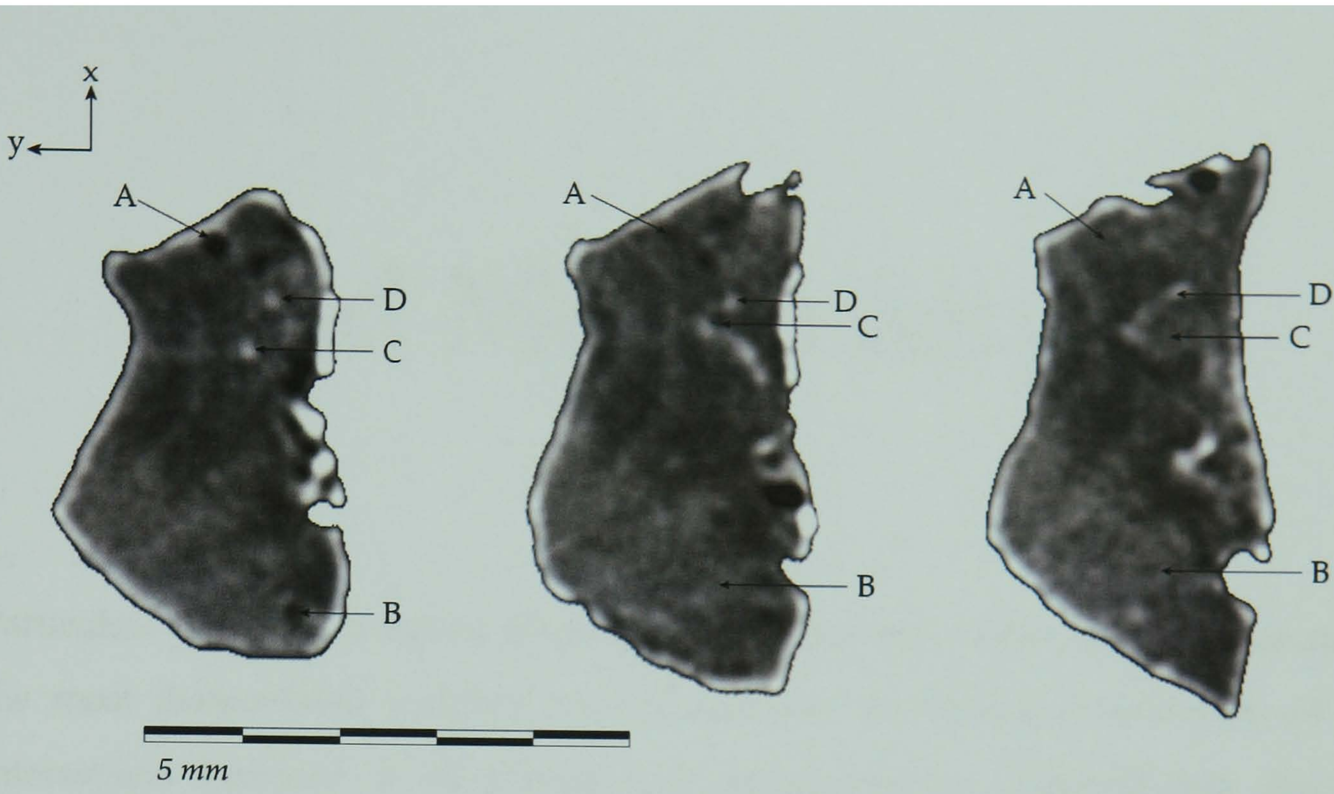

Figure 6.7: *Slices reconstructed from x-ray data of the fossilised piece of whalebone (a) 10 mm, (b) 6 mm, and (c) 3 mm from the bottom (corresponding directly to* Figure 6.6 *(a), (b) and (c), respectively).*

6.1.3 Discussion

Although the suitability of neutron imaging for studying and identifying macroscopic structures in palaeontological specimens has been demonstrated, its overall impact is tempered by the coarse spatial resolution currently attainable. Nonetheless, neutrons may still prove useful in detecting small amounts of latent organic material, and in revealing the position and extent of features concealed inside a matrix – information that would be conducive to the targeted use of more refined techniques.

Fluid Mechanics

Particulate flows are abundant in nature and industry (after water, granular material is the most manipulated material), and an accurate mathematical modelling of the interactions involved is of fundamental importance to understanding physical processes such as the transportation and packing of granular materials, and particulate mixing and segregation. Examples include the filling and discharging of silos, rockfalls, avalanches, and sand dune formation and rippling. Relatively small systems can be studied under laboratory conditions, but even relatively simple situations are capable of exhibiting highly complex behaviour and it is often only possible to observe the outer surfaces of these flows (e.g. from the top or the side); the interior behaviour remains elusive and is troublesome to observe quantitatively or qualitatively. The difficulty of obtaining good experimental data makes it difficult to verify the predictions of mathematical models, and, as a consequence, granular materials are poorly comprehended.

6.2.1 Methodology

One important parameter of granular systems is how the grains pack together and how their packing density varies through a bulk volume. Beam attenuation, A, depends on the material attenuation coefficient, α, and the length of the beam path through the material, s, according to (from Equations 2.2 and 4.1) $A = (\alpha \cdot s)$. Therefore, for any homogeneous material (i.e. where the attenuation coefficient within the material is constant), the beam attenuation depends only on the path length. For a granular material, s will be the sum of path lengths through several grains, which may be equal to or less than the total thickness of the system under consideration, ς (the difference will be made up by air voids). The attenuation is given by $A = \alpha \cdot n \cdot \varsigma$, where n is the packing fraction of grains along s as defined by $n = s / \varsigma$. Since, the measured attenuation (and therefore the grey-scale pixel value in a radiograph) is directly proportional to the packing fraction of the grains (Figure 6.8), the latter is thence experimentally measurable (via calibration measurements of a sample of known packing density). Figure 6.9, for example, shows the density variations associated with the propagation of a funnel channel formed by grains draining from a rectangular hopper through a circular orifice at the centre of the base.

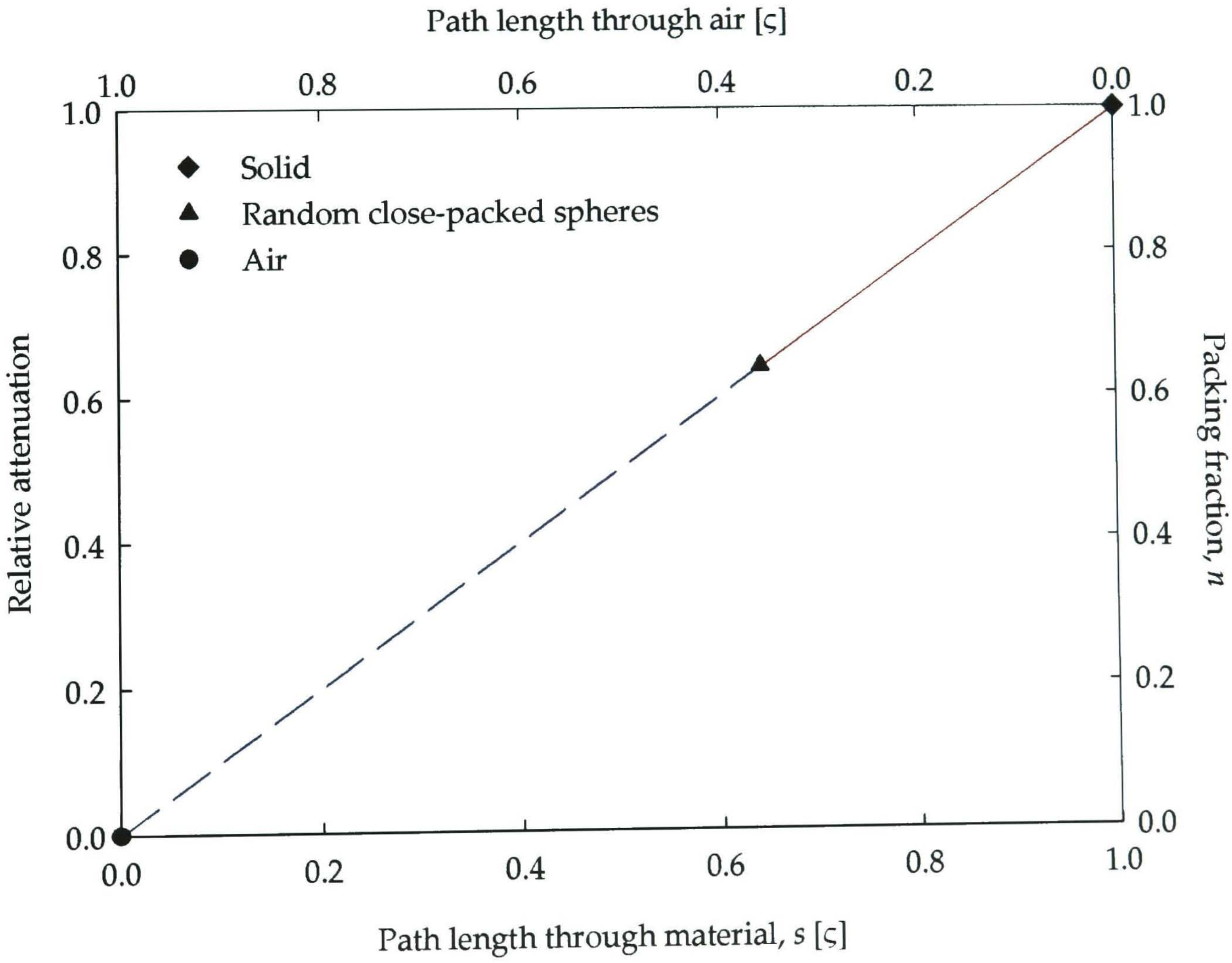

Figure 6.8: *Model values showing the relationship between grain packing density and beam attenuation. (It is assumed that the attenuation of air is zero).*

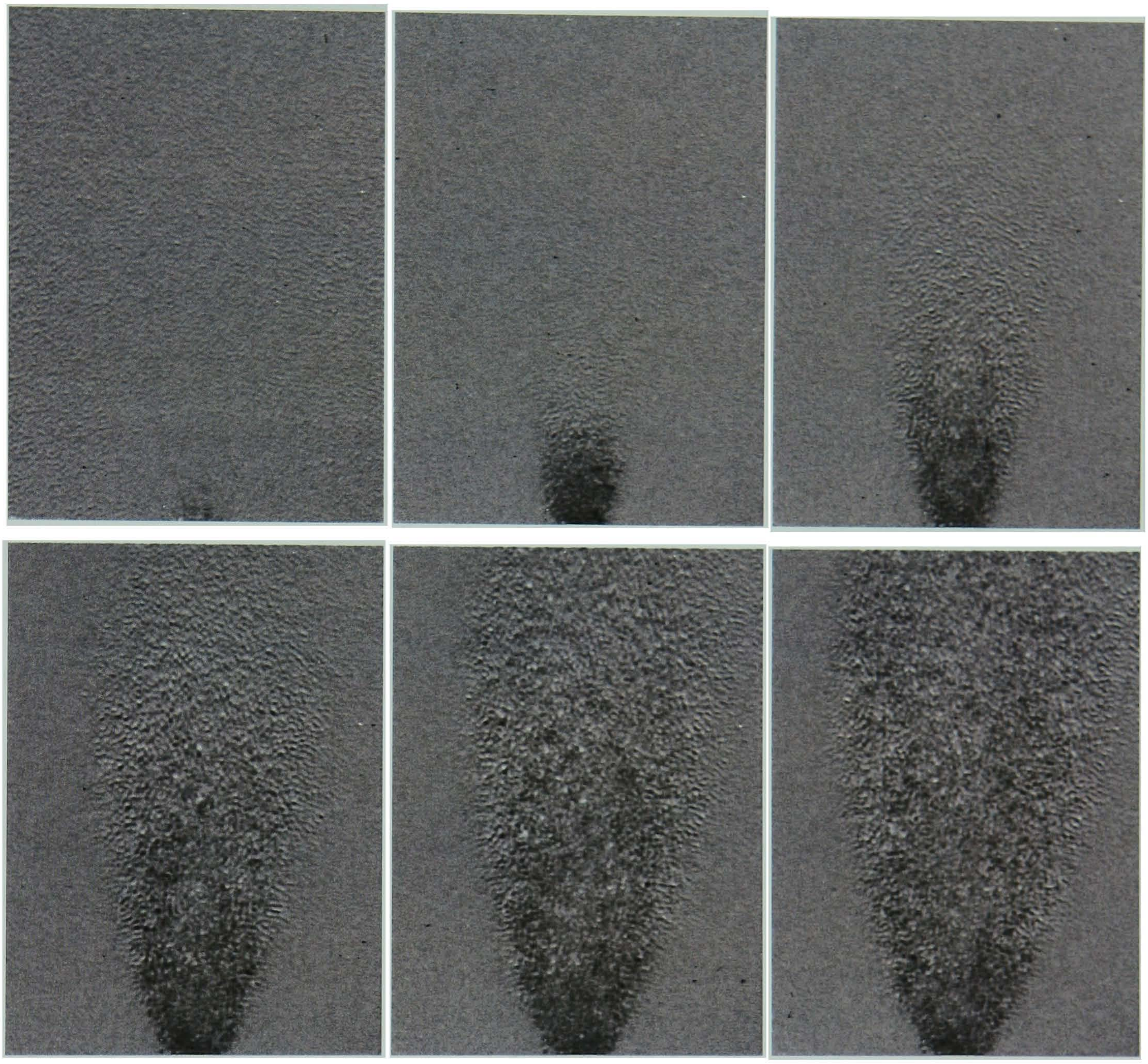

Figure 6.9: *A series of radiographs showing the density variations associated with the propagation of a funnel channel formed by grains draining from a rectangular hopper through a circular orifice at the centre of the base. Darker areas are regions of lower density. The time elapsed between images is 100 ms. The left, right and lower surfaces of the system correspond to the left, right and lower limits of the field of view, but the upper surface of the system is several cm above the upper limit of the field of view.*

6.2.2 Grain distribution in dense flows

Loose, cohesionless grains flow whenever they are stacked (or placed on a steep slope) beyond their angle of repose, at which point gravity-induced shear occurs at the base. The segregation of sheared granular media (whether by agitation or flow) is a well-known phenomenon, wherein larger grains migrate towards the upper surface of the bulk (even when all the grains have the same material density) to created size-ordered striation [77]. In dense or energetic flows this layering is predominantly caused by kinetic sieving, which is a consequence of the changes in local void spacing that develop during flow; as voids open between grains, smaller grains are more likely to fall (downwards) into them than are larger particles and thus percolate towards the lower surface of the flow, while large particles are levered towards the upper surface. Counteracting this effect is a diffusive remixing (or dispersive pressure) that arises from the random trajectories of individual grains as they collide with one another, causing them to mix together. This leads to the formation of a series of sorted layers (containing only one grain size) separated by transition regions (containing a mixture of grain sizes), whose relative sizes (and thus the smoothness of the transition) are determined by the relative strengths of these two competing processes.

The system selected to study this grain segregation consisted of a fifty-fifty mixture of large sugar (*1.54 mm*) and small glass (*720 μm*) spherical grains discharged into an aluminium chute (*120×6×10 cm (l×w×h)*) inclined at an angle of *28°* to the horizontal from a hopper (*30×6×30 cm (l×w×h)*) at the elevated end. The hopper and the chute were connected by a remotely-operated sluice gate (*6×1 cm* (*w×h*)), and the top of the whole apparatus was left open in order to reduce any pressure effects caused by trapped air. Although the flow in such a system is relatively shallow (typically several *mm* deep), upon reaching the closed end of the chute there is a sudden change in the flow regime. A bore (or shock) is formed, which returns to expand the flow into a thick (typically several *cm* deep), stationary deposit (Figure 6.10). This final deposit represents a steady state of the grain distribution within the flow.

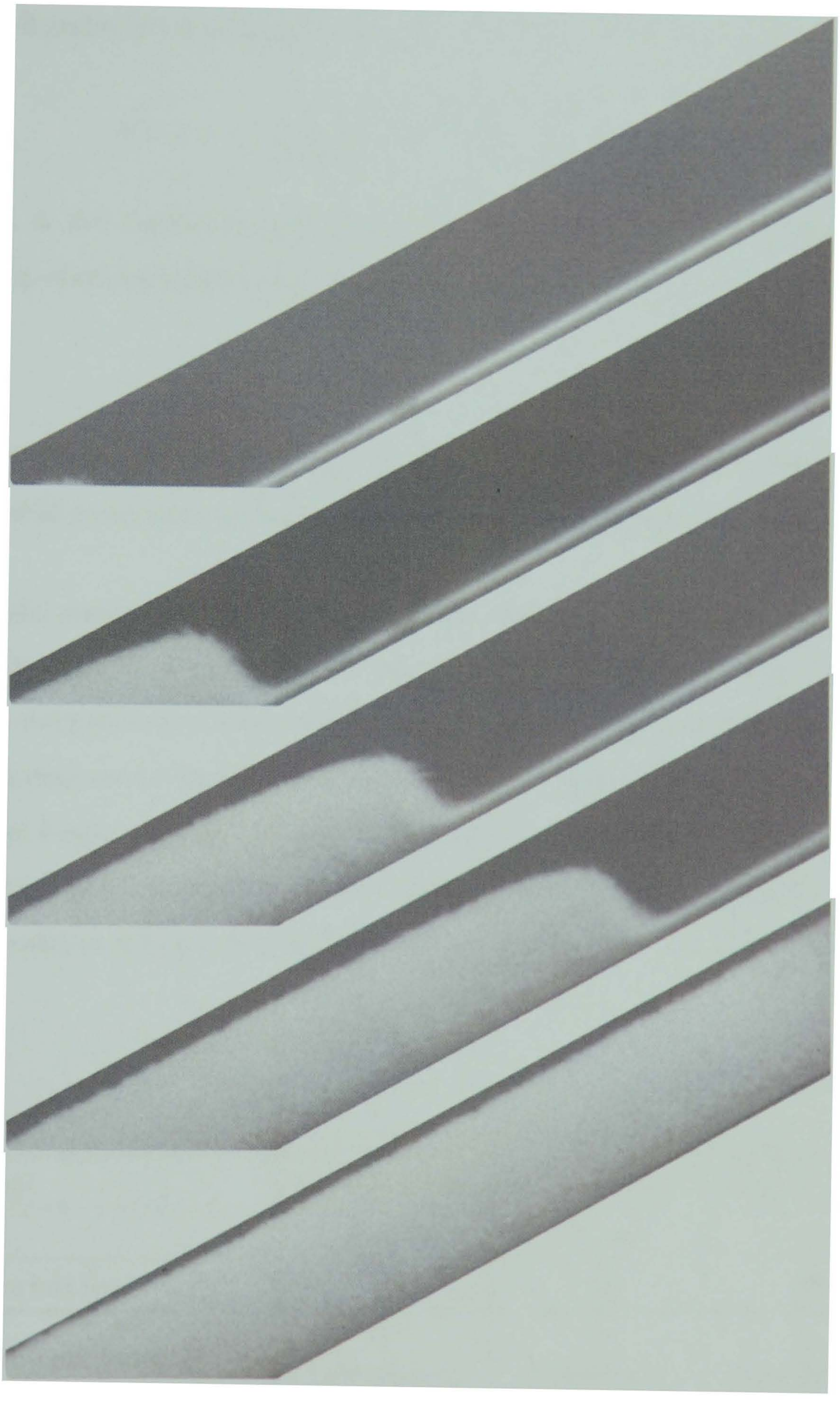

Figure 6.10: *A series of radiographs showing a granular flow (from right to left) and the returning bore (from left to right) in a chute inclined at an angle of 28° to the horizontal. The lower image shows the stationary final deposit. Neither the hopper nor the closed lower end of the chute are shown in these images.*

A model has been proposed [78, 79], which describes the variation in the concentration of the small grains, ϕ^s, as a function of height, z, throughout this final deposit

$$\phi^s = \frac{\left(1 - e^{\left(-\phi_m/z_0\right)}\right) e^{\left(\left(-\phi_m - z\right)/z_0\right)}}{1 - e^{\left(-\left(1-\phi_m\right)/z_0\right)} + \left(1 - e^{\left(-\phi_m/z_0\right)}\right) e^{\left(\left(-\phi_m - z\right)/z_0\right)}} \qquad \text{Equation 6.1}$$

where ϕ_m is the depth-averaged grain concentration, and z_0 is the dimensionless segregation-remixing length-scale. The model assumes that

$$\phi^s + \phi^l = 1 \qquad \text{Equation 6.2}$$

where ϕ^l is the concentration of large particles (i.e. the total volume of the grains and the interstitial pores space is constant and the latter can be subsumed into the former).

Radiography measurements were made of the deposit at positions δ_{30}, δ_{70} and δ_{100}, located *~30 cm*, *~70 cm* and *~100 cm* respectively from the lower end of the chute (experimental parameters given in Table 6.3). The images (after normalisation to initial conditions (Section 4.1.1)) were then transformed into plots of the packing fraction as a function of height through the deposit and fitted to Equation 6.1 (Figure 6.11). The experimental data show good agreement to the theoretical model reasonably well, with all three positions fitting well to the same parameters, $\phi_m=0.5$ and $z_0=0.15$.

	δ_{30}	δ_{70}	δ_{100}
Camera	PCO SensiCam	PCO SensiCam	PCO SensiCam
Lens	35 mm	50 mm	35 mm
Camera box *[cm]*	100	100	100
Exposure per frame *[s]*	5 [100×50 ms]	5 [100×50 ms]	5 [100×50 ms]

Table 6.3: *Experimental parameters used for a radiographic study of the stationary deposit of a granular flow* .

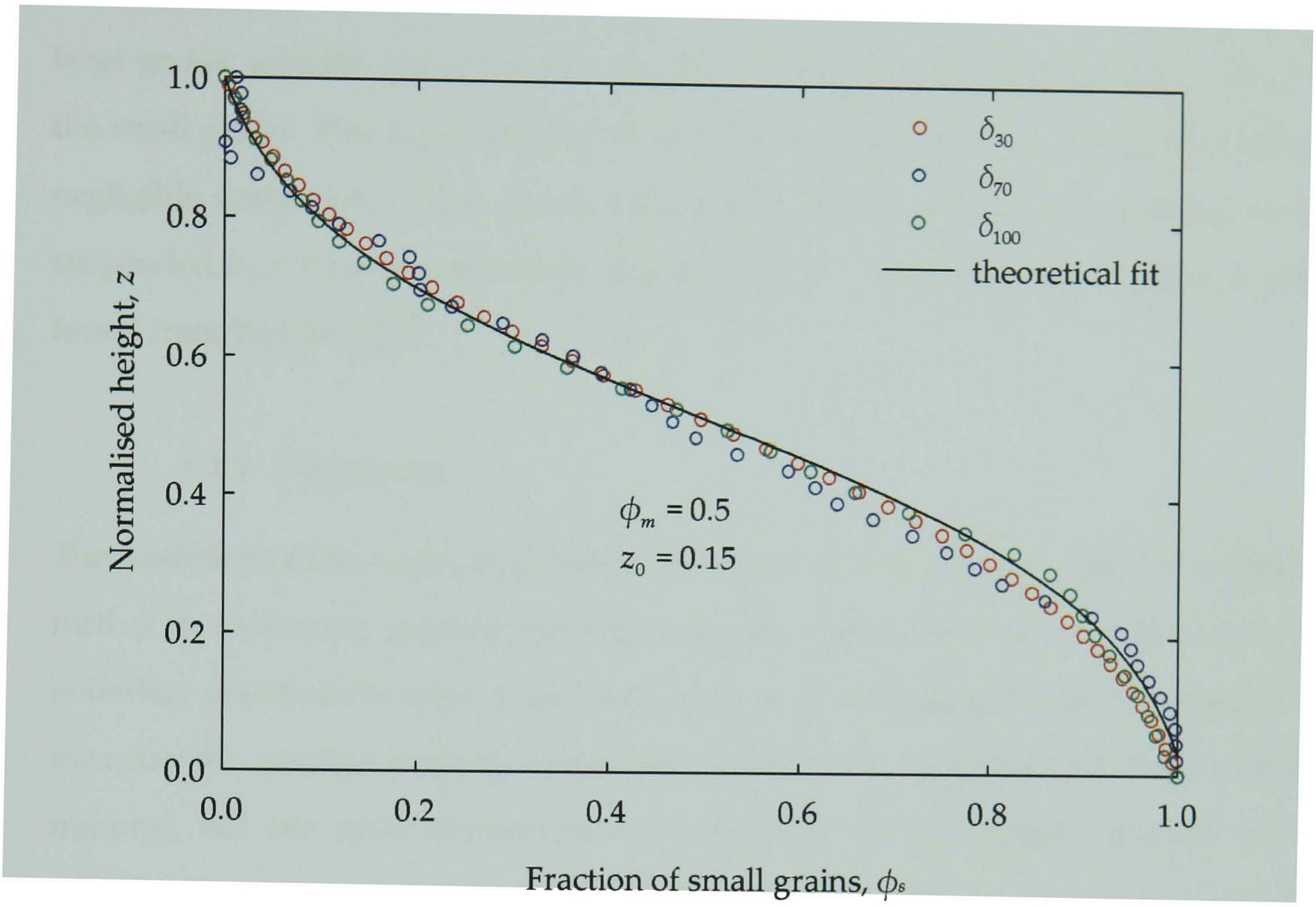

Figure 6.11: *A plot showing the concentration of the small grains as a function of height through the deposit for three positions* δ_{30}, δ_{70} *and* δ_{100}, *located ~30 cm, ~70 cm and ~100 cm respectively from the lower end of the chute.*

The significance of the result $\phi_m=0.5$ is that the mean local concentration of small grains is *50%*. Since the mixture in the hopper also contained *50%* small grains, this indicates that there was only a weak shear within the flow and that little grain segregation occurs inside the hopper. (A strong shear would tend to to push the large particles towards the front of the flow and the small grains towards the rear, resulting in ϕ_m increasing towards the top of the chute). The value of z_0 is more difficult to interpret. It is defined as a measure of segregation-remixing effects ($z_0=0$ corresponds to no remixing, $z_0 \to \infty$ corresponds to no segregation) and is related to the grain sizes and the velocity profile in the flow, but it is not currently possible to calculate values theoretically – they must be found from test measurements of the system under investigation.

It should be noted that in this example the measured packing fraction is that of the large grains, with the role of the air voids discussed in the methodology being filled by the small grains. This is justified by the fact that the attenuation of the small grains is negligible compared to that of the large grains, which can thus be assumed to be suspended in a transparent matrix. The packing fraction of the small grains is then found from Equation 6.2.

6.2.3 Discussion

The feasibility of this method has been proven and there is a clear potential to exploit it further in measuring granular packing fractions. One concern is the contribution of boundary effects at the edge of the chute, since with a radiograph it is only possible to measure the average packing across the volume. It is expected that these will be minimal, but one great improvement would be to use tomography instead, which would allow characterisation of the packing density variations not only along the length and height of a flow, but across its width. This will prove difficult with neutrons because rotation of the sample will likely disturb the grains, but could easily be achieved with a standard medical x-ray scanner.

Archaeology

Tomographic studies can allow compositional and structural characterisation of archaeological artefacts, which are often fragile, dirt-engrained and in a continuing state of deterioration. This can provide an insight into how materials were combined and implements were assembled. Figure 6.12 (experimental parameters given in Table 6.4) shows a pottery sherd (*43×65×9 mm*) from the wall of a food vessel dating from the Bronze age (circa BC *1800-2000*), which was excavated from the area between East and West Heslerton in North Yorkshire, England, a site of human activity and settlement since the late Mesolithic (circa BC *5000*) [80, 81]. It is possible to delineate six parallel bands (~*9 mm* thick), indicating that the bowl was coil-built (formed by coiling rolls of clay) [82]. Embedded within these are numerous rounded, irregular inclusions (probably grit, crushed pottery (grog) or flint), which were introduced arbitrarily during fabrication to temper the pottery and to limit crack formation and propagation.

The ability to identify the coil structure within the roughly homogeneous material in this example is althought to arise from its extreme coarseness rather than any special suitability or applicability of neutron imaging. The large inclusions (~*1-5 mm*) prevent the coils from stacking smoothly, opening up the structure between the bands with air voids, and it is anticipated that x-rays would produce equally good results. However, one area of research where neutrons are expected to perform significantly better is in the investigation of archaeological artefacts with metallic components.

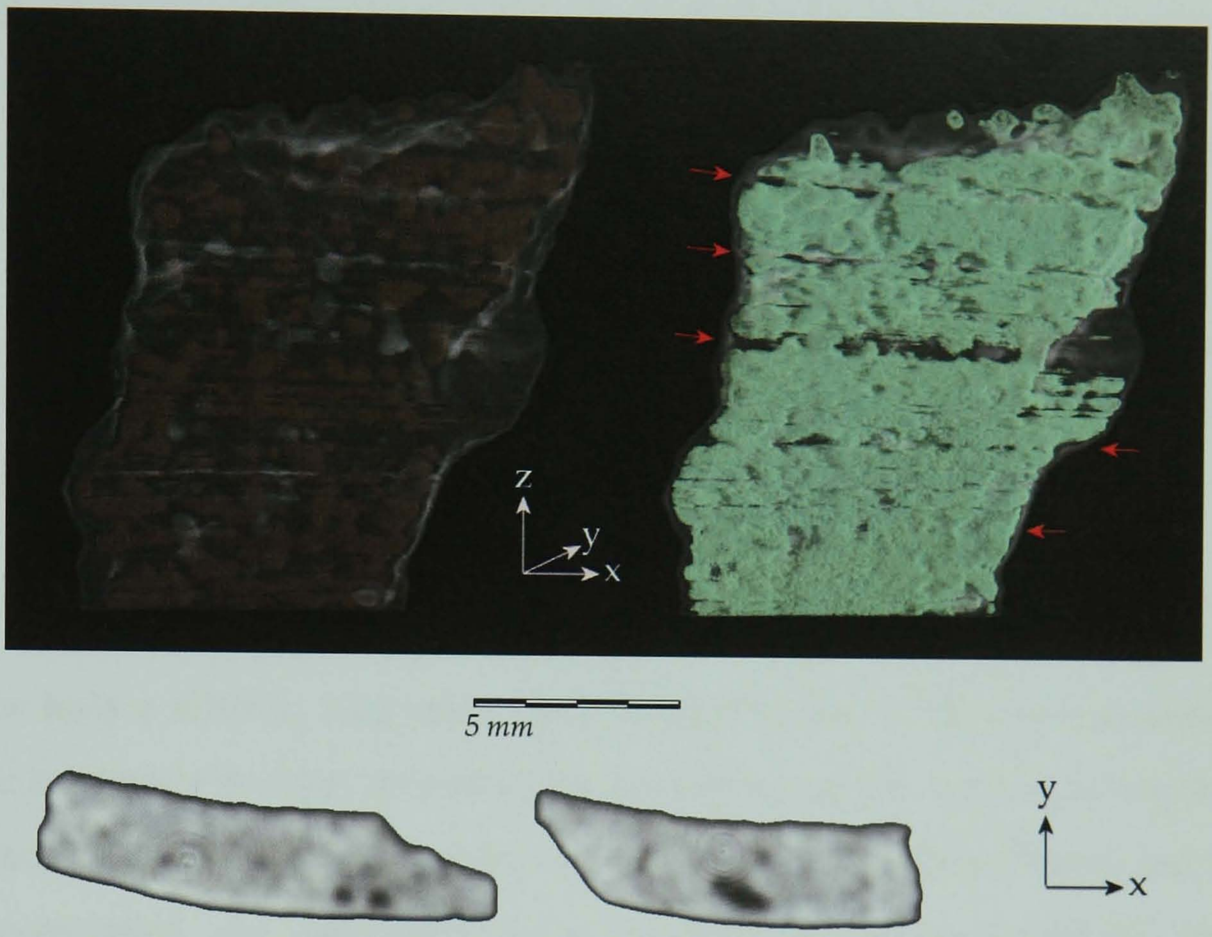

(a) (b)

Figure 6.12: *Tomographic reconstruction of a pottery sherd, showing the inclusions (top left) and the clay bands (top right). The band edges are indicated by the red arrows. The reconstructed slices taken (a) 3 mm and (b) 23 mm from the top show the presence of inclusions (brighter spots) and voids (darker spots). (See also* Appendix C*).*

Camera	Andor iXon
Lens	50 mm
Camera box *[cm]*	70
Rotation angle	π
Projections	801
Exposure per projection *[s]*	2 [20×100 ms]

Table 6.4: *Experimental parameters used for a tomographic study of Bronze Age pottery.*

Marine biology

Corals are highly sensitive to their marine surroundings, and their annual skeletal growths hold a reliable, long-term, chronological record of the environmental and climatic conditions in which they live (changes in temperature, influxes of toxins, etc.). Environmental shifts are indicated by changes both in the skeletal density and in the the concentration and distribution of accumulated hydrogenous material such as organic matter (algae) and fluid inclusions [83, 84], which should be directly observable using neutrons (thermal neutrons: $\sigma\{H\}=82.36$ *barn*, $\sigma\{CaCO_3\}=21.56$ *barn*).

Figure 6.13 shows a section of *Porites sp.* (41×76×7 mm), a tropical reef-building coral that grows in vast colonies of identical polyps (milliscopic in size), which was extracted from Myrmidon Reef, part of the central Great Barrier Reef, Australia. Each polyp is surrounded by a tubular skeleton, or corallite, of aragonite (a mineral of calcium carbonate), which is aligned perpendicular to the growth surface of the colony. The growth surface is bumpy, and new corallites form at the summit of the bumps by assexual division. As the coral grows upwards and outwards, older corallites become progressively displaced from the summit, ultimately disappearing from the growth surface at the bottom of valleys between adjacent bumps [85]. It was expected that organic material would be trapped within in the skeleton at the points where the corallites grow together (i.e. in the valleys). Neutron tomography, however, reveals that exactly the opposite is in fact true (Figure 6.14, experimental parameters given in Table 6.5).

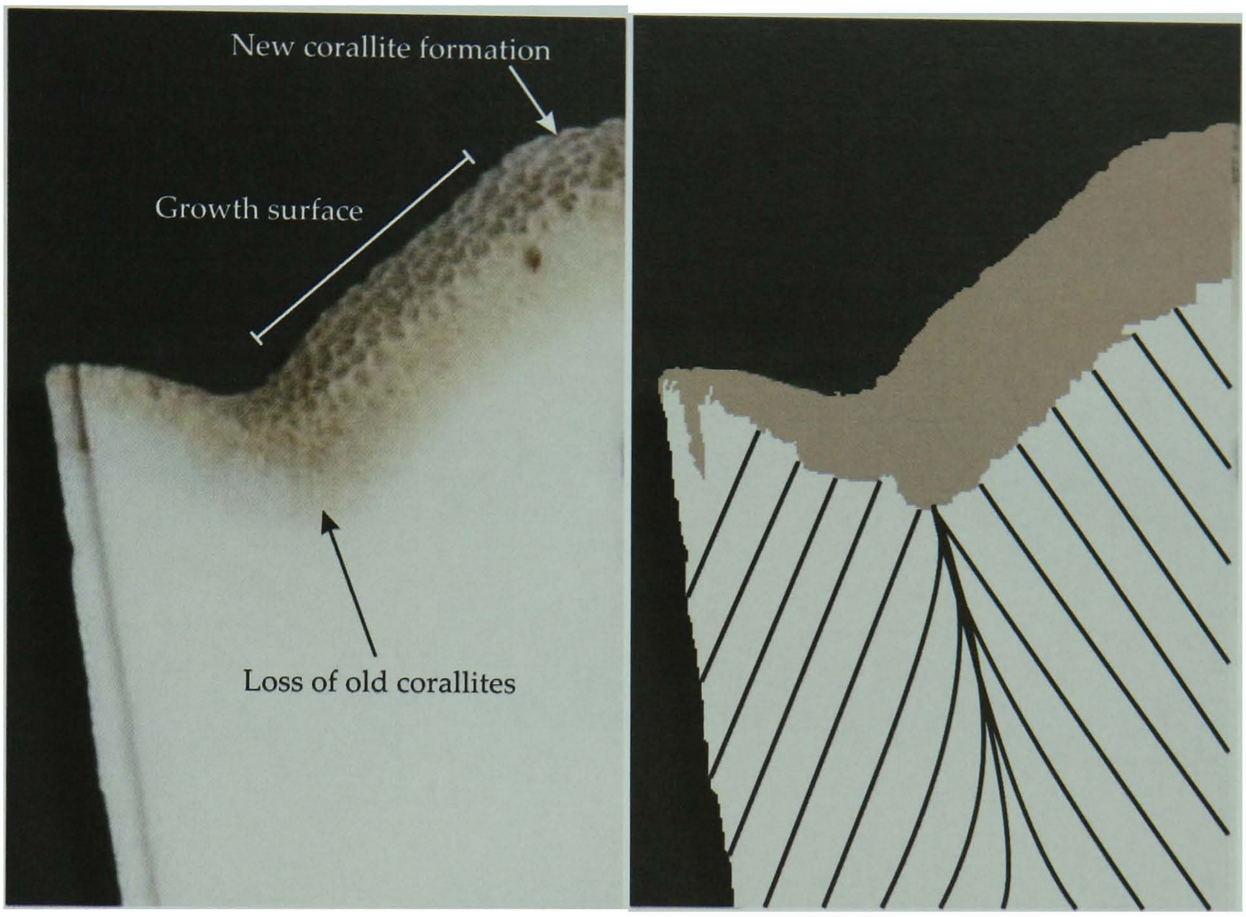

Figure 6.13: *A photograph (left) and an illustration (right) of a section of Porites sp. coral showing a bump and valley on the growth surface. New corallites grow at the summit of the bumps and are progressively displaced as the coral grows outwards before disappearing from the growth surface at the bottom of a valley. The black lines indicate the approximate orientation of the corallites.*

Individual corallites are visible emanating perpendicular to the organic-rich layer at the growth surface (the top ~5 *mm*). Running parallel to the growth surface are three discontinuous bands of hydrogenous material, but these exist only where the corallites are perpendicular to the growth surface (i.e. where the corallites are fully developed and growing parallel to each other) and stop in the valley region. This reason for this curious feature is not currently understood.

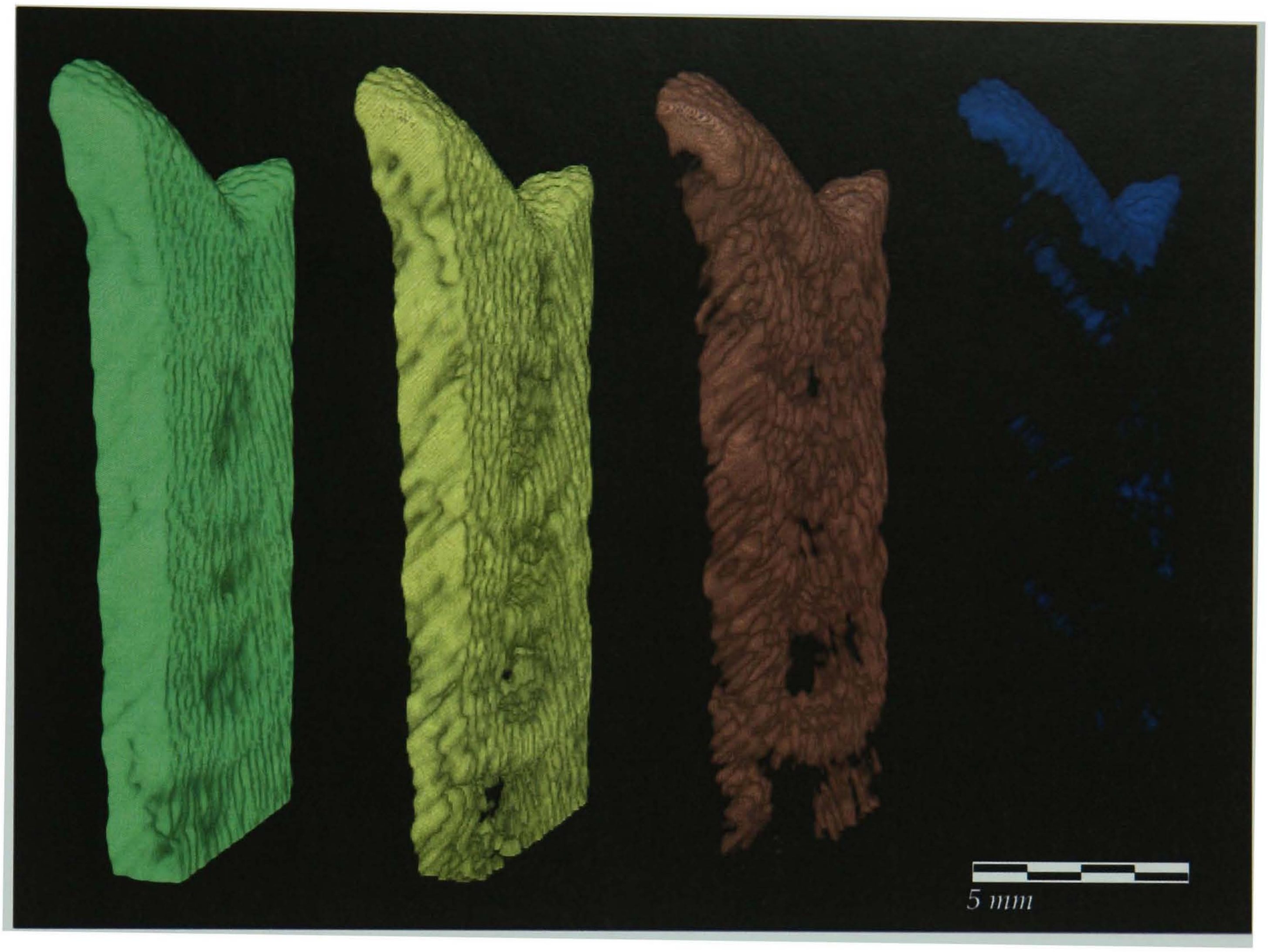

Figure 6.14: *Tomographic reconstruction of a piece of Porites sp. coral showing changes in the skeletal density (yellow, green and coral; density increasing from left to right) and the presence of hydrogenous material both at the surface (the top ~5 mm) and trapped within the skeleton (blue).*

Camera	Andor iXon
Lens	50 mm
Camera box *[cm]*	100
Rotation angle	2π
Projections	800
Exposure per projection *[s]*	5 [50×100 ms]

Table 6.5: *Experimental parameters used for a tomographic study of coral.*

7 Discussion

7.1 Instrumentation

Neutron radiography and tomography are routinely applied non-destructive testing techniques on *Neutrograph,* and the data acquisition, processing and evaluation steps are understood and undertaken as a matter of course. However, while the present equipment is passable, there are considerable technological limitations that need addressing in order to improve performance characteristics. The most important aspects of this are the attainable temporal and spatial resolution, and progress in these areas would undoubtedly expand the applicability of neutron imaging.

The temporal resolution, in terms of image exposure times, is limited primarily by the measured radiation intensity. *Neutrograph* already receives a neutron flux around the peak of what is possible with the current generation of neutron sources, so any increase here must come from improvements in the efficiency of the neutron-photon conversion in the scintillator and of the subsequent photon detection in the camera. Also of importance, in terms of the frame rate, is the readout speed of the detector electronics. It is clearly detrimental to dynamic tomography acquisition rates (as well as wasteful in any application) to be have exposure times in the millisecond regime (as is possible on *Neutrograph*), if only tens of frames per second can be recorded.

The spatial resolution can be increased by improvements in the detection process, notably the spot size of the neutron-photon conversion and new optics to decrease the image pixel size. However, such steps would be pointless for the most part on *Neutrograph* without first decreasing the beam divergence. Hopefully, this will be achieved in the near future with the installation of collimators in the primary casemate.

7.2 Applicability of neutron imaging techniques

In terms of imaging techniques, the similarities between neutrons and x-rays are so striking that it is hard not to constantly draw parallels. It is important when doing so, however, to remember that neutrons and x-rays are not necessarily in competition with one another, but instead provide complementary information; in situations where one fails the other will often succeed. Although the development of neutron-based methods has undeniably benefited greatly from some instrumental developments (digital detector systems, for example) and knowledge-base laid down by other imaging technologies, they have also suffered from the fact that the use of x-rays for non-destructive investigations already permeates almost every discipline of physical science. This has made it difficult for neutrons to make a substantial impact and, although applied to an ever-increasing number of fields, they are exploited much more sporadically. Indeed, it is frequently only in situations where x-rays are non-viable (e.g. when heavy elements are concerned) that neutrons are a preferred option. Even in some cases where neutrons hold an intrinsic advantage (e.g. visualising water flow through a system), a solution can be found so that x-rays can be used instead [24 compared with 86, for example].

The reasons for this are twofold. Firstly, unlike neutrons, x-radiation does not induce sample radioactivity. Secondly, although neutron techniques have made considerable progress in the past decade, this has been stymied by the small number of dedicated worldwide facilities with a high enough flux to produce good quality results within a reasonable exposure time. As a result, their x-ray counterparts, which have a much longer history of research and development (making a direct comparison perhaps a little unfair), are far ahead in terms of both performance and accessibility. Consequently, the evolution of neutron imaging methods is currently very much solution-driven and problem-lacking. In other words, techniques arise and develop in many cases through an aspiration to discover what is experimentally possible and not in response to the demands of any specific application. That is not to say that neutron imaging is redundant, indeed it has already shown its potential after having been employed successfully in a broad variety of applications including palaeontology, archaeology, materials science, engineering, and fluid mechanics. Rather, it lacks that decisive, quintessential application that would elevate it from something of a fringe role to being an influential tool for scientific investigation.

7.3 Further developments

Aside from developing the instrumentation and extending the use of neutron imaging into new fields of application, it is also necessary to refine the methodology of data acquisition, presentation and analysis, which will augment the applicability of imaging techniques.

7.3.1 Data acquisition

The amount and type of information extractable from imaging data can be limited by current acquisition methods, and new approaches need to be developed to allow access to the maximum possible data. As a case in point, consider a single radiograph of a sample with vast variations in local attenuation coefficient (or correspondingly large fluctuations in the sample thickness); a long exposure may reveal features in high-attenuation regions, while overexposing the low-attenuation regions, whereas a short exposure may reveal features in low-attenuation regions, while underexposing high-attenuation regions. However, a series of radiographs with an array of exposure settings (from underexposure to overexposure) could be used to cover the whole dynamic range; since every region is likely to be well-exposed at least once, the separate radiographs could be combined to provide enhanced visualisation of the whole sample in a single image. This is akin to high dynamic range photography, which achieves much the same effect for regions of dark shadow and bright highlight.

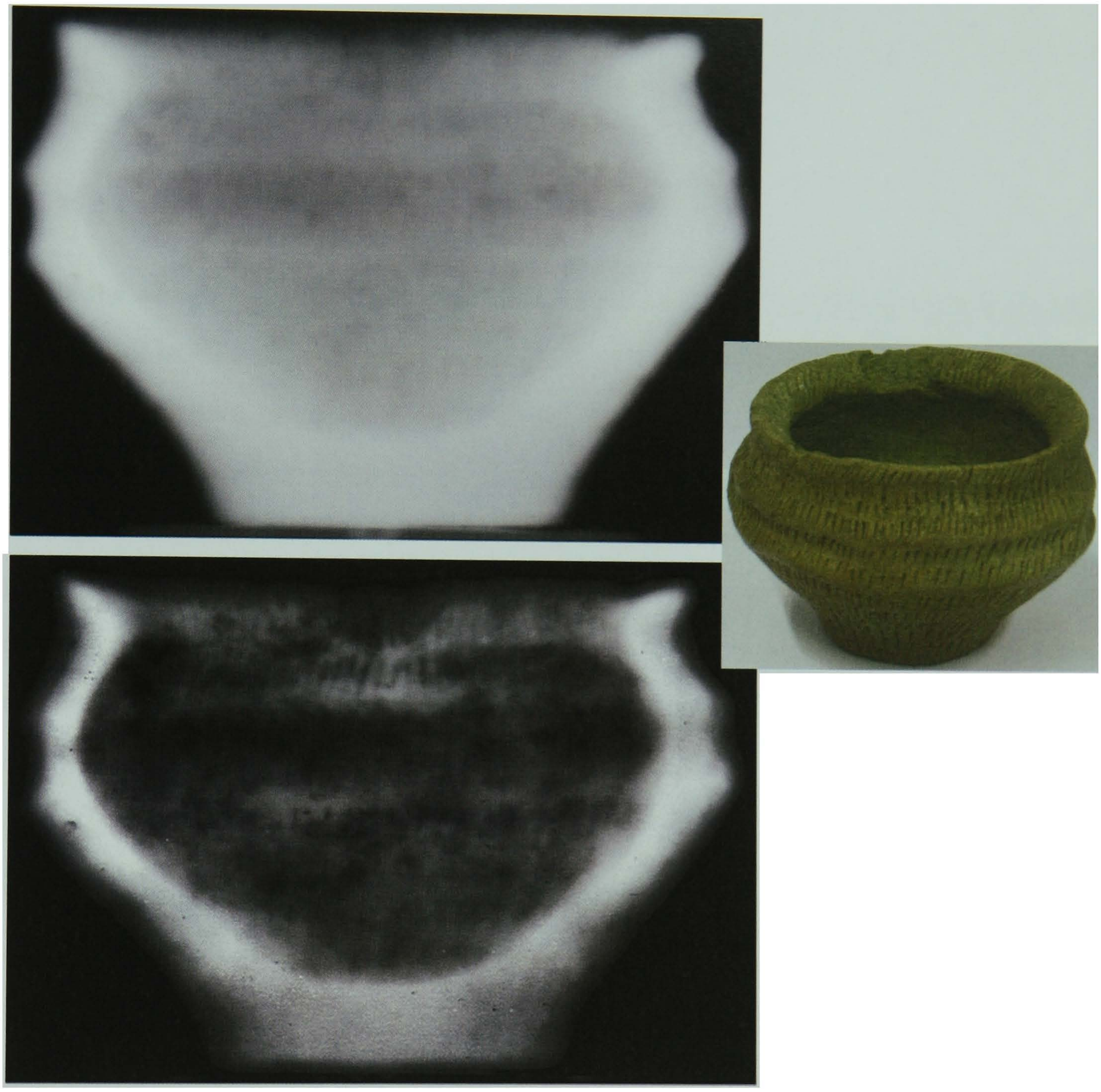

Figure 7.1: *An example of standard radiographic imaging (top) compared with (pseudo) high dynamic range radiographic imaging (bottom) for a Bronze Age food vessel. The vertical groove pattern carved into the bowl is barely visible in the standard radiograph, but becomes much clearer in the high dynamic range radiograph.*

Figure 7.1 shows a comparison of standard radiographic imaging and high dynamic range radiographic imaging for a Bronze Age food vessel. The high dynamic range image reveals many more of the features within the walls of the bowl (the vertical incised-groove pattern, and several inclusions and air voids, for example) and in more detail. Note, however, that this is only an example of pseudo high dynamic range image since data for the regions of lowest radiation transmission (where the curvature of the walls of the bowl is tangential to the beam propagation direction) are missing or incomplete (i.e. the brightest areas of the image). In its true form this method is expected to yield much better results.

7.3.2 Data presentation

While the two-dimensional nature of radiographs makes them easy to convey through a variety of media, three-dimensional tomography volumes are much more difficult to present. Software can be used to express the data in two dimensions by using highlights and shadows to create the feeling of depth, but this could be improved upon through the development of algorithms that are capable of displaying volume data as a pseudo-hologram. These three-dimensional representations would exhibit parallax and depth, and change aspect when viewed from different angles, providing a useful three-dimensional overview of the sample in a single image.

7.3.3 Data analysis

The visual nature of imaging data makes it relatively simple to understand and interpret, and thus highly appealing. However, while providing useful diagnostic information (if and where a given feature is present), it is often more difficult to extract quantitative information (the exact geometrical shape and size and of that feature) from the results. It would, therefore, be extremely useful to begin to use the volume data in conjunction with algorithms that can recognise and evaluate selected properties of structures or surfaces of interest – their morphology, densities, and sizes.

Appendix A

The following is an outline of the mathematical concept of parallel beam tomography, which, aside from being the most common neutron imaging beam geometry, is also mathematically the simplest. A much more robust and extensive treatment as well as further proofs and derivations can be found in, for example, [29-31, 43, 87].

A.1 The Radon transform

If the sample is described in a coordinate system *(x,y,z)*, where *z* is the rotation axis, then each projection can be described in a coordinate system *(ε,z)* (Figure A.1), related to the former by

$$\varepsilon = x\cos\theta + y\sin\theta \qquad \text{Equation A.1}$$

The grey-scale values in each processed projection, *P*, are connected to the local material attenuation coefficients, *α(x,y,z)*, summed along the path through the sample, *s(x,y,z)* according to

$$P(\varepsilon, z) = \int \alpha(x, y, z)\, \mathrm{d}s(x, y, z) \qquad \text{Equation A.2}$$

In parallel geometry, the path through the sample is parallel to *η*, which is orthogonal to *ε* and *z*, and any slice can be treated independently of any other, meaning that the local attenuation coefficient becomes a two-dimensional function that is independent of *z*, *f(x,y)*.

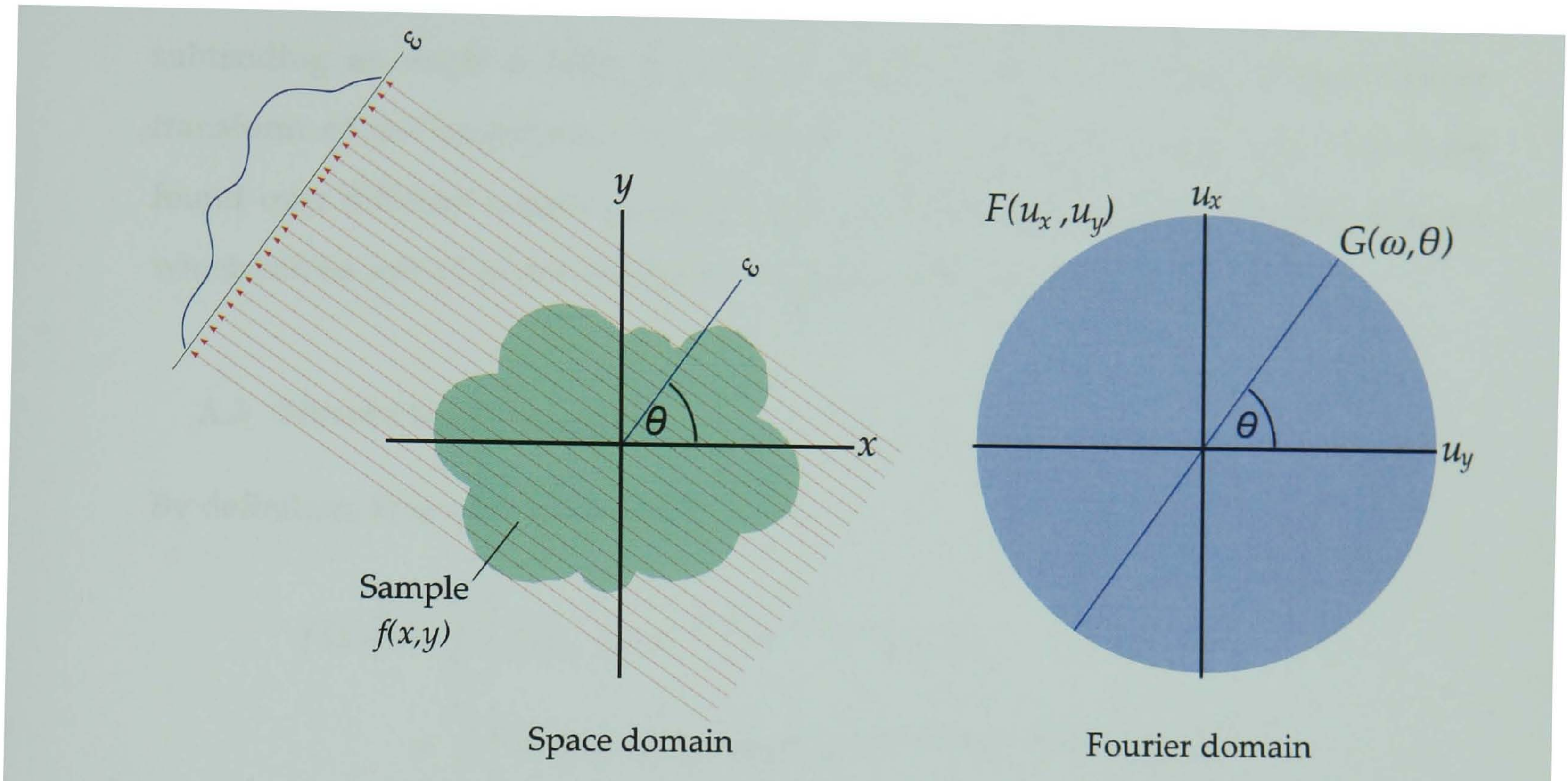

Figure A.1: *The coordinate system of the Radon transform and the Fourier slice theorem.*

$$P(\varepsilon) = \int_{-\infty}^{\infty} f(x,y)\,\mathrm{d}\eta \qquad \text{Equation A.3}$$

More generally, for any projection, $P_\theta(\varepsilon)$, measured at an arbitrary angle, θ, about the *z*-axis,

$$P_\theta(\varepsilon) = \int_{-\infty}^{\infty}\int_{-\infty}^{\infty} f(x,y)\,\delta(x\cos\theta + y\sin\theta - \varepsilon)\,\mathrm{d}x\,\mathrm{d}y \qquad \text{Equation A.4}$$

which is known as the Radon transform of the distribution $f(x,y)$.

A.2 The Fourier slice theorem

The objective of tomographic reconstruction is, given knowledge of $P_\theta(\varepsilon)$, to solve the inverse Radon transform to find $f(x,y)$. The solution is based on the Fourier slice theorem, which relates the two-dimensional Fourier transform, $F(u_x,u_y)$, of the function $f(x,y)$ to the one-dimensional Fourier transform, $G(\omega,\theta)$, of $P_\theta(\varepsilon)$.

$$G(\omega,\theta) = F(\omega\cos\theta, \omega\sin\theta) \qquad \text{Equation A.5}$$

In words, the value of the two-dimensional Fourier transform of *f(x,y)* along a line subtending an angle θ with the axis u_x is given by the one-dimensional Fourier transform of the projection $P_\theta(\varepsilon)$. It follows that if sufficient projections, $P_\theta(\varepsilon)$, are found over different angles, u_x–u_y space can be filled, generating a complete $F(u_x,u_y)$, which can be solved to find its inverse Fourier transform, *f(x,y)*.

A.3 Filtered back-projection

By definition, $F(u_x,u_y)$ is related to *f(x,y)* by

$$\begin{aligned} f(x,y) &= \int_{\infty}^{\infty}\int_{\infty}^{\infty} F(u_x,u_y)\, e^{-i2\pi u_x x}\, e^{-i2\pi u_y y}\, \mathrm{d}u_x \mathrm{d}u_x \\ &= \int_0^{2\pi}\int_0^{\infty} \omega F(\omega\cos\theta,\omega\sin\theta)\, e^{-i2\pi\omega x\cos\theta}\, e^{-i2\pi\omega y\sin\theta}\, \mathrm{d}\omega \mathrm{d}\theta \\ &= \int_0^{2\pi}\int_0^{\infty} \omega G(\omega,\theta)\, e^{-i2\pi\omega(x\cos\theta+y\sin\theta)}\, \mathrm{d}\omega \mathrm{d}\theta \end{aligned}$$

Equation A.6

but $G(\omega,\theta+\pi) = G(-\omega,\theta)$, which gives

$$\begin{aligned} f(x,y) &= \int_0^{\pi}\int_0^{\infty} \omega G(-\omega,\theta)\, e^{-i2\pi\omega(x\cos(\theta+\pi)+y\sin(\theta+\pi))}\, \mathrm{d}\omega \mathrm{d}\theta \\ &= \int_0^{\pi}\int_{-\infty}^{0} (-\omega)G(\omega,\theta)\, e^{-i2\pi\omega(x\cos\theta+y\sin\theta)}\, \mathrm{d}\omega \mathrm{d}\theta \\ &= \int_0^{\pi}\int_{-\infty}^{\infty} |\omega|G(\omega,\theta)\, e^{-i2\pi\omega(x\cos\theta+y\sin\theta)}\, \mathrm{d}\omega \mathrm{d}\theta \\ &= \int_0^{\pi} Q_\theta(x\cos\theta+y\sin\theta)\, \mathrm{d}\theta \end{aligned}$$

Equation A.7

where

$$\begin{aligned} Q_\theta(\varepsilon) &= \int_{-\infty}^{\infty} |\omega|G(\omega,\theta)\, e^{-i2\pi\omega\varepsilon}\, \mathrm{d}\omega \\ &= P_\theta(\varepsilon) * \varrho(\varepsilon) \end{aligned}$$

Equation A.8

is a filtered projection obtained by convolving the measured projection, $P_\theta(\varepsilon)$, with a ramp filter, $\varrho(\varepsilon)$, defined in frequency space as $R(\omega) = |\omega|$. The reconstructed slice (i.e. the function *f(x,y)*) can be found by summing $Q_\theta(\varepsilon)$ over all angles, θ. Since $Q_\theta(\varepsilon)$

contributes to all points in the slice along ε, this can be visualised as Q being projected or smeared back across the image plane along this line.

A.4 Number of projections

Fourier space is filled radially with a sampling interval, $\Delta\omega_r$, given by

$$\Delta\omega_r = \frac{1}{n\Lambda} \qquad \text{Equation A.9}$$

where n is the number of sampling points in the projection (i.e. the number of pixels across the width of the image) and Λ is the projection sampling interval (i.e. the pixel width). According to the Nyquist theorem, the highest resolvable frequency, ω_{max}, is

$$\omega_{max} = \frac{1}{2\Lambda} \qquad \text{Equation A.10}$$

Although the radial sampling frequency is constant, the angular frequency of sampling points decreases towards towards the periphery (Figure A.2), where the interval, $\Delta\omega_a$, is largest

$$\Delta\omega_a = \omega_{max}\,\Delta\theta \qquad \text{Equation A.11}$$

where $\Delta\theta$ is the angular spacing between projections. To ensure sufficient sampling, the interval (both angular and radial) at all points in the Fourier domain must be of the same order. Equating $\Delta\omega_a$ and $\Delta\omega_r$ leads to

$$\Delta\theta = \frac{\Delta\omega_r}{\omega_{max}} = \frac{2}{n} \qquad \text{Equation A.12}$$

Hence, theoretically, for a high quality image, the number of projections, Σ, required in π-rotation is

$$\Sigma = \frac{\pi}{\Delta\theta} = \frac{\pi n}{2} \qquad \text{Equation A.13}$$

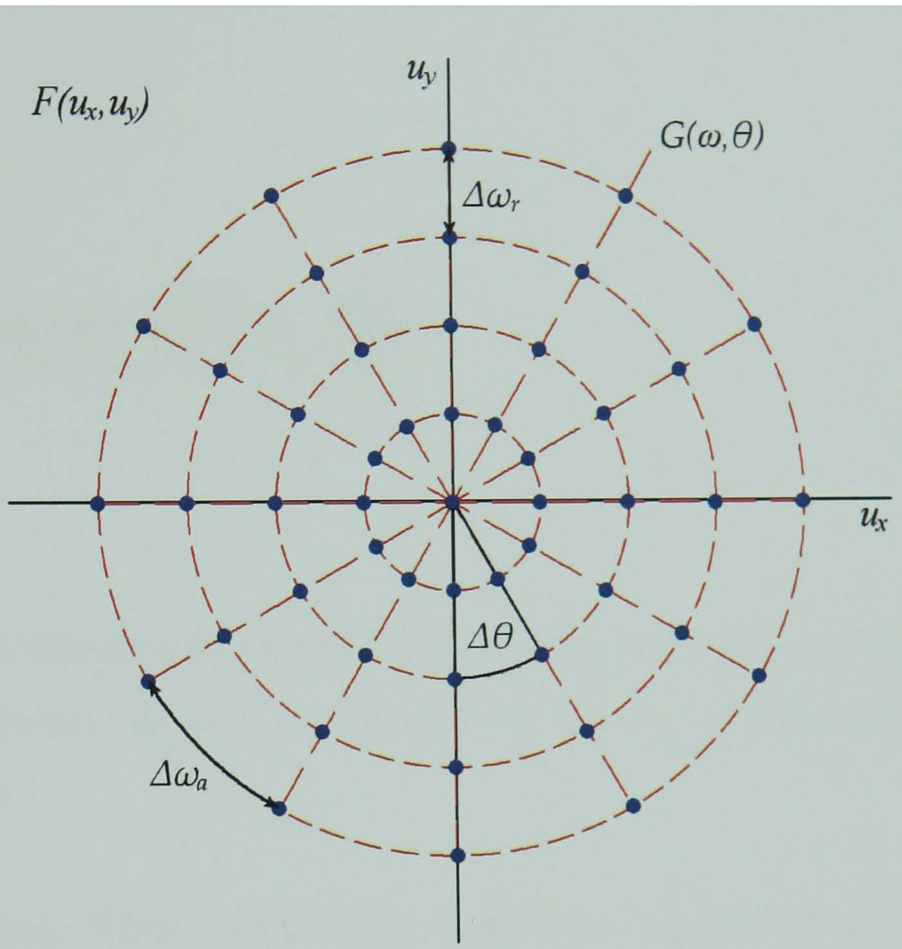

Figure A.2: *The radial filling of Fourier space, $F(u_x,u_y)$, by the sampling points (blue) of projections, $G(\omega,\theta)$. The red dashed lines are intended as guides to the eye.*

Appendix B

The following is intended as a rough guide to the steps routinely involved in neutron imaging experiments, as well as some useful tips in avoiding some of the more common pitfalls.

Sample activation: When atoms absorb a neutron they are transmuted into a new isotope. These new isotopes are commonly unstable and return to their original state via radioactive decay. For most elements, the level of activity is low and the half life is short, but this is not always the case and radioactive samples require safe radiation-shielded storage. This is worth bearing in mind if the sample is highly valuable or is required for other measurements. If constituents of the sample are unknown, then one possibility is to irradiate the sample briefly with neutrons and to then measure its gamma spectrum (radioactive decay is often accompanied by gamma ray emission at element-specific energies). Note, however, that if the sample does contain problematic elements, after even a few minutes in a high intensity beam it may already be too late.

Contrast: Although possible to the calculate theoretical beam transmission and material attenuation coefficients, this does not always give a clear indication of, for example, how scattering will affect the spatial resolution, or whether sufficient neutrons will be detected to produce a usable image. Whenever possible, the best approach is often to make test measurements.

Just because a feature is not detectable with radiography does not necessarily mean that it will not be detected by tomography. A radiograph has no depth perception and so cannot differentiate between a short path with high attenuation and a longer path with lower attenuation. A subtle attenuation variation may thus be concealed inside an irregularly shaped sample.

Sample preparation: In order to ensure the maximum possible spatial resolution, the sample should be positioned as close to the detection plane as possible without disturbing or being disturbed by it – remember that in tomography experiments it may need to be periodically moved in and out of the field of view to acquire open beam images. The sample should be fixed firmly to the rotation table to prevent artifacts caused by slippage.

On a high flux instrument, once irradiated the casemate and sample are likely to remain active (and therefore out of bounds) for upwards of an hour afterwards. It is therefore worth taking extra preparation time to ensure that equipment is correctly set up and functioning before opening the primary beam shutter.

Data acquisition: A complete set of tomography data (assuming parallel beam geometry) consists of a series of projections with equiangular separation from 0 to π (2π for a divergent beam), one dark image and one (or more, depending on the magnitude of detector degradation during the measurement) open beam image. The whole of the sample (not just a region of interest) must be in the field of view for every projection.

Data should be as noise-free and as statistically accurate as possible. This requires that exposure times be as long as possible, measuring a strong signal through the most opaque parts of the sample, without saturating any part of the detector (i.e. use the full dynamic range of the detector). Statistical accuracy can also be improved by averaging many images for each projection. Although the projection data are undoubtedly important, a small number of missing or erroneous data in a small number of projections will not necessarily be overly detrimental. Much worse would be if these errors appeared in the dark images or open beam images, since these are used to correct, and are therefore present in, every single projection.

For simplicity, projection data, dark images and open beam images should be acquired with exactly the same experimental parameters, i.e. exposure time, image dimensions, and number of images over which to average.

Number of projections: The theoretical number of projections required is $(\pi n)/2$, where n is width of each projection in pixels (Equation A.13). More projections will not improve the resolution of the reconstruction, but they will contribute to statistical accuracy.

Alignment of tomographic data: Tomographic data should always include a projection at π (assuming π-rotation). Although it will not be used in reconstructions, it serves an important purpose as it is a mirror image of the projection at 0 and can therefore be used to align all projections at the centre of rotation (Figure B.1) – subtracting P_0 from $-P_\pi$ will yield a roughly homogeneous image when properly aligned. It can also be used to correct any tilt associated with a twisted camera or with an inclination of the sample rotation axis perpendicular to the beam propagation direction, i.e. only when the inclination is coplanar with the field of view – any inclination of the sample rotation axis parallel to the beam propagation direction is impossible to correct completely.

(a) (b) (c)

Figure B.1: *An example using P_0 and $-P_\pi$ to align a tomography dataset, showing (a) completely misaligned data, (b) horizontally aligned, but rotationally misaligned data, and (c) well aligned data.*

Appendix C

The following images are supplementary to Section 6: Archaeology, and show a three-dimensional rendering of a Bronze Age pottery sherd (circa BC *1800-2000*) from a variety of angles.

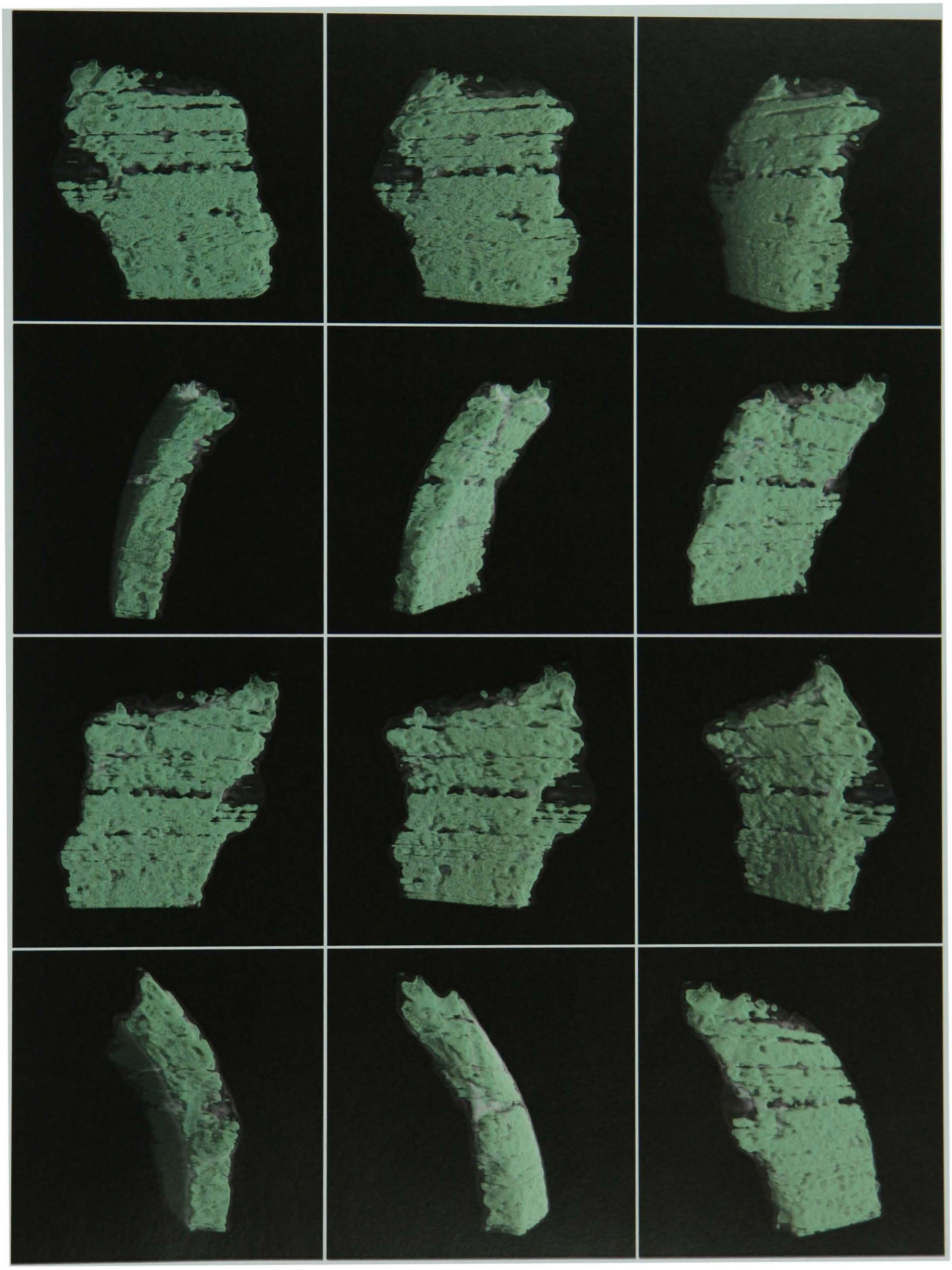

Figure C.1: *A 3-D rendering of a Bronze Age pottery sherd, showing the horizontal band structure of the clay. (See also* Section 6: Archaeology*).*

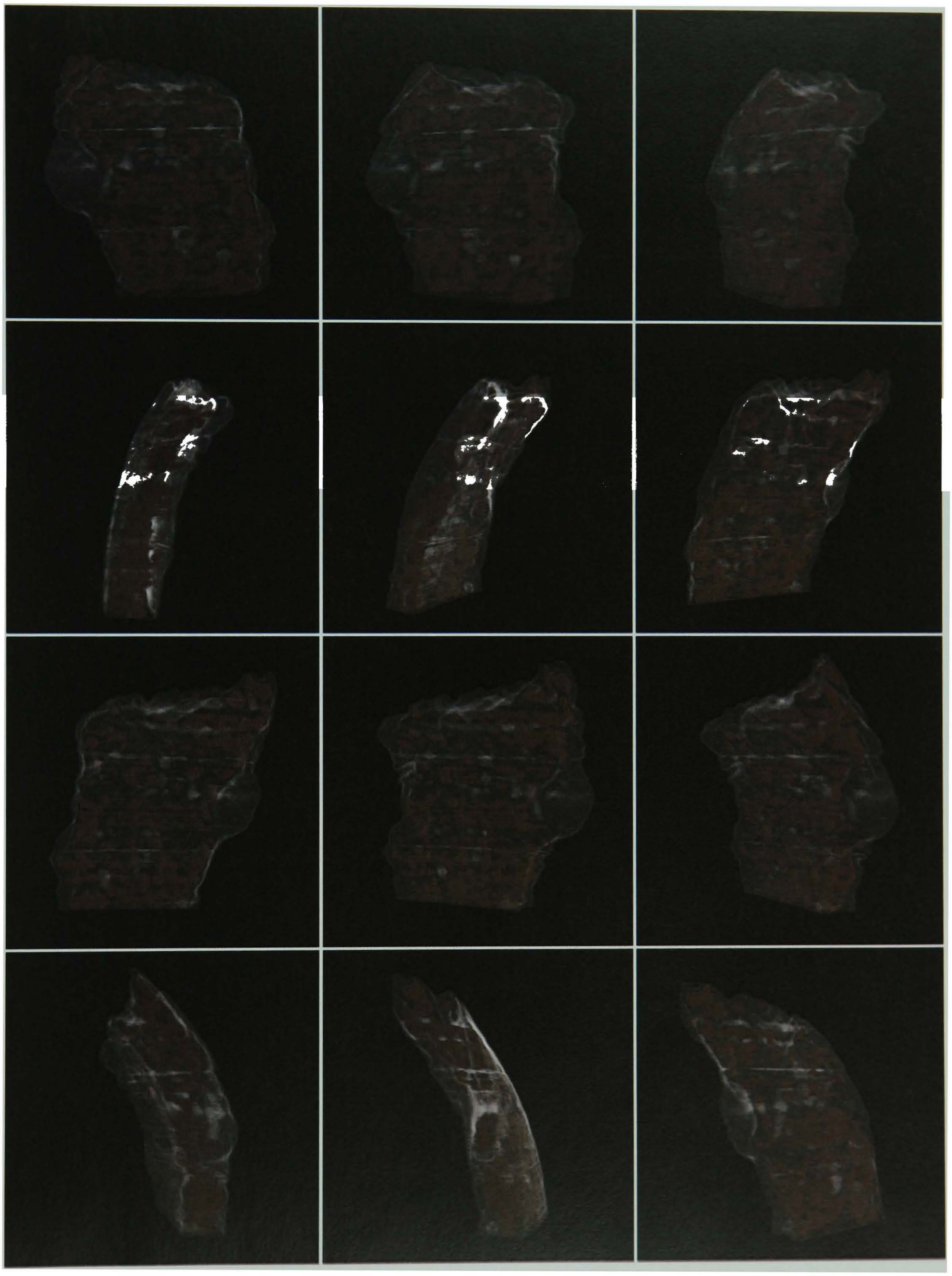

Figure C.2: *A 3-D rendering of a Bronze Age pottery sherd, showing the inclusions within the clay. (See also* Section 6: Archaeology*).*

Bibliography

[1] H. Kallmann, *Neutron radiography,* Research **1**, pg. 254-260 (1948).

[2] O. Peter, *Neutronen-Durchleuchtung,* Zeitschrift für Naturforschung **1**, pg. 557-559 (1946).

[3] H. Berger, *Neutron radiography,* Annual Review of Nuclear Science **21**, pg. 335-364 (1971).

[4] A.R. Spowart, *Neutron radiography,* Journal of Physics E: Scientific Instruments **5**, pg. 497-510 (1972).

[5] A.I. Lewcock, *Neutron radiography: status report,* Physics Technology **10**, pg. 74-76 (1979).

[6] J. Thewlis, *Neutron radiography,* British Journal of Applied Physics **7**, pg. 345-350 (1956).

[7] J. Thewlis & R. Derbyshire, *Harwell Report,* Atomic Energy Research Establishment M/TN **37**, (1956).

[8] G.N. Hounsfield, *Computerized transverse axial scanning (tomography). Description of system,* British Journal of Radiology **46**, pg. 1016-1022 (1973).

[9] J. Ambrose & G. Hounsfield, *Computerized transverse axial tomography,* British Journal of Radiology **46**, pg. 148-149 (1973).

[10] J. Radon, *Berichte über die Verhandlungen der Königlich Sächisischen Gesellshaft der Wissenschaften zu Luipzig,* Verhandlungen der Königlich Sächisischen Gesellshaft der Wissenschaften **69**, pg. 262–277 (1917).

[11] A. Hilger, N. Kardjilov, M. Strobl, et al., *The new cold neutron radiography and tomography instrument CONRAD at HMI Berlin,* Physica B: Condensed Matter **385-386**, pg. 1213-1215 (2006).

[12] E. Calzada, B. Schillinger & F. Grünauer, *Construction and assembly of the neutron radiography and tomography facility ANTARES at FRM II*, Nuclear Instruments and Methods in Physics Research A **542**, pg. 38–44 (2005).

[13] E. Lehmann, P. Vontobel & L. Wiezel, *Properties of the radiography facility NEUTRA at SINQ and its potential for use as European reference facility*, Proceedings of the 6th World Conference on Neutron Radiography, (1999).

[14] E. Deschler-Erb, E.H. Lehmenn, L. Pernet, et al., *The complementary use of neutrons and x-rays for the non-destructive investigation of archaeological objects from Swiss collections*, Archaeometry **46**, pg. 647-661 (2004).

[15] W. Kockelmann, S. Siano, L. Bartoli, et al., *Applications of tof neutron diffraction in archaeometry*, Appl. Phys. A **83**, pg. 175-182 (2006).

[16] J. Rant, Z. Milič, J. Istenič, et al., *Neutron radiography examination of objects belonging to the cultural heritage*, Applied Radiation and Isotopes **64**, pg. 7–12 (2006).

[17] D. Schwarz, P. Vontobel, E.H. Lehmann, et al., *Neutron tomography of internal structures of vertebrate remains: a comparison with x-ray computed tomography*, Palaeontologia Electronica **8**, pg. 1-11 (2005).

[18] F.C. de Beer, M. Coetzer, D. Fendeis, et al., *Neutron radiography and other NDE tests of main rotor helicopter blades*, Applied Radiation and Isotopes **61**, pg. 609–616 (2004).

[19] A.E.-G.E. Abd & J.J. Milczarek, *Neutron radiography study of water absorption in porous building materials: anomalous diffusion analysis*, Journal of Physics D: Applied Physics **37**, pg. 2305–2313 (2004).

[20] N. Takenaka, T. Kadowaki, Y. Kawabata, et al., *Visualization of cavitation phenomena in a diesel engine fuel injection nozzle by neutron radiography*, Nuclear Instruments and Methods in Physics Research A **542**, pg. 129–133 (2005).

[21] M. Bastürka, N. Kardjilov, H. Rauch, et al., *Neutron imaging of fiber-reinforced materials*, Nuclear Instruments and Methods in Physics Research A **542**, pg. 106–115 (2005).

[22] E. Lehmann, G. Kühne, P. Vontobel, et al., *Material inspections by different methods of neutron radiography-specific problem solutions*, IEEE Transactions on Nuclear Science **52**, pg. 317-321 (2005).

[23] E.H. Lehmann, P. Vontobel & A. Hermann, *Non-destructive analysis of nuclear fuel by means of thermal and cold neutrons*, Nuclear Instruments and Methods in Physics Research A **515**, pg. 745–759 (2003).

[24] D. Kramer, E. Lehmann, G. Frei, et al., *An on-line study of fuel cell behavior by thermal neutrons*, Nuclear Instruments and Methods in Physics Research A **542**, pg. 52–60 (2005).

[25] I. Manke, Ch. Hartnig, M. Grünerbel, et al., *Quasi-in situ neutron tomography on polymer electrolyte membrane fuel cell stacks*, Applied Physics Letters **90**, pg. 184101 (2007).

[26] A.X. da Silva & V.R. Crispim, *Use of thermal neutron tomography for the detection of drugs and explosives*, Radiation Physics and Chemistry **61**, pg. 767–769 (2001).

[27] M. Wilding, C.E. Lesher & K. Shields, *Applications of neutron computed tomography in the geosciences*, Nuclear Instruments and Methods in Physics Research A **542**, pg. 290–295 (2005).

[28] U. Matsushima, Y. Kawabata, M. Hino, et al., *Measurement of changes in water thickness in plant materials using very low-energy neutron radiography*, Nuclear Instruments and Methods in Physics Research A **542**, pg. 76–80 (2005).

[29] A.C. Kak & M. Slaney, *Principles of Computerized Tomographic Imaging*, Society of Industrial and Applied Mathematics, (2001).

[30] A. Faridani, *Introduction to the mathematics of computed tomography*, Inside Out: Inverse Problems (MSRI Publications) **47**, (2003).

[31] J. Banhart (ed), *Advanced Tomographic Methods in Materials Mesearch and Engineering*, Oxford University Press, (2008).

[32] K.M. Rosenberg, CTSim 3.5 User Manual.

[33] F. Pfeiffer, T. Weitkamp, O. Bunk, et al., *Phase retrieval and differential phase-contrast imaging with low-brilliance x-ray sources*, Nature Physics **2**, pg. 258-226 (2006).

[34] F. Pfeiffer, C. Grünzweig, O. Bunk, et al., *Neutron phase imaging and tomography*, Physical Review Letters **96**, pg. 215505 (2006).

[35] M. Sánchez del Río & R.J. Dejus., *XOP 2.1: A new version of the X-ray optics software toolkit*, Synchrotron Radiation Instrumentation: Eighth International Conference, pg. 784-787 (2004).

[36] A.-J. Dianoux & G. Lander (ed), *Neutron Data Booklet*, OCP Science, (2003).

[37] L. Alianelli, M. Sánchez del Río & R. Felici, *NOP: a new software tool for neutron optics*, Physica B: Condensed Matter **350**, pg. e739–e741 (2004).

[38] M. Thoms, D. Myles & C. Wilkinson, *Neutron detection with imaging plates part I: image storage and readout*, Nuclear Instruments and Methods in Physics Research A **424**, pg. 26-33 (1999).

[39] M. Thoms, *Neutron detection with imaging plates part II: detector characteristics*, Nuclear Instruments and Methods in Physics Research A **424**, pg. 34-39 (1999).

[40] The Neutron Imaging and Activation Group, Informationen für potenzielle Nutzer und Anwender, Neutron Imaging an der Spallations-Neutronenquelle SINQ.

[41] PCO Computer Optics GmbH, PCO Sensicam 12-bit Cooled VGA CCD Camera Manual.

[42] Andor Technology PLC, Andor iXon DV885 EMCCD Manual.

[43] S.W. Smith, *The Scientist and Engineer's Guide to Digital Signal Processing,* California Technical Publishing, (1997).

[44] N. Kardjilov, *Neutron Imaging Group, Hahn-Meitner-Institut, Berlin, Germany,* Personal Communication.

[45] G. Shirane, S.M. Shapiro & J.M. Tranquada, *Neutron scattering with a triple-axis spectrometer: basic techniques,* Cambridge University Press, (2002).

[46] G. Ehlers & F. Klose, *Characterization of magnetic materials by means of neutron scattering,* Handbook of Advanced Magnetic Materials Volume 2. Characterization and Simulation, pg. 66 - 112 (2006).

[47] W. Treimer, M. Strobl, N. Kardjilov, et al., *Wavelength tunable device for neutron radiography and tomography,* Applied Physics Letters **89**, pg. 203504 (2006).

[48] W. Kockelmann, G. Frei, E.H. Lehmann, et al., *Energy-selective neutron transmission imaging at a pulsed source,* Nuclear Instruments and Methods in Physics Research A **578**, pg. 421-434 (2007).

[49] *NEUWAVE Imaging Workshop,* Forschungsneutronenquelle Heinz Maier-Leibnitz, Garching bei München, 2008.

[50] N. Kardjilov, F. de Beer, R. Hassanein, et al., *Scattering corrections in neutron radiography using point scattered functions,* Nuclear Instruments and Methods in Physics Research A **542**, pg. 336–341 (2005).

[51] A. van Overberghe, *High Flux Neutron Imaging for highly dynamic and time resolved non-destructive testing,* Thesis, Ruprecht-Karls-Universität Heidelberg, Germany (2006).

[52] O. Halpern & T. Holstein, *On the passage of neutrons through ferromagnets,* Physical Review **59**, pg. 960-981 (1941).

[53] O. Halpern & T. Holstein, *On the depolarization of neutron beams by magnetic fields,* Proceedings of the National Academy of Science of the United States of America **28**, pg. 112-118 (1942).

[54] M.Th. Rekveldt, *Study of ferromagnetic bulk domains by neutron depolarization in three dimensions,* Zeitschrift für Physik A: Hadrons and Nuclei **259**, pg. 391-410 (1973).

[55] M.Th. Rekveldt, *Neutron depolarization in submicron ferromagnetic materials,* Textures and Microstructures **11**, pg. 127-142 (1989).

[56] N. Kardjilov, I. Manke, M. Strobl, et al., *Three-dimensional imaging of magnetic fields with polarized neutrons,* Nature Physics **4**, pg 399-403 (2008).

[57] M. Hochhold, H. Leeb & G. Badurek, *Tensorial neutron tomography: a first approach,* Journal of Magnetism and Magnetic Materials **157-158**, pg. 575-576 (1996).

[58] G. Badurek, M. Hochhold & H. Leeb, *Neutron magnetic tomography - a novel technique,* Physica B: Condensed Matter **234-236**, pg. 1171-1173 (1997).

[59] H. Leeb, A.M. Hochhold, G. Badurek, et al., *Neutron magnetic tomography: a feasibility study,* Australian Journal of Physics **51**, pg. 401-413 (1998).

[60] H. Leeb, R. Szeywerth, E. Jericha, et al., *Towards manageable magnetic field retrieval in bulk materials,* Physica B: Condensed Matter **356**, pg. 187–191 (2005).

[61] D.J. Hughes & M.T. Burgy, *Reflection of neutrons from magnetized mirrors,* Physical Review **81**, pg. 498-506 (1951).

[62] F. Mezei, *Novel polarized neutron devices: supermirror and spin component amplifier,* Communications on Physics **1**, pg. 81-85 (1976).

[63] F. Mezei & P.A. Dagleish, *Corrigendum and first experimental evidence on neutron supermirrors,* Communications on Physics **2**, pg. 41-43 (1977).

[64] A. Delapalme, J. Schweizer, G. Couderchon, et al., *Etude de l'alliage de Heusler (Cu_2MnAl) comme monochromateur de neutrons polarisés,* Nuclear Instruments and Methods **95**, pg. 589-594 (1971).

[65] P. Courtois, *Characterization of Heusler crystals for polarized neutrons monochromators,* Physica B: Condensed Matter **267-268**, pg. 363-366 (1999).

[66] M. Batz, S. Baeßler, W. Heil, et al., *^{3}He spin-filter for neutrons,* Journal of Research of the National Institute of Standards and Technology **110**, pg. 293-298 (2005).

[67] K.H. Andersen, R. Chung, V. Guillard, et al., *First results from Tyrex the new polarized-^{3}He filling station at ILL,* Physica B: Condensed Matter **356**, pg. 103-108 (2005).

[68] A. Petoukhov, K.H. Andersen, D. Jullien, et al., *Recent advances in polarised ^{3}He spin-filters at the ILL,* Physica B: Condensed Matter **385**, pg. 1146-1148 (2006).

[69] D.S. Hussey, D. R. Rich, A.S. Belov, et al., *Polarized ^{3}He gas compression system using metastability-exchange optical pumping,* Review of Scientific Instruments **76**, pg. 053503 (2005).

[70] S.R. Parnell, G.W. Wallidge, C.D. Frost, et al., *Metastable optical pumping of ^{3}He for neutron spin filter cells at ISIS,* Physica B: Condensed Matter **356**, pg. 114-117 (2005).

[71] W. Heil, H. Humblot, E. Otten, et al., *Very long nuclear relaxation times of spin polarized helium-3 in metal coated cells,* Physics Letters A **201**, pg. 337-343 (1995).

[72] W. Heil, J. Dreyer, D. Hofmann, et al., *^{3}He neutron spin-filter,* Physica B: Condensed Matter **267-268**, pg. 328- (1999).

[73] P. Hohenstein, *X-ray imaging for palaeontology,* British Journal of Radiology **77**, pg. 420-425 (2004).

[74] A. Gibbons, *Paleontologists get x-ray vision,* Science **7**, pg. 1546 - 1547 (2007).

[75] R. Stephens, *Eocene flora from Seymour Island, Antarctica,* Thesis, School of Earth and Environment, University of Leeds, England (2007).

[76] C. Little, *School of Earth and Environment, University of Leeds, England,* Personal communication.

[77] J.M.N.T. Gray & K. Hutter, *Pattern formation in granular avalanches,* Continuum Mechanics and Thermodynamics **9**, pg. 341–345 (1997).

[78] J.M.N.T. Gray & A.R. Thornton, *A theory for particle size segregation in shallow granular free-surface flows,* Proceedings of the Royal Society A **461**, pg. 1447–1473 (2005).

[79] J.M.N.T. Gray & V.A. Chugunov, *Particle-size segregation and diffusive remixing in shallow granular avalanches,* Journal of Fluid Mechanics **569**, pg. 365–398 (2006).

[80] C. Haughton & D. Powlesland, *West Heslerton: The Anglican Cemetery - Volume 1,* The Landscape Research Centre, (1999).

[81] C. Haughton & D. Powlesland, *West Heslerton: The Anglican Cemetery - Volume 2,* The Landscape Research Centre, (1999).

[82] A.M. Gibson & A. Woods, *Prehistoric pottery for the archaeologist,* Continuum International Publishing Group, (1997).

[83] D.J. Barnes & M.J. Devereux, *Variations in skeletal architecture associated with density banding in the hard coral Porites,* Journal of Experimental Marine Biology and Ecology **121**, pg. 37-54 (1988).

[84] M. le Tissier, B. Clayton, B.E. Brown & P.S. Davis, *Skeletal correlates of coral density banding and an evaluation of radiography as used in sclerochronology,* Marine Ecology Progress Series **110**, pg. 29-44 (1994).

[85] W.M. Darke & D.J. Barnes, *Growth trajectories of corallites and ages of polyps in massive colonies of reef-building corals of the genus Porites,* Marine Biology **117**, pg. 321-326 (1993).

[86] Ch. Hartnig, I. Manke, R. Kuhn, et al., *Cross-sectional insight in the water evolution and transport in PEM fuel cells,* Applied Physics Letters **92**, pg. 134106 (2008).

[87] J.C. Russ, *The Image Processing Handbook,* CRC Press, (2002).